Microwave Frequency Power Dependence in High-T_c Thin Films, Grain Boundaries, and Josephson Junctions

by

Youssef M Habib

Submitted to the Department of Physics
in partial fulfillment of the requirements for the degree of

Doctor of Philosophy

at the

MASSACHUSETTS INSTITUTE OF TECHNOLOGY

December 1998

Author .....
Department of Physics
December 1998

Certified by... .....
Mildred S. Dresselhaus
Institute Professor
Thesis Supervisor

Certified by .....
Daniel E. Oates
Visiting Scientist
Thesis Supervisor

Accepted by .....
Marc A. Kastner
Chairman, Department Committee on Graduate Students

Microwave Frequency Power Dependence in High-T_c Thin Films, Grain Boundaries, and Josephson Junctions

by

Youssef M Habib

Submitted to the Department of Physics
on December 1998, in partial fulfillment of the
requirements for the degree of
Doctor of Philosophy

Abstract

A comprehensive study of the dc and rf electrodynamic properties of $YBa_2Cu_3O_{7-\delta}$ (YBCO) thin films, grain boundaries and Josephson junctions (JJ) is presented. The surface impedance $Z_s = R_s + iX_s$ of YBCO thin films is shown to have a dependence on rf current, which leads to nonlinear power losses at levels of rf power that are relevant for device applications. To understand the loss mechanisms in high-T_c thin films, measurements and modeling of the microwave-frequency (rf) power dependence of the impedance in YBCO thin-film grain-boundary Josephson junctions (JJ) are presented. Microwave impedance measurements were performed using a stripline resonator technique on engineered grain-boundary JJs as a function of rf current (10^{-4} to 1 A) and temperature (5 to 70 K). To understand the observed power dependence, a long-junction model which allows for Josephson-vortex creation, annihilation, and motion is introduced. The impedance calculated using the long-junction model fits the measured data qualitatively. It is shown that Josephson vortices generated by the rf fields cause nonlinearities in the impedance, resulting in increases in both resistance and reactance with steps in the resistance due to flux quantization. The modeling results also show second harmonic generation and this is explored experimentally. In addition, a comparative study of the rf power-dependence of thin-film YBCO grain boundaries engineered on sapphire bicrystal substrates with misorientation angles of $\theta = 2°$, $5°$, $10°$, and $24°$ and films grown on single-crystal substrates is presented. The rf results are compared to dc measurements performed on a four-point test structure on the same substrate as the resonator. The measurements demonstrate that low-angle grain boundaries ($\theta \leq 10°$) have little effect on the rf power handling, while the high-angle grain boundaries ($\theta = 24°$) cause large nonlinear losses due to Josephson vortices created by rf currents.

Thesis Supervisor: Mildred S. Dresselhaus
Title: Institute Professor

Thesis Supervisor: Daniel E. Oates
Title: Visiting Scientist

Acknowledgments

I owe thanks to the many professors, students, scientists, technicians, and others who assisted me in my thesis work. I would particularly like to thank Dan Oates for his guidance, friendship and insight throughout my research work. I also thank Millie and Gene Dresselhaus for being great advisors and seeing me through the Ph.D. In addition, I thank my mother for a lifetime of support.

Contents

List of Figures

List of Tables

Chapter 1

Introduction

1.1 Historical Background

H. Kamerlingh Onnes first liquefied helium at the Leiden Cryogenic Laboratory on July 10, 1908. The liquefier built by Kamerlingh Onnes' team produced liquid helium on the first attempt due to the methodical planning and careful execution of the experiment. By pumping out the vapor above the liquid, temperatures as low as 1 K could be attained. Having access to a new realm of low temperatures, Kamerlingh Onnes performed measurements of the electrical resistivity as a function of temperature on different metals. He found, upon cooling, in some metals at a certain temperature the resistivity abruptly dropped to zero. This previously unobserved state of matter, which Kamerlingh Onnes called superconductivity, was not something he expected to observe; rather, it was revealed to him because he strived for excellence in his experimental technique. The increasing complexity of modern research techniques requires a careful and systematic approach to measurement. Quantitative investigation can lead to insight or as Kamerlingh Onnes stated, "door meten tot weten" (through measurement to knowledge).[1]

Kamerlingh Onnes first measured the transition from the normal metallic resistive state to a zero-resistance superconducting state in very pure mercury wire. Mercury undergoes a change of state at a temperature known as the critical temperature T_c which is 4.15 K. Kamerlingh Onnes soon also measured superconducting transitions

in tin (T_c = 3.7 K) and lead (T_c = 7.2 K). By 1930, the highest T_c that had been measured anywhere was in elemental niobium which has a T_c of 9.2 K.

It was discovered by Meissner and Oschenfeld in 1933 that superconductors, in addition to having zero resistance, are also perfect diamagnets. The hallmark of this perfect diamagnetism is that an applied magnetic field will be expelled from the inside of a superconductor. The phenomenon of flux expulsion is known as the Meissner effect. By making a modification to Ohm's law to allow for zero resistivity, F. and H. London introduced an equation in 1934 which mathematically describes both the Meissner effect and the zero resistance using a two-fluid model. The two-fluid model supposes that the total density n of electrons in the superconductor is composed of superconducting n_s and normal n_n electrons with the total given by the sum, $n = n_s + n_n$. The London formulation also introduced the London penetration depth λ_l which is the characteristic length that a magnetic field will penetrate into a superconductor in setting up the diamagnetic shielding currents for flux expulsion. A macroscopic phenomenological theory of superconductivity was developed by Ginzburg and Landau in 1950 based on the Landau theory of second-order phase transitions.

From the discovery of superconductivity through the early fifties, attempts at using superconductors to construct high-field magnets had failed due to the low critical current I_c, or equivalently the low critical magnetic field H_c. When elemental superconductors are exposed to a magnetic field $H \geq H_c$, superconductivity is destroyed, and the material goes to the normal state. For niobium, the critical field is $H_c \approx$ 0.2 T. In 1953, Pippard introduced another characteristic length which is important to understanding superconductivity, the coherence length ξ of the superconducting electrons. In 1957 A. Abrikosov theoretically predicted the existence of two types of superconductors which are differentiated by the relative size of their penetration depths and coherence lengths. In a type-I superconductor λ_l is less than ξ, and the superconducting state persists in an applied magnetic field until the critical field value H_c is reached forcing the material into the normal state. In contrast, if λ_l is greater than ξ, the superconductor is a type-II which has two critical fields. Below the lower

critical field H_{c1}, the Meissner state is preserved, but between H_{c1} and the upper critical field H_{c2} where superconductivity is destroyed, there exists an intermediate state where quantized units of magnetic flux, $\Phi_0 = h/2e = 2.07 \times 10^{-15}$ Wb can penetrate the material in a vortex lattice (Abrikosov vortices) without destroying superconductivity. Abrikosov's prediction of a type-II superconductor was first realized in the 1950's with the niobium alloy compound Nb_3Sn and later culminating with the discovery in 1973 by J. Gavaler of Nb_3Ge which has $T_c = 23$ K and $H_{c2} = 38$ T. The type-II niobium alloys provided a material suitable for the construction of high field magnets.[2]

The first fully quantum-mechanical microscopic theory of superconductivity was published in 1957 by J. Bardeen, L. Cooper, and R. Schfieffer. The BCS theory predicted that the superconducting electrons form "Cooper pairs". The paired electrons no longer obey the Fermi statistics of unpaired electrons and thus can all act in a single coherent manner. Using BCS theory to examine tunneling phenomena, B. Josephson deduced in 1962 that very interesting quantum mechanical effects are manifested when Cooper pairs tunnel between two superconductors separated by a thin non superconducting layer. The Josephson effect comprises a large part of this thesis work and will be described in detail later.

A new era in superconductivity began in 1986, when G. Bednorz and A. Müller reported that they had found evidence of superconductivity at 30 K in ceramic materials of the Ba-La-Cu-O system.[3] This discovery was deemed so important that Bednorz and Müller were awarded the Nobel prize less than two years later. The discovery of a new class of superconducting ceramics brought intense research, and within a year P. Chu had found another superconducting copper-oxide compound $YBa_2Cu_3O_{7-\delta}$ (YBCO) which has an astonishingly high T_c of 92 K and an H_{c2} of more than 100 T. The highest reported values of T_c rose rapidly with H. Maeda et al . finding a T_c of 110 K in $Bi_2Sr_2Ca_2Cu_3O_{10}$, and Z. Sheng *et al* . finding a T_c of 125 K in $Tl_2Ba_2Ca_2Cu_30_{10}$, both in 1988. The highest T_c to date is in the compound $Hg_2Ca_{n-1}Cu_{n-2}O_{2n+2+\delta}$ which has a T_c of 134 K that can be increased to 164 K under very high pressure.[4] All of these high-T_c compounds are type-II su-

perconductors with very short coherence lengths, anisotropic crystal structures, and quasi-two-dimensional conduction in CuO_2 planes. The high-T_c materials are unlike all previously known superconductors making them interesting and novel materials for study.

The bulk of my thesis work is on the compound YBCO, although many results presented here can be extended to other high-T_c cuprates in general. In the next chapter I will present the structural and electrical properties of YBCO to motivate the study of the microwave-frequency power dependence in YBCO thin-films, grain boundaries, and Josephson junctions in the subsequent chapters.

Chapter 2

Structural and Electrical Properties of $YBa_2Cu_3O_{7-\delta}$ (YBCO).

This chapter provides an overview of some important physical properties of the high-temperature superconductor $YBa_2Cu_3O_{7-\delta}$ to provide a necessary background for the rest of the research presented in this thesis. First, the crystalline structure of YBCO is presented and discussed to demonstrate how the anisotropic, planar structure of the material affects its physical properties. Next, the choice of substrate materials and the thin-film growth techniques employed to prepare the devices used in this study are examined, along with the resulting microstructure of the thin films. This chapter concludes with a brief look at some of the measured dc electrical properties of the YBCO thin films studied in this work.

2.1 Crystalline structure of YBCO

The superconducting properties of the compound $YBa_2Cu_3O_{7-\delta}$ are largely determined by the content and arrangement of the oxygen atoms in the unit cell. As the oxygen content is increased from O_6 to O_7 ($\delta = 1$ to $\delta = 0$), the material changes from an insulator to a metallic conductor which is superconducting at a temperature

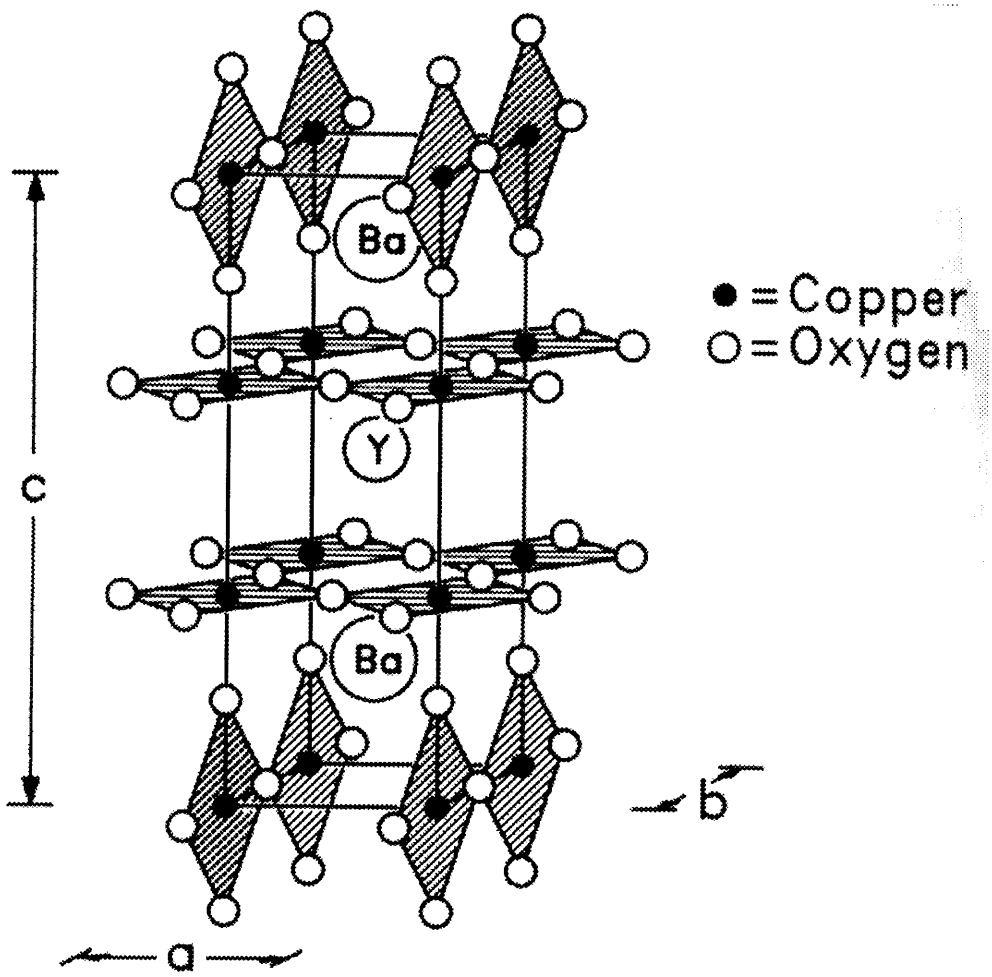

Figure 2-1: This figure shows the unit cell of $YBa_2Cu_3O_7$ emphasizing the copper-oxygen bonds. The supercurrents flow in the CuO_2 conduction planes on either side of the Y layer, while the CuO chains above and below the Ba act as charge reservoirs. From Beyers et al.[5]

T equal to or below the critical temperature value $T \leq T_c$. The oxygen deficient insulating state occurs for the stochiometric range $0.6 \leq \delta \leq 1.0$, while superconductivity exists in the range $0 \leq \delta < 0.6$. The highest T_c value of 94 K occurs when the oxygen content is $\delta = 0.07$ with the T_c value decreasing slightly to 92 K when the oxygen is increased to $\delta = 0$.[2] As the amount of oxygen in the unit cell is increased, the transition from an insulating material to a metallic-superconducting phase is accompanied by a continuous transition of the YBCO unit cell from a tetragonal to an orthorhombic structure.[5] The compounds studied in this thesis have a slightly lower

than ideal oxygen content resulting in a typical T_c value of 90 K.

The structure of $YBa_2Cu_3O_7$ is shown in Fig.2-1. The unit cell has a modified perovskite structure which is tripled along the c-axis. The material has a highly anisotropic layered structure with stacked copper-oxygen layers in the basal a-b plane separated along the c-axis by barium oxide and yttrium layers. There are CuO "chains" shown at the top and bottom of Fig.2-1 above and below the BaO layers and CuO_2 "planes" between the BaO and Y layers. The superconductivity occurs quasi-two-dimensionally in the CuO_2 planes, while the CuO chains act as charge reservoirs. The charge carriers are holes. The dimensions of the orthorhombic unit cell are, $a = 3.88$ Å, $b = 3.84$ Å, $c = 11.63$ Å. [2, 6, 7]

$YBa_2Cu_3O_7$ is a strongly type-II superconductor with a very short anisotropic coherence length. In the basal a-b plane, the coherence length is isotropic with a value $\xi_{ab} \approx 15$Å, while along the c-axis the coherence length is only $\xi_c \approx 4$Å. Since ξ_c is less than the length of the unit cell, and about the same as the spacing between copper-oxide planes, the coupling in this direction is very weak and conduction along the c-axis occurs only through tunneling. The supercurrents with a high critical-current density, J_c, propagate in the basal a-b plane. In the a-b plane, the relatively small value of ξ_{ab} makes the superconducting properties of this material very sensitive to small scale structural defects, such as twin boundaries, oxygen deficiencies, grain boundaries, stacking faults or other material defects. For these type-II superconductors, the penetration depth is large and anisotropic, with $\lambda_{ab} \approx 2000$ Å and $\lambda_c \approx 6000$ Å.

2.2 Synthesis and Microstructure of YBCO Thin Films

YBCO has a critical current density J_c three to four orders of magnitude higher in thin films than in the bulk material. This is a consequence of the short coherence length which is sensitive to the numerous extended defect structures found in the

bulk material. In addition to a high J_c, thin films also have greater structural reproducibility and consistency of T_c and J_c values which is desirable for applications. At microwave frequencies, high-T_c thin-films can be used for devices such as filters, delay lines, mixers, and multiplexers. All the measurements presented in this thesis were performed on YBCO thin-film devices. Therefore, before discussing any experimental results, it is useful to examine the techniques used to produce the films and the microstructural characteristics of the films.

2.2.1 Substrates

When determining which substrate material is suitable for deposition of YBCO thin films, two important properties are a good lattice match and low chemical reactivity. Since the material is planar, with the high-J_c supercurrents flowing in the basal a-b plane, it is desirable to grow c-axis oriented films. A c-axis orientation means that the c-axis of the YBCO unit cell is oriented perpendicular to the surface of the substrate. Single-crystal substrates with four-fold surface symmetry and a lattice constant of 3.8 to 3.9 Å are good candidates for growing epitaxial films. If the lattice match is not adequate, or the material is chemically reactive with YBCO, a buffer layer can be deposited on the substrate before YBCO deposition. Some single-crystal materials that have been successfully used as substrates for growing YBCO films include $SrTiO_3$, Al_2O_3 (sapphire), MgO, $YAlO_3$, $LaAlO_3$, $LaGaO_3$, and YSZ.

The YBCO thin films used in this study were mostly prepared using sapphire substrates, with a few on $LaAlO_3$. $LaAlO_3$ is used because it has a good lattice match ($a_0 = 3.793$Å) and it is very inert. However, for microwave applications, sapphire has a lower dielectric constant ($\epsilon_r = 9.3$ (Al_2O_3), $\epsilon_r = 24$ ($LaAlO_3$)) and much lower loss tangent ($\tan\delta = 3.8 \times 10^{-8}$ (Al_2O_3), $\tan\delta = 7.6 \times 10^{-6}$($LaAlO_3$) at 10 GHz and 77 K) which must be considered.[8, 9] Sapphire also has a high thermal conductivity that helps reduce heating effects in the thin films. Most of the films used in this study were grown on r-plane ($1\bar{1}02$) sapphire ($a_0 = 3.48$ Å) after an epitaxial buffer layer of CeO_2 was deposited to facilitate lattice matching and prevent chemical reactivity.[10]

2.2.2 Deposition technique

The YBCO films were produced using a pulsed laser deposition technique. This is an in-situ process, in other words, the crystalline structure of the YBCO film develops as it is deposited onto the substrate. In the pulsed-laser deposition process, a laser beam is focused onto a target pellet of stoichiometric $YBa_2Cu_3O_7$, evaporating some of it. The substrate is located adjacent to the target and the plume created by the laser evaporation deposits the YBCO on the substrate. This is done in an O_2 environment at a pressure of 800 mTorr and at a temperature of 760° C. The films were grown to a thickness of 1400Å. The YBCO deposition was performed by L. R. Vale at NIST Boulder.[10]

After YBCO deposition, the films are patterned into test structures using standard photolithographic techniques and etched using a 0.25% phosphoric acid solution.

2.2.3 Microstructure

Thin films of YBCO have numerous microstructural defects that affect the electromagnetic properties. Microstructural investigations using probing techniques including x-ray diffraction, SEM, TEM, AFM, energy-dispersive spectroscopy, and Raman spectroscopy have revealed numerous point, line, and planar defects as well as inclusions and precipitates in YBCO thin films.[11, 12, 13] Point defects such as oxygen vacancies, or line defects such as microcracks can actually enhance the J_c of the thin film by acting as pinning sites for Abrikosov vortices. Precipitated crystallites of CuO_2 are often found on the surface of the film along with Y_2O_3 which also forms inclusions within the film. Figure 2-2 shows an SEM micrograph of one of the films used in this work. A matrix of grains of YBCO, which appear light grey, separated by grain boundaries, which appear dark grey, constitute the bulk of the micrograph. The white spots in Fig.2-2 are precipitates of CuO_2, while the smaller black spots are holes in the film. The correlation between microstructural properties of the films and their electrical properties is an area of ongoing research.

YBCO thin films typically do have a granular composition. The effect of the grain

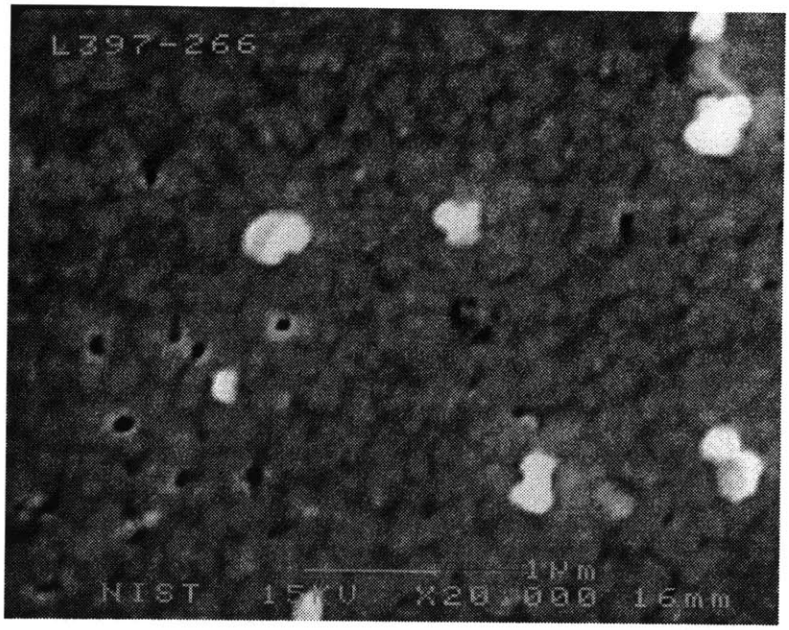

Figure 2-2: SEM micrograph of one of the YBCO on sapphire thin films used in this study. A matrix of grains of YBCO, which appear light grey, separated by grain boundaries, which appear dark grey, constitute the bulk of the micrograph. Also visible are white spots which are precipitates of CuO_2 and smaller black spots which are holes in the film.

boundaries and the orientation of the grains on the electrical properties of the material make up a large part of this thesis. In c-axis-oriented films, there are typically some grains of a-axis-oriented material. It has been found that films with the highest J_c's have the smallest fraction of a-axis-oriented grains.[14] In-plane misorientations of the basal-plane a-axis between c-axis oriented grains are also observed. These in-plane grain boundaries can be characterized by a misorientation angle θ, which is the degree of rotation of the a-axis across the boundary separating the c-axis-oriented grains. The films can further be characterized by their mosaic spread, which gives the range of θ values found throughout the film. Typical mosaic spreads are 2°, which means values of θ ranging from 0-2° are distributed amongst the grains in the film, while larger mosaic spread values have been reported.[13, 14] The in-plane grain boundaries

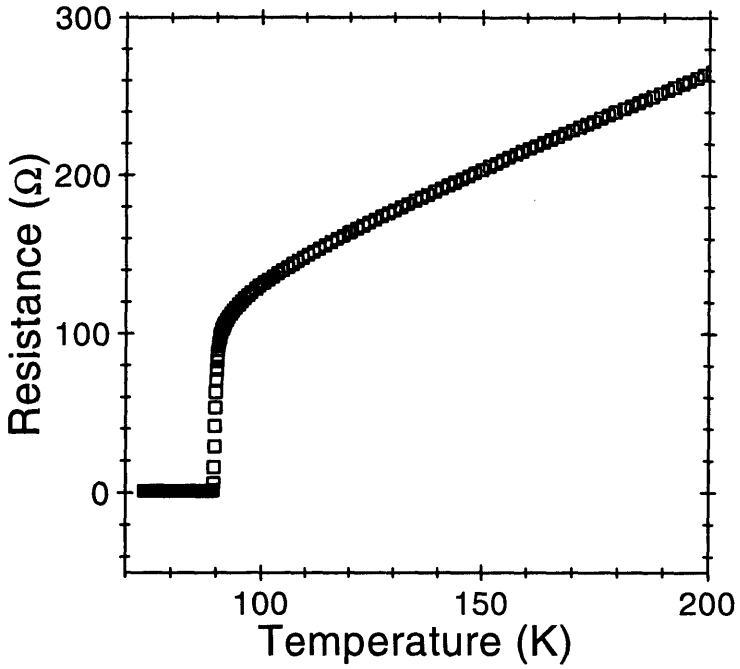

Figure 2-3: Resistance as a function of temperature, showing the transition from the normal resistive state to the superconducting state at the critical temperature $T_c = 89.8$ K. This measurement was performed on a thin film of the high-T_c compound $YBa_2Cu_3O_{7-\delta}$ (YBCO).

will be examined thoroughly later in this thesis.

2.3 dc Electrical properties of YBCO thin films

Microwave-frequency (rf) electrodynamic properties of YBCO thin films are the primary focus of this thesis. To provide a basis for comparison with rf measurements, dc measurements were performed on many of the same films whose rf properties were studied. A resonator line for rf measurements and a four point test structure for performing dc measurements are patterned from a YBCO film grown on a single 1 cm x 1 cm substrate. Both the dc and rf lines have the same width. The dc measurements require silver electrical contacts to be deposited on the YBCO and therefore cannot be done on the resonator line used for rf measurements. After the dc measurements are performed, the dc test structure is removed by etching to prevent spurious coupling

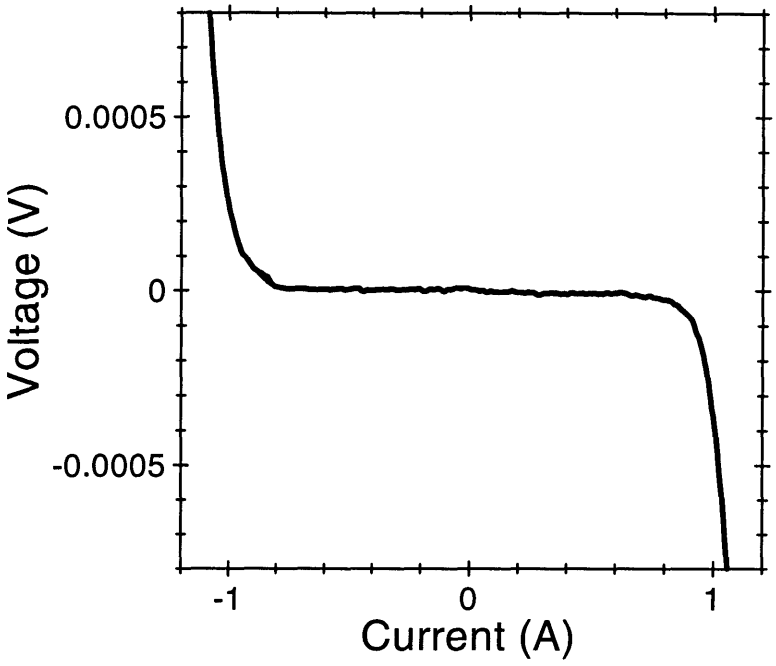

Figure 2-4: Voltage as a function of applied current (I-V) measurement used to determine I_c. This measurement was performed at 76K. The critical current is determined using a 20-μV voltage criterion.

to the resonator line during the rf measurements. Some dc measurements performed on a YBCO film grown on a single-crystal sapphire substrate are presented below.

A typical resistance versus temperature measurement used to determine T_c for the films used in this thesis is shown in Fig.2-3. The resistance is seen to decrease linearly with temperature until T_c is reached, and the resistance abruptly drops to zero. This measurement has 10-90% transition width of 1.6 K with a midpoint resistive T_c of 89.8 K which is a typical result seen in the samples measured for this work. All the samples presented throughout this thesis had a T_c of 89.5 K $\pm$ 0.5 K. Films showing transitions with these characteristics are generally regarded to be of good quality.[2, 15]

Another useful dc characterization indicator to gauge the quality of a superconducting thin film is the magnitude of J_c as a function of temperature. The critical current density is determined from the critical current, $J_c = I_c/A$, where A is the cross sectional area of the patterned film being measured. The value of I_c is determined from a transport I-V measurement, where the voltage response as a function of applied dc current is measured by the standard four-point technique. A typical

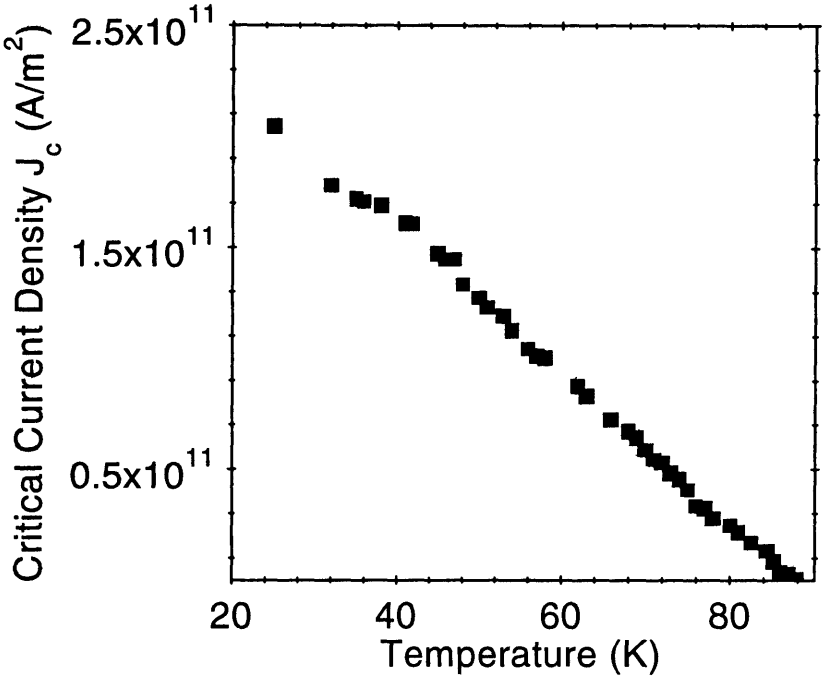

Figure 2-5: Critical current density J_c in A/m^2 as a function of temperature as determined from an I-V plot as in Fig.2-4 taken at each temperature shown.

I-V curve taken at 76 K is shown in Fig.2-4. Throughout this thesis, the I_c is defined to be the current level where the voltage reaches 20 μV. The voltage results from the motion of Abrikosov vortices giving rise to a flux-flow resistivity. The J_c as a function of temperature, as determined from an I-V plot taken at each temperature point presented, is shown in Fig.2-5. The dependence of J_c on T is linear. The films used on this study have a $J_c = 3 \times 10^{10}$ A/m^2 at 77 K and $J_c = 2 \times 10^{11}$ A/m^2 at 30 K which are typical values obtained for high-quality YBCO thin films.[16]

Chapter 3

Microwave-Frequency Power Dependence of the Surface Impedance of YBCO Thin Films

The microwave-frequency (rf) surface impedance of YBCO thin films is an important parameter for potential device applications and a sensitive probe of the physical properties of high-temperature superconducting systems. YBCO is an attractive material for active and passive microwave device applications, because rf power losses are substantially lower than for copper at liquid nitrogen temperatures (77K). However, the surface impedance of YBCO is dependent on rf power, becoming nonlinear at power levels needed for device applications. The nonlinearities in the surface impedance result in power losses, harmonic generation, and intermodulation distortion, all of which limit potential device applications.

One of the goals of this thesis work is to understand whether the observed power dependence of the surface impedance is due to extrinsic properties resulting from materials processing or due to an intrinsic feature of high-T_c superconductors. This chapter first reviews some basic theoretical aspects for calculating the surface impedance in superconducting thin films. Next, the microwave-frequency measurement technique used throughout this work is explained, and the measurement results showing the power dependence of the surface impedance in YBCO films are presented. This

chapter concludes with an overview of some possible explanations for the observed dependence of the surface impedance of YBCO thin films on rf power, which is also known as power handling.

3.1 Microwave-Frequency Electrodynamics

3.1.1 Surface Impedance

The concept of surface impedance originates from classical electromagnetic theory. If one considers a good conductor occupying the half-space $z > 0$ with a plane-wave normally incident upon it, most of the power in the plane wave will be reflected from the surface, while some power will be dissipated as heat by currents induced on the conducting surface within the skin depth of the material. From Maxwell's equations, the complex surface impedance Z_s is defined as the ratio of electric to magnetic fields at the surface,

$$Z_s = \frac{E}{H} = \sqrt{\frac{i\omega\mu_0}{\sigma}} = R_s + iX_s \tag{3.1}$$

where ω is the angular frequency of the plane wave, $\sigma = \sigma_1 - i\sigma_2$ is the complex conductivity of the conducting material, R_s is the surface resistance, and X_s is the surface reactance.[17, 18] To calculate the surface impedance of a superconductor, the complex conductivity $\sigma = \sigma_1 - i\sigma_2$ is obtained from the two-fluid model.

3.1.2 Two-Fluid Model

At any finite temperature, a superconductor has a density of normal charge carriers n_n and superconducting carriers n_s, such that the total carrier density is equal to the sum $n = n_n + n_s$. Consequently, the total conductivity σ is the sum of the normal and superconducting parts $\sigma = \sigma_n + \sigma_s$. Substituting for a sinusoidially varying superconducting current density $J_s = \sigma_s E e^{i\omega t}$, into the first London equation yields σ_s,

$$\mu_0\lambda_l^2\frac{dJ_s}{dt} = E \Rightarrow \sigma_s = \frac{1}{i\mu_0\omega\lambda_l^2} \tag{3.2}$$

[19] which is purely imaginary and does not contribute to rf power losses. The simplest expression one can use for σ_n comes from the Drude model of electrical conductivity,

$$\sigma_n = \frac{\sigma_0}{1 - i\omega\tau}, \; \sigma_0 = \frac{n_n e^2 \tau}{m_e} \tag{3.3}$$

[20] where e and m_e are the electron charge and effective mass respectively, and τ is the relaxation time for electron scattering. Typically, $10^{-13} > \tau > 10^{-15} s$ in YBCO samples. At microwave frequencies, 300 MHz to 300 GHz, the product $\omega\tau \ll 1$, and consequently, the total complex conductivity is given as

$$\sigma = \sigma_1 - i\sigma_2 = \frac{n_n e^2 \tau}{m_e} - i\frac{1}{\mu_0 \omega \lambda_l^2} \tag{3.4}$$

with $\sigma_1 \ll \sigma_2$. Then, substituting Eq.3.4 into Eq.3.1 yields

$$Z_s = i\sqrt{\frac{\omega\mu_0}{\sigma_2}}\left(1 + i\frac{\sigma_1}{\sigma_2}\right)^{-1/2} \approx \frac{\sigma_1}{2\sigma_2^2 \lambda_l} + i\omega\mu_0\lambda_l = R_s + iX_s \tag{3.5}$$

giving the surface impedance Z_s in the two-fluid model. The surface resistance in the two-fluid model is proportional to the frequency squared, $R_s \propto \omega^2$, compared to $R_s \propto \omega^{-1/2}$ for a normal conductor given in Eq.3.1. The surface reactance is inductive, $X_s = \omega L_k$ where $L_k = \mu_0 \lambda_l$ is the kinetic inductance of the superconducting charge carriers. The BCS theory gives $\sigma_1 \propto e^{-\Delta/kT}$ which predicts $R_s \longrightarrow 0$ with $T \longrightarrow 0$ and that R_s is independent of the rf current amplitude below the critical current. Experimentally, high-T_c materials have a residual R_s even as $T \longrightarrow 0$ and a dependence on rf current which cannot be explained by the conventional theories of superconductivity.

3.1.3 Penetration Depth

The magnitude of the penetration depth λ_l and the dependence of λ_l on temperature and microwave field amplitude are important considerations when analyzing Z_s in this chapter and for quantifying Josephson junction effects in the next chapter. It has been determined empirically [21] that the temperature dependence of λ_l is given by

$$\lambda_l(T) = \frac{\lambda_l(0)}{\sqrt{1 - (\frac{T}{T_c})^4}}. \tag{3.6}$$

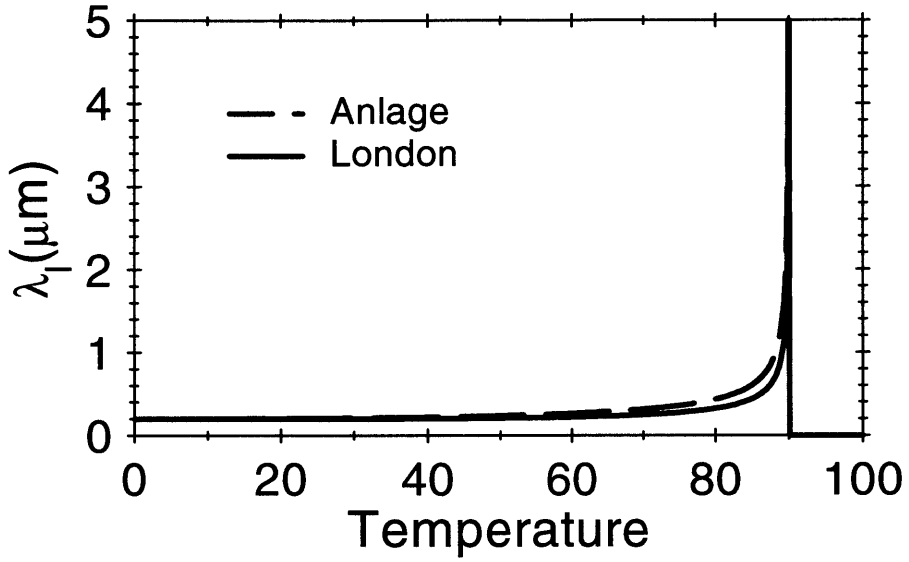

Figure 3-1: Temperature Dependence of the penetration depth $\lambda_l(T)$ as determined from the two-fluid model, and from microwave measurements on YBCO by Anlage et al.[22] for $T_c = 90$K and $\lambda_l(0) = 0.2\mu$m.

More recent microwave frequency measurements by Anlage et al.[22] on YBCO thin films show a temperature dependence of $(T/T_c)^2$ rather than the $(T/T_c)^4$ dependence given in Eq.3.6. In either case, the temperature dependence of λ_l is relatively insignificant at temperatures much below T_c. A plot comparing the two temperature dependencies is shown in Fig.3-1 for $T_c = 90$ K and $\lambda_l(0) = 0.2\ \mu$m. For the temperatures of interest in this study, $T = 4.2$ to 77 K, the variation of λ_l with T is small in either case. The magnitude of $\lambda_l(0)$ is anisotropic, having one value in the basal a-b plane, $\lambda_{lab}(0) \approx 0.2\ \mu$m, and another in the c-axis direction, $\lambda_{lc} \approx 0.6\ \mu$m[2, 23]. The high J_c supercurrents flow in the a-b plane. Therefore it is λ_{lab} that determines the relevant penetration depth and will be referred to as λ_l for the rest of this thesis. The patterned c-axis-oriented YBCO films used in this study have a thickness, $d \approx 0.14\mu\text{m} \approx \lambda_l$, so that a uniform field penetration through the thickness of the film can be assumed. On the other hand, the width of the lines is $w = 150\mu\text{m} \gg \lambda_l$, resulting in a very nonuniform field distribution across the width of the line.

The dependence of λ_l on microwave current amplitude is manifested as a change in X_s. Nguyen et al.[23] have measured the variation of λ_l in YBCO thin films with

microwave field amplitude over the power ranges used in this work, and determined that the variance is less than 10 %. The relation of $\Delta\lambda_l$ to ΔX_s is outlined in the next section. Unless otherwise noted, throughout this thesis λ_l is assumed to be constant with a value $\lambda_l = 0.2\,\mu$m.

3.2 Measurement Techniques and Results

3.2.1 Measuring the Surface Impedance Using a Stripline Resonator

The surface impedance of superconducting thin films can be directly measured using resonator techniques. In this study, a stripline-resonator shown schematically in Fig.3-2 is used to measure Z_s. The stripline geometry is defined as having a center conductor, an upper and lower ground plane, and a symmetric dielectric. This geometry allows for the propagation of TEM modes which are the easiest modes to analyze. The center conductor consists of a patterned transmission line that is one half wavelength long at the fundamental resonance frequency. The center line is coupled to the external measurement circuits by capacitive gaps. The length of the line is chosen to yield a fundamental resonant frequency $f_1 \approx 3$ GHz, with overtone resonant modes at integer n multiples of f_1, $f_n \approx nf_1$. The width of the line is 150 μm. Using 0.5 mm thick sapphire dielectric substrates results in a characteristic transmission line impedance $Z_0 = 50\,\Omega$. The upper and lower ground planes act to confine the electromagnetic fields within the stripline structure, minimizing radiative power losses and spurious coupling to other conductors. The stripline geometry also concentrates most of the currents in the center conductor which allows high current densities to be attained at modest levels of input power. The configuration in Fig.3-2 consisting of three YBCO films on three separate substrates is clamped together in a gold-plated copper package with rf coaxial connectors for measurement. The ground planes and center conductor films were all prepared as described in section 2.2.

The surface impedance as a function of rf current is obtained by directly mea-

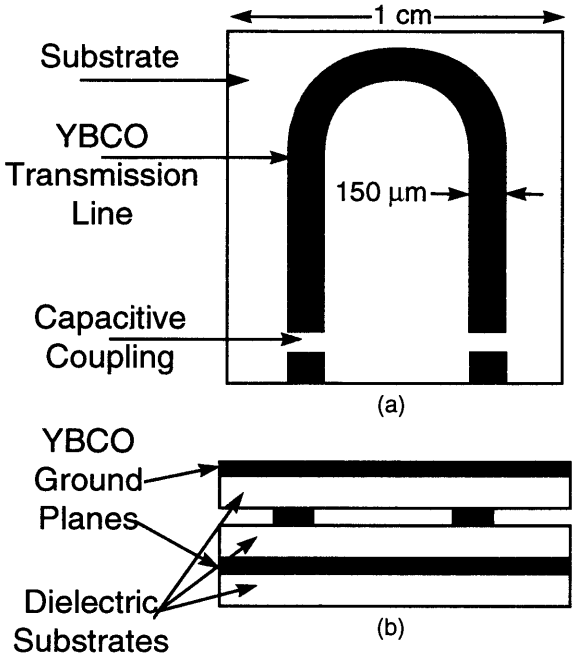

Figure 3-2: Stripline resonator schematic. (a) Shows a top view of a capacitively-coupled YBCO transmission line which is patterned from a YBCO thin film on a sapphire substrate. (b) Shows a cross sectional view of a stripline resonator. The transmission line in (a) has been placed between two unpatterned thin-film YBCO ground planes. In both (a) and (b), the YBCO thin film is in black, and the substrate is in white.

suring the quality factor Q, resonant frequency f_n, and the insertion loss IL of the stripline resonator.[24, 25] The experimental setup used to perform the measurement is shown schematically in Fig.3-3. A vector network analyzer generates an rf signal at a set power level, repeatedly sweeping through a range of frequencies in the neighborhood of the resonant frequency. This signal can then be attenuated or amplified as needed before it travels to the stripline resonator, that is in a cryogenically controlled

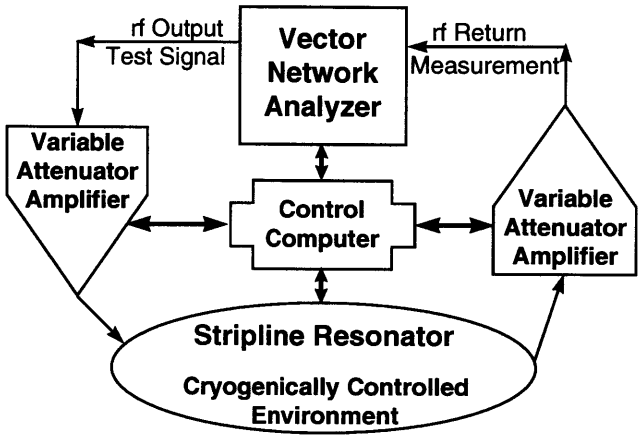

Figure 3-3: Schematic of the experimental setup used to measure the power dependence of Z_s in YBCO thin films. The vector network analyzer generates an rf signal sweeping through a range of frequencies centered about the resonant frequency f_n at a set power level. The power level can be adjusted by the variable attenuator/amplifier before the rf signal is sent to the stripline resonator being tested. The resonator is at a controlled stable temperature. The signal transmitted through the resonator can again be amplified or attenuated before returning to the vector network analyzer which records the magnitude of the transmitted signal as a function of frequency. A computer is used to control the instruments and record the measured data.

environment at a fixed temperature that can be set to any desired temperature from 5 to 300 K. Temperature stability is critical for attaining a reliable measurement. To this end, I designed and constructed a custom-built cryostatic microwave probe which provided a temperature stability of one-part per thousand over a measurement period greater than 48 hours. The probe is cooled by using a liquid helium dewar so that the probe and dewar together constitute the cryogenically controlled environment shown in Fig. 3-3. The cryostatic probe is also magnetically shielded and constructed from

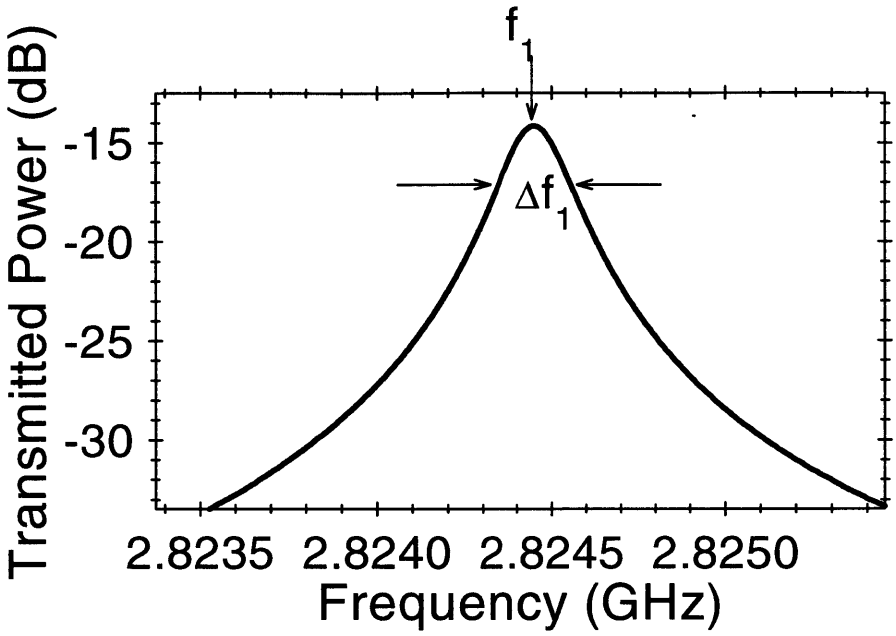

Figure 3-4: The results of a measurement using the experimental setup shown in Fig.3-3. This shows the power transmitted through the resonator as a function of frequency with the fundamental resonant frequency f_1 and the 3 dB bandwidth Δf_1 shown. This data corresponds to a Q of 13400 and an IL of 8.5 dB.

non-magnetic materials to ensure that the ambient magnetic field is $B < 10^{-7}$ T, thereby significantly reducing the possibility that stray magnetic flux will influence the measurement results. The rf signal that is transmitted through the resonator can then be attenuated or amplified before returning to the vector network analyzer which records the magnitude of the transmitted signal as a function of frequency over the same frequency range as the output signal. The attenuators and amplifiers allow measurements to be performed over a power range from -80 to 30 dBm. All the components of the experimental system are calibrated prior to measurement so that the power level delivered to and transmitted through the resonator is known to a 0.05 dB accuracy. The insertion loss is determined as the difference between the power delivered to the resonator and the power transmitted through the resonator at the resonant frequency. A computer is used to control the individual instruments in the experimental setup and record the measurement results.

Figure 3-4 shows the results of a typical measurement using the experimental setup shown in Fig.3-3. This shows the microwave power transmitted through the stripline resonator as a function of frequency. The transmitted power peaks at the resonant frequency f_1. The level of transmitted power falls off when the frequency is above or below the resonant value. The resonance curve fits a Lorentzian function, and hence the loaded Q, given as Q_l, is calculated as the ratio of f_1 to the frequency bandwidth Δf at a level 3 dB down from f_1 on either side, $Q_l = f_1/\Delta f$.[18] The measurement shown here has a $Q = 13400$ and an IL of 8.5 dB. At high levels of rf input power, the resonance curves become distorted and no longer fit a Lorentzian function. However, the error in Q calculated from the 3 dB bandwidth is found to be less than 10%[26, 27], and hence, the 3 dB criterion will be used to determine Q throughout this thesis. The insertion loss is determined as the amount of power dissipated in the stripline resonator. A full measurement at a given temperature involves recording the Q_l, IL, and f_n at a given calibrated rf power level and then increasing the power and repeating the measurement throughout the desired power range.

The surface resistance is obtained from the unloaded quality factor Q_u, which is the Q of the superconducting resonator. The measured Q_l is slightly smaller than Q_u due to the loading effect of the circuitry external to the resonator. The Q_u is determined from the voltage insertion ratio r_v which is related to the insertion loss, IL, by $IL = -20 \log r_v$. The Q_u is given by[24]

$$Q_u = \frac{Q_l}{1 - r_v} \tag{3.7}$$

and using this relation, R_s is calculated from the definition of Q as follows. The Q is the figure of merit which is proportional to the ratio of the energy stored in the resonator to the power dissipated. The power dissipated per unit volume is $(1/2)\rho J_{rf}^2$, where J is the current density in the stripline resonator and ρ is the two-fluid-model resistivity, given as

$$\rho = Re(\frac{1}{\sigma}) = \frac{\sigma_1}{\sigma_1^2 + \sigma_2^2} \approx \frac{\sigma_1}{\sigma_2^2} \tag{3.8}$$

using $\sigma_1 \ll \sigma_2$. The energy is stored in the rf magnetic field and this is given by

$(1/2)\mu_0 H_{rf}^2$ per unit volume. Defining the angular frequency of the resonant mode, $\omega_n = 2\pi f_n$, R_s is determined by

$$\frac{1}{Q_u} = \frac{1}{\omega_n}\frac{Power Lost}{Energy Stored} = \frac{\frac{\sigma_1}{\sigma_2^2}\int J_{rf}^2 dAdl}{\omega_n \int \mu_0 H_{rf}^2 dAdl} = \frac{2R_s\lambda_l \int J_{rf}^2 dA}{n\omega_1 \int \mu_0 H_{rf}^2 dA}. \tag{3.9}$$

The final term in Eq. 3.9 is obtained by integrating over l using the fact that J_{rf} and H_{rf} have the same functional dependence on l, and then substituting Eq.3.5 to obtain the final result. The ratio of the area integrals in Eq.3.9 is a constant geometrical factor Γ which is determined for $f_1 = 3$ GHz by the method of Sheen *et al.*[28] For a given resonant mode number n, R_s is given by

$$R_s = \frac{n}{2\Gamma Q_u} = \frac{0.67n}{Q_u}(\Omega) \tag{3.10}$$

Typical low power Q_u values of 10,000 to 30,000 translate to R_s values of 67 to 22 $\mu\Omega$ respectively for the $n = 1$ resonant mode.

Using an equivalent circuit model, the current in the center conductor of the stripline resonator at resonance can be obtained from the measured data. The equivalent circuit of the transmission line resonator is shown in Fig. 3-5(a).[29] The components of the equivalent resonator circuit in Fig.3-5(a): the capacitance C, the inductance L, and the resistance R, are derived from the Q_u, f_n, and Z_0 of the resonator. Specifically,

$$C = \frac{n\pi}{2Z_0\omega_n} \tag{3.11}$$

$$L = \frac{1}{\omega_n^2 C} \tag{3.12}$$

$$R = \frac{2Q_u Z_0}{n\pi} = \frac{Q_u}{\omega_n C} \tag{3.13}$$

where n is the resonant mode number. In addition, C_c represents the capacitive coupling to the resonator, R_l is the load resistance external to the resonator, and V_s is the source voltage. The voltage at resonance can be calculated by transforming the circuit of Fig. 3-5(a) into an equivalent parallel circuit.[24] For $\omega_n C_c \ll 1/R_L$, the equivalent circuit is given in Fig. 3-5(b). The current generated by the source I_s, is given by $I_s = j\omega_n C_c V_s$, where V_s is the voltage generated by the source; and R_p the

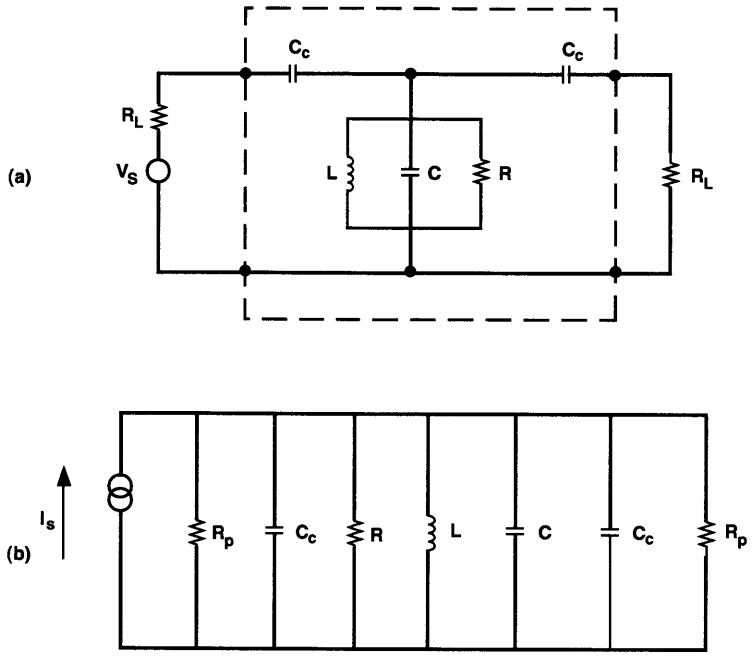

(a) Shows the equivalent circuit for a transmission line resonator. (b)

Figure 3-5: Shows the equivalent parallel circuit of (a). The circuit in (b) is used for calculation of the resonator current at resonance.[24]

equivalent parallel source resistance is $R_p = 1/(\omega_n^2 C_c^2 R_L)$. At resonance, the voltage across the resonant circuit is

$$V_r = \frac{RR_p}{2R + R_p} I_s. \tag{3.14}$$

The V_L defined as the voltage across the load resistance R_L, is $V_L = [R/(2R+R_p)]V_s$. The voltage insertion ratio for the resonator r_v is $r_v \equiv |2V_L/V_s| = 2R/(2R+R_p)$ which is the same as the r_v related to the insertion loss by $IL = -20 \log r_v$ as introduced in Eq.3.7. The resonant voltage V_r is then given by

$$V_r = j\sqrt{r_v(1 - r_v)\frac{R}{2R_L}} V_s \tag{3.15}$$

and rewritten using expressions 3.11, 3.12, and 3.13,

$$V_r = j\sqrt{\frac{r_v(1 - r_v)Q_c Z_0}{n\pi R_L}} V_s. \tag{3.16}$$

The available power P from the source is

$$P = \frac{V_s^2}{4R_L} \tag{3.17}$$

and the current I_0 at the standing wave peaks in the resonator at resonance is

$$|I_0| = \frac{|V_r|}{Z_0}. \tag{3.18}$$

Substituting (3.17) and (3.18) into (3.16) yields:

$$|I_0| = \sqrt{\frac{r_v(1-r_v)4Q_cP}{n\pi Z_0}}. \tag{3.19}$$

The current I_0 in Eq.3.19 is the rms value of the current at the peaks of the resonant standing waves. Then, for a transmission line of length l in the y direction, the resonant rf current is

$$I_{rf} = I_{rf}(z,t) = I_0 \sin(\frac{n\pi y}{l}) \cos(\omega t). \tag{3.20}$$

This expression for rf current will be used throughout this thesis.

From the dependence of the measured resonant frequency on rf current, $f_n(I_{rf})$, the change in surface reactance as a function of rf current $\Delta X_s(I_{rf})$ is obtained as follows. For the resonant circuit shown in Fig.3-5(a), the angular resonant frequency is given by Eq.3.12. Assuming a constant capacitance, any change in resonant frequency with increasing rf current is due to inductive changes. Hence the following equation is obtained,

$$-2\frac{\Delta f_n}{f_n} = \frac{\Delta L}{L}. \tag{3.21}$$

The total inductance L is equal to the sum of the geometrical and kinetic inductances $L = L_g + L_k$, where $L_g \gg L_k$, and is obtained from the inductive energy relation for a superconducting transmission line [21],

$$\frac{1}{2}LI^2 = \frac{1}{2}\mu_0 \int (H_{rf}^2 + \lambda_l^2 J_{rf}^2) dA. \tag{3.22}$$

From Eq.3.22 it then follows that the change ΔL due to a change in the penetration depth $\Delta\lambda$ is given by,

$$\frac{\Delta L}{L} = \frac{2(\Delta\lambda_l)\lambda_l \int J_{rf}^2 dA}{\int H_{rf}^2 dA} = \Gamma\mu_0\omega\Delta\lambda_l = \Gamma\Delta X_s \tag{3.23}$$

using Eqs.3.5 and 3.9. Then the change in surface reactance as a function of rf current is given as

$$\Delta X_s(I_{rf}) = -2.78\frac{\Delta f_n}{f_n}(\Omega), \text{ where } -\Delta f_n = f_n(0) - f_n(I_{rf}). \tag{3.24}$$

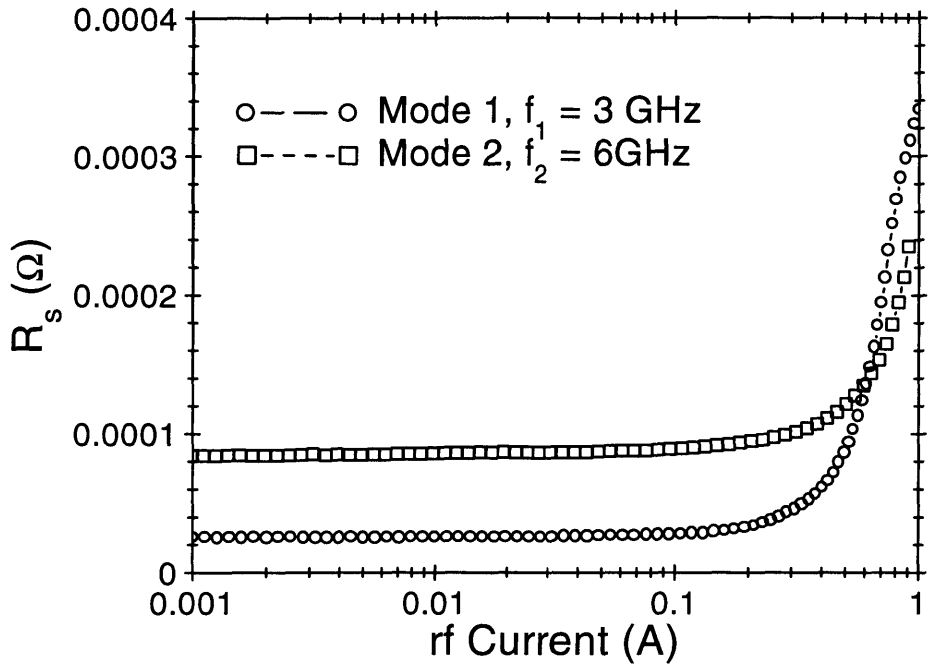

Figure 3-6: Measurement results of the surface resistance as a function of rf current, $R_s(I_{rf})$. The measurements were performed on a YBCO thin film using the stripline resonator technique. The results are shown for the first two resonant modes at T = 20 K, shown on a semi-log plot.

Now all the pieces are in place to examine the measured surface impedance as a function of rf current for the YBCO thin films used in this study.

3.2.2 Measurement Results of $Z_s(I_{rf})$

The surface resistance as a function of rf current $R_s(I_{rf})$ obtained using the stripline resonator measurement technique outlined in the previous sections is shown in Fig.3-6 for the first two resonant modes at T = 20 K. This data was measured on a YBCO on sapphire thin film prepared as described in Chapter 2 and is typical of many samples tested in this study. In the low-power regime, $I_{rf} < 0.1$ A, the magnitude of R_s is effectively constant as a function of rf current. Over this range of I_{rf}, the R_s is in the so-called linear regime, and the magnitude of R_s increases by approximately a factor of four between the fundamental resonant mode, $f_1 = 3$ GHZ, and the second mode, $f_2 = 6$ GHz, which is in agreement with the frequency squared dependence predicted by the two-fluid model in Eq.3.5. The low power value of R_s varied by no more than a factor of two from sample to sample at a given temperature. The low

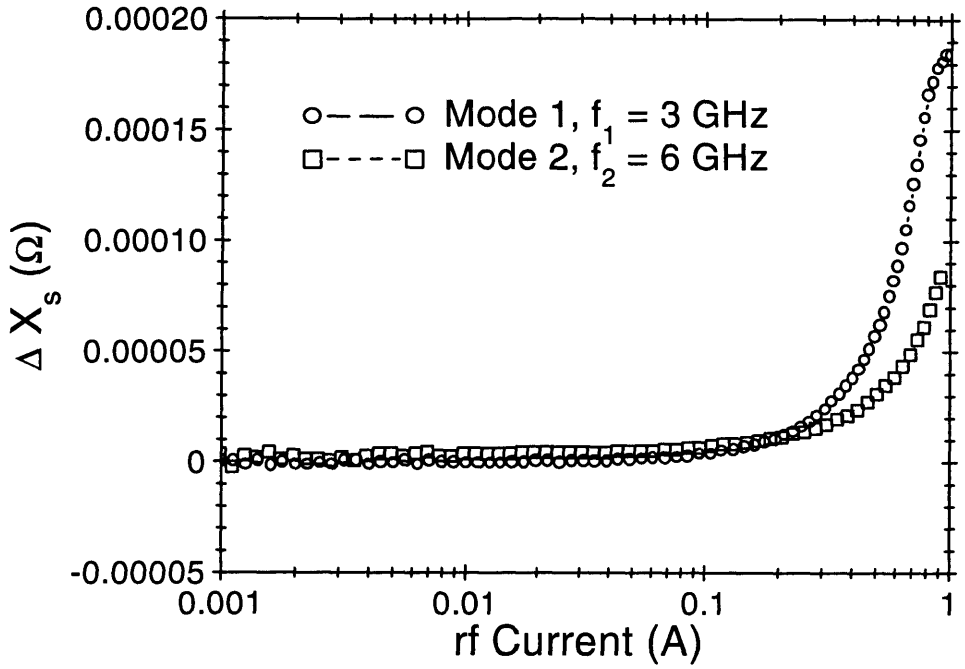

Figure 3-7: Measurement results showing the change in surface reactance vs. rf current, $\Delta X_s(I_{rf})$. The measurements were performed on a YBCO thin film using the stripline resonator technique. The results are shown for the first two resonant modes at T = 20 K, shown on a semi-log plot. This data is taken on the same device as in Fig.3-6

power R_s of 22 and 83 $\mu\Omega$ for 3 and 6 GHz respectively at 20K is a typical result for good quality films.[30, 31]. The low power value of R_s for both modes is however higher than theoretically predicted and this residual resistance has been attributed to defect structures resulting from thin film processing techniques.[23] As the rf current is increased into the range 0.1 to 1 A, the R_s enters the nonlinear regime, R_s is no longer independent of rf current, and the microwave frequency losses increase rapidly with I_{rf}. Results similar to those shown in Fig.3-6 have been measured in YBCO thin films by other researchers using similar measurement techniques.[23, 30, 32, 33, 34] Microwave power losses, harmonic generation, and intermodulation distortion occurring in this nonlinear regime limit possible device applications of high-T_c thin films. Possible explanations for the large residual value of R_s at low currents and the mechanism of nonlinear power handling will be presented in the next section.

In Fig.3-7 the change in surface reactance as a function of rf current, $\Delta X_s(I_{rf})$, as obtained from Eq.3.24 is presented for the first two resonant modes at T = 20

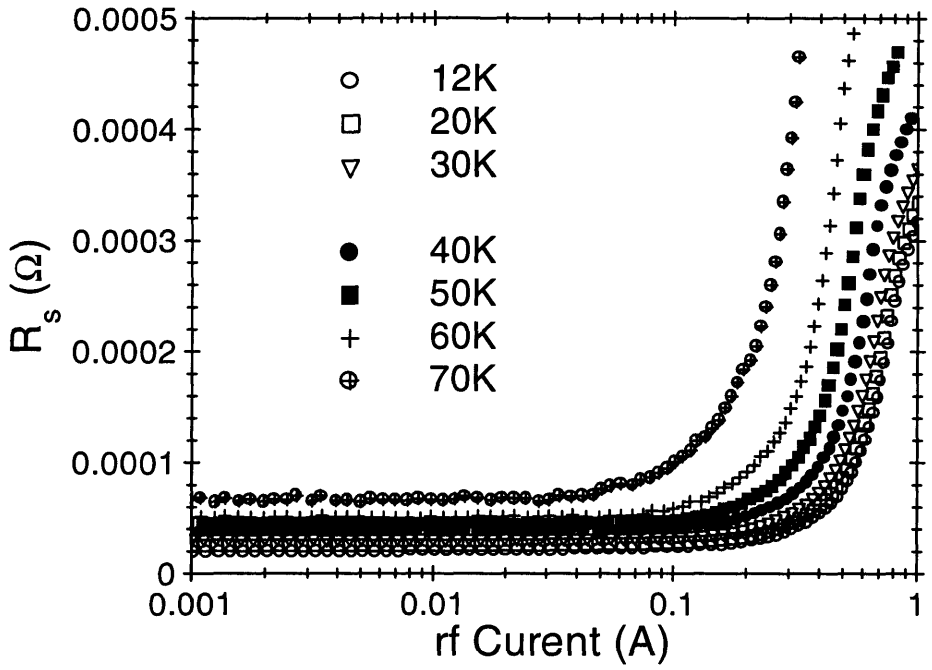

Figure 3-8: The results of measurements showing $R_s(I_{rf})$ at different temperatures for the fundamental f_1 resonant mode.

K. This data is taken on the same device as was used in Fig.3-6. The ΔX_s has the same general functional behavior as R_s in current; below 0.1 A the ΔX_s is effectively constant and zero, while for $I_{rf} > 0.1$ A the change in surface reactance begins to increase and then increases sharply for $I_{rf} > 0.2$ A. Simlar to the dependence of $R_s(I_{rf})$, in the range 0.1 to 1 A, the ΔX_s enters the nonlinear regime where ΔX_s is no longer independent of rf current.

Finally, in Fig.3-8 $R_s(I_{rf})$ is presented for a range of temperatures. The overall character of the $R_s(I_{rf})$ does not change much with temperature, but the value of the residual, low-current R_s increases while the rf current level where nonlinear power losses begin, decreases with increasing temperature. The plots shown in Figs.3-6, 3-7, and 3-8 demonstrate that improvements could be made in both reduction of the low power residual surface resistance and increases in the rf current level where the onset of nonlinear power losses begins. Some proposed mechanisms for both the residual R_s and the nonlinear power response of R_s to increasing rf power are presented in the next section.

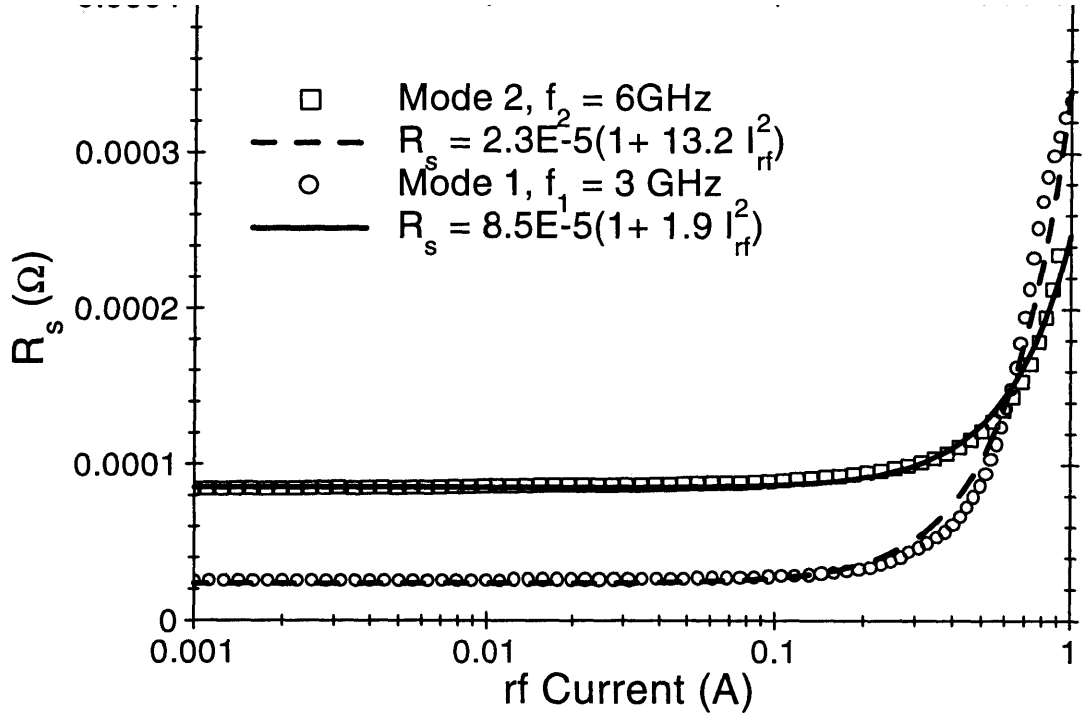

Figure 3-9: Surface resistance vs. rf current $R_s(I_{rf})$ plots from Fig.3-6, with quadratic fits obtained from Eq.3.25.

3.2.3 Possible Physical Mechanisms for the Measured $Z_s(I_{rf})$ in YBCO Thin Films

The magnitude of R_s of YBCO thin films in the limits of very low power and temperature has a significant residual value which is in disagreement with the BCS theory. The observed granular, or polycrystalline, morphology of the films has led to a coupled-grain model to describe R_s in the low power limit.[23, 35, 36] The coupled grain model treats the thin film as a network of ideal superconducting grains separated by grain-boundary weak links. The grains are assumed to have intrinsic properties which can be described by BCS or Ginzburg-Landau theories, while the grain boundaries act as Josephson junctions. In this model, the low power R_s is dominated by the extrinsic resistivity of the grain boundaries which are in series with the lower resistance grains. Presumably, if films without grains could be produced, the low power R_s could be reduced.

The coupled-grain model has also been extended to account for the onset of non-linearities in Z_s.[23, 37, 38, 39, 40, 41] The grain boundary Josephson junctions in the model are characterized by a critical current I_c and normal resistance R_n. When

I_{rf} exceeds I_c, nonlinearities will occur due to the creation of Josephson fluxons.[42] The power dependent coupled-grain model predicts a quadratic dependence of R_s on I_{rf}[37, 23],

$$R_s = R_s(0)[1 + b_r I_{rf}^2] \tag{3.25}$$

where $R_s(0)$ is the limiting low power value of R_s and b_r is the quadratic coefficient. The $R_s(I_{rf})$ plots from Fig. 3-6 are shown with fits to the data obtained using Eq.3.25 in Fig. 3-9, to demonstrate that the quadratic dependence of R_s on I_{rf} is in agreement with experimental data. It has also been proposed that the onset of nonlinearities is due to edge effects in the patterned transmission line. Since the current density is large at the edges of the line, imperfections at the edges due to patterning techniques could effect the power handling. However, this seems unlikely since the nonlinear behavior also has been observed in unpatterned films.[43] Abrikosov vortices will be created in the film when I_rf reaches a level sufficient that the magnetic field at the surface of the film is equal to H_{c1} which will result in nonlinearities. However, the nonlinear behavior begins at lower rf current levels than are required to exceed H_{c1}.[42] Localized heating at defects in the film could also cause an onset of nonlinear impedance behavior.[44] Heating is known to occur at defects as the resistance begins to increase rapidly and this heating effect can damage the films irreversibly.[45]

Josephson junction effects at grain boundary weak links are widely believed to be responsible for both the linear and nonlinear regimes of the microwave Z_s. Thus motivated, I present in the next chapter the results of measurements and modeling of the microwave impedance in high-T_c Josephson junctions.

Chapter 4

Josephson Junctions

The observed power dependence of the microwave-frequency surface impedance in YBCO thin films has been attributed to Josephson junction (JJ) effects that are a consequence of the defect structures found in the films. The morphology and distribution of microstructural defects varies from film to film, with the composition of the defect structures being strongly influenced by the film deposition parameters.[46, 47] However, the films are generally observed to have a granular structure which has led to the development of a coupled-grain model to explain the measured surface impedance as a function of rf current.[35, 36] This model has yielded good agreement with experimental results in both the low power (linear) and high power (nonlinear) regimes.[23, 48] In this coupled-grain model, the superconducting film is modeled by many ideal superconducting grains that are separated by grain-boundary weak links, thus forming a random network of coupled Josephson junctions (JJs) with a distribution of properties. A systematic study of the microwave power-handling capabilities of engineered high-T_c JJs is useful for interpreting the observed rf power dependence of thin films within the context of a coupled-grain model. Quantifying the microwave power losses occurring in high-T_c JJs and identifying the microstructural film defects that result in rf junction effects could help lead to the production of films with improved power-handling capabilities.

In this chapter, I present a study of the measured and modeled microwave impedance of high-T_c Josephson junctions as a function of microwave current to investigate the

idea that JJ defects are responsible for the observed power handling in thin films. Studying power-dependent JJ effects at microwave frequencies also provides a means to explore some fundamental physics that has not previously been examined extensively and has practical importance for device applications. This chapter begins with some background on Josephson junctions and the types of JJs used in this study. The experimental technique employed to directly measure rf JJ effects, and the results of power-dependent impedance measurements performed on high-T_c JJs at microwave frequencies are presented. Then, a long-junction model is introduced, and the model calculations are compared with the measured data. Finally, modeling and measurement results are used to understand the mechanisms responsible for rf power losses in JJs and to quantify the effects of Josephson vortex creation, annihilation, and motion on rf power handling. Analysis of the measured and modeled data specifically shows that Josephson vortices created by rf currents cause the nonlinearities in the impedance.

4.1 Measurements of Josephson Junctions

4.1.1 Engineering YBCO Josephson Junctions

A Josephson junction is a system of two superconducting electrodes separated by a thin interlayer material through which Cooper pairs can interact quantum mechanically. The interlayer material can be an insulator (SIS junction), a normal metal (SNS junction), or some other constriction or defect generally referred to as a "weak link" that causes a suppression of the macroscopic superconducting order parameter Ψ. In 1962, Brian Josephson correctly predicted that a zero-voltage supercurrent would flow from one superconducting electrode to the other through the interlayer material. The Josephson current is governed by the expression,

$$I_j = I_c \sin \phi \tag{4.1}$$

where I_j is the current through the junction, I_c is the critical current which is the maximum zero-voltage current that can flow through the junction, and ϕ is the gauge-

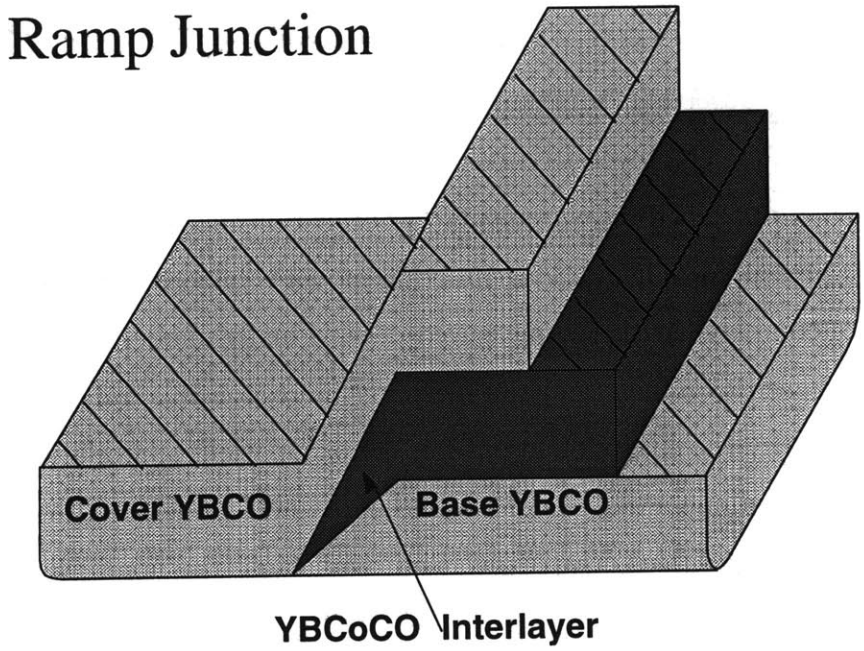

Figure 4-1: Ramp-type Josephson junction schematic. Two YBCO electrodes with a wedge shaped interlayer of cobalt-doped YBCO ($YBa_2CoCu_3O_{7-\delta}$) form an SNS type junction.

invariant phase difference of the superconducting wavefunctions on either side of the interlayer. In addition, Josephson found that a voltage across the junction will cause ϕ to evolve in time,

$$\frac{d\phi}{dt} = \frac{2\pi V_j}{\Phi_0} \tag{4.2}$$

where V_j is the voltage across the junction and $\Phi_0 = \pi\hbar/e = 2.068 \times 10^{-15}$ Wb is the magnetic flux quantum or fluxon. The Josephson current-phase (Eq. 4.1) and voltage-phase (Eq. 4.2) equations are now considered to be fundamental to superconductivity in general, and the Josephson effect has resulted in many important device applications.[19, 21, 49, 50]

Two types of Josephson junctions were studied for this thesis work. The initial studies were done on SNS ramp-type junctions shown schematically in Fig. 4-1. The ramp-type of configuration was fabricated by depositing a base electrode of YBCO on a $LaAlO_3$ substrate (not shown) which is partially masked by an angled stainless steel blade resulting in the desired ramp shape shown in Fig. 4-1. Then the normal-metal interlayer of cobalt-doped YBCO, $YBa_2CoCu_3O_7$, is deposited in a wedge shape before a cover electrode of YBCO is finally deposited over the whole assembly resulting in a Josephson junction. These junctions were engineered by Koren *et al.* using pulsed-laser deposition.[51] The layered films were grown to a thickness of 2000 Å each. The measurements I performed on ramp-type junctions were done early in my doctoral research work, before I started studying grain-boundary type junctions, which are more relevant to the motivation associated with the coupled-grain model.

The method used to engineer a grain-boundary JJ is shown schematically in Fig. 4-2. A grain-boundary JJ more closely simulates the type of weak links found in YBCO thin films than the ramp junction shown in Fig. 4-1. To form the grain boundary, YBCO is deposited on a commercially-obtained sapphire bicrystal substrate using the pulsed laser technique described in Chap. 2. The bicrystal is manufactured by fusing together two sapphire single crystals oriented with a common c-axis but with a rotation of the a-axis in the basal a-b plane, similar to the grain alignment found in c-axis oriented YBCO films. The substrate is cut so that the border between the two crystals is directly across the centerline of the substrate dividing it into two equal halves as shown in Fig. 4-2. The a-axis rotation is symmetric about the centerline, and the degree of a-axis rotation can be characterized by a misorientation angle θ which is 24° in the case of Fig. 4-2. The YBCO is deposited on the bicrystal epitaxially, so that the crystalline orientation of the YBCO mimics that of the bicrystal substrate, resulting in an engineered grain boundary of YBCO with a misorientation angle of $\theta = 24°$. The electronic properties of grain boundaries are very sensitive to the degree of the misorientation angle[52, 53], and this angular dependence will be examined in the next chapter. As with the films grown on single-crystal substrates presented in Chap. 2, dc measurements were performed on the 24° grain-boundary junctions

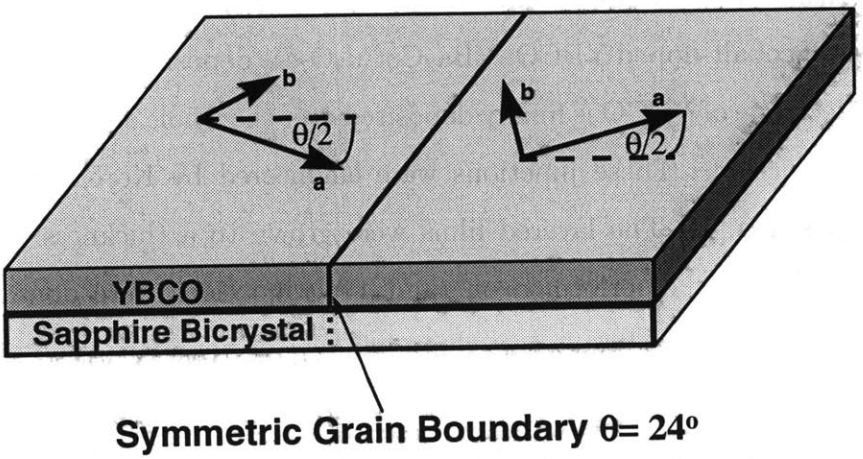

Figure 4-2: Bicrystal grain-boundary Josephson junction schematic. A YBCO thin film is deposited epitaxially on a commercially-obtained sapphire bicrystal substrate with a 24° misorientation angle resulting in an engineered grain-boundary. The degree of misorientation is symmetric about the boundary.

on four-point test structures. These structures are removed by etching prior to the performance of the rf measurements.

4.1.2 dc Measurements

To obtain the critical current I_c and the normal-channel resistance R_n of the 24° grain-boundary JJ as a function of temperature, I performed four-point I-V measurements at temperatures from 5 to 80 K. The temperature dependence of I_c is shown in Fig. 4-

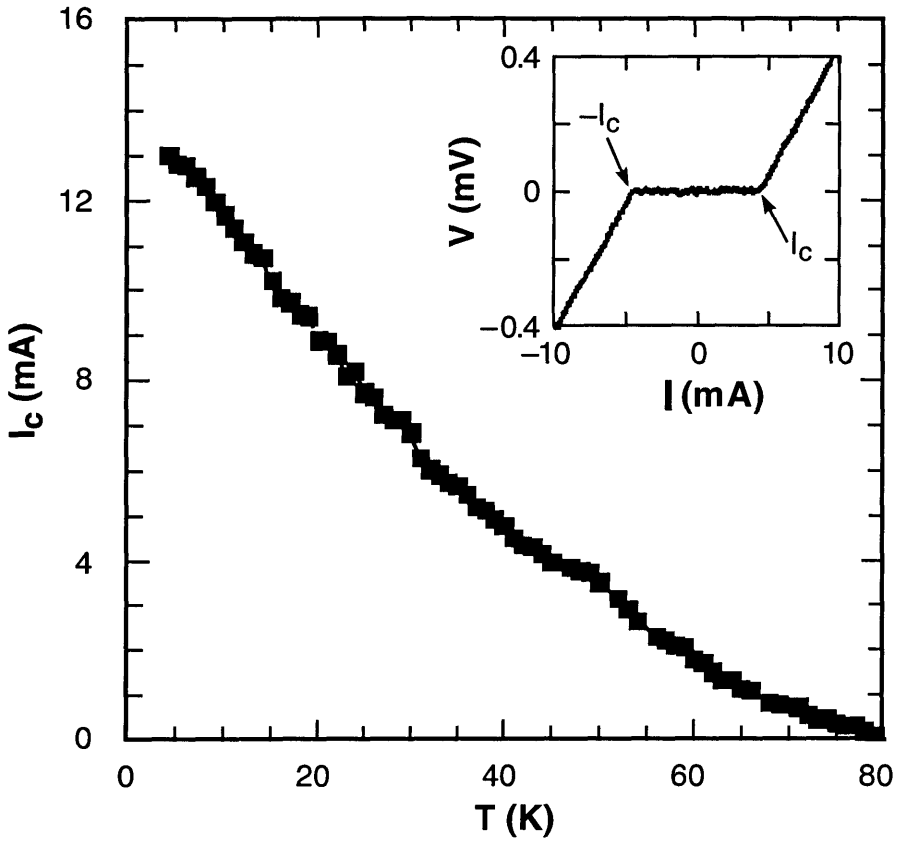

Figure 4-3: Measurement results for a 24° grain-boundary JJ showing the temperature dependence of the dc critical current I_c. The I_c and R_n at each temperature were determined from I-V measurements. The inset is a typical I-V curve measured at 40 K. All the observed temperature dependence was for I_c, with R_n remaining constant with a value $R_n \approx$ 80 m$\Omega \pm$ 10 mΩ, independent of temperature.

3, with a typical I-V curve ($T = 40$ K) shown in the inset, from which the I_c and R_n data were extracted. The I-V curves, such as the one shown in the inset in Fig. 4-3, were taken at each temperature. As the dc current is increased from zero, the voltage

across the JJ remains zero until the current level reaches I_c and the JJ switches to a resistive state. The I_c value is determined by the 20 μV criterion given in Sec. 2.3 and is marked on the inset to Fig. 4-3. The value of R_n is determined by the slope of the I-V curve ($R_n = dV/dI$) at current levels above I_c, and the value of R_n does not vary with increasing current. The value of R_n remained constant over the entire temperature range $R_n = 80 \pm 10\,\mathrm{m}\Omega$. It is interesting to compare the I-V curve in Fig. 2-4 with that in Fig. 4-3. Both YBCO films were deposited from a common target during the same laser deposition run, yet the film grown on a single-crystal sapphire substrate has a critical current about three orders of magnitude greater than the grain boundary grown on a bicrystal substrate. In addition, the characteristics of the I-V curves in the vicinity of I_c are markedly different. The grain boundary I-V plot in Fig. 4-3 shows a distinct kink at I_c where a voltage develops and the curve breaks to a constant sloped resistive state. The I-V curve in Fig. 4-3 also shows no hysteresis and is characteristic of an overdamped resistively-shunted junction.[50, 54] In contrast, the way the I-V curve in Fig. 2-4 turns radially upward when I_c is reached is characteristic of flux-flow which results in significant heating. It is also noteworthy that the 24° grain-boundary junctions show a large excess current, $I_{\mathrm{ex}} = I - V/R_n \approx I_c$, which has also been reported by other researchers in similar systems.[55, 56] The measured critical current is very sensitive to magnetic fields and hence magnetic shielding was used to ensure an ambient field $B < 10^{-7}$ T in the sample-measurement space for all measurements reported here.

4.1.3 Microwave Measurements of Josephson Junctions

The microwave power dependence of the engineered Josephson junctions described in the previous section can be directly measured using the stripline-resonator technique presented in Chapter 3. By exploiting the properties of the standing waves in the transmission line, the rf current dependence of the JJ can be distinguished from the rest of the film. To this end, the resonator line is patterned such that the JJ is positioned at the midpoint of the stripline length ($l \approx 2$ cm) and spanning the entire width, as shown in the upper part of Fig. 4-4. At resonance, the fundamental $n = 1$

mode is a half-wavelength standing wave with a current maximum at the midpoint of the resonator line, where the fabricated JJ is positioned. In contrast, the $n = 2$ resonant mode is a full-wavelength standing wave with a current node at the position of the JJ. Thus, the $n = 1$ mode will be maximally affected by the JJ, while the $n = 2$ mode will be minimally affected. The current distributions along the length of the stripline for the first two modes are shown in the lower part of Fig. 4-4. Comparing the measured results on these two resonant modes is the method employed to separate the rf properties of the engineered JJ from those of the remainder of the superconducting film constituting the majority of the resonator structure.

The current distribution across the width of the line and through the thickness of the film is an important experimental consideration. The width w of the patterned stripline $w = 150\,\mu$m is large compared with the London penetration depth, $\lambda_l \approx 0.2\,\mu$m (at $T \leq 70$ K), while the thickness t of the films, $t = 0.14$ and $0.2\,\mu$m for the grain-boundary and ramp junctions respectively, are about equal to λ_l, so that $w \gg \lambda_l \approx t$. Thus, the current density is essentially uniform through the thickness of the film, but very nonuniform across the width of the stripline. The normalized current density $J_{rf}(x)/J_{AVG}$ as a function of position x across the stripline width is shown in Fig. 4-5, which was calculated using the method of Sheen *et. al.*[28] The current is peaked at the edges of the line with an edge value approximately ten times greater than at the center of the line.

The JJ is considered a small perturbation to the overall current distribution in the stripline structure, since the Q remains over 10^3, even at high rf current levels. Thus, the resonator line acts as a current source for the junction, so that the current profile into and out of the JJ is that shown in Fig. 4-5. The JJ is expected to have essentially no effect on the measured properties of the resonator in the low-power limit, when the current density at the stripline edges is much less than the JJ critical-current density J_c. As the input power is increased, a critical level is reached when the rf current density in the stripline first begins to exceed the J_c of the JJ at the edges of the line. When this critical level is exceeded, JJ effects are expected to be observed in the $n = 1$ mode, but no such JJ effects should affect the $n = 2$ mode.

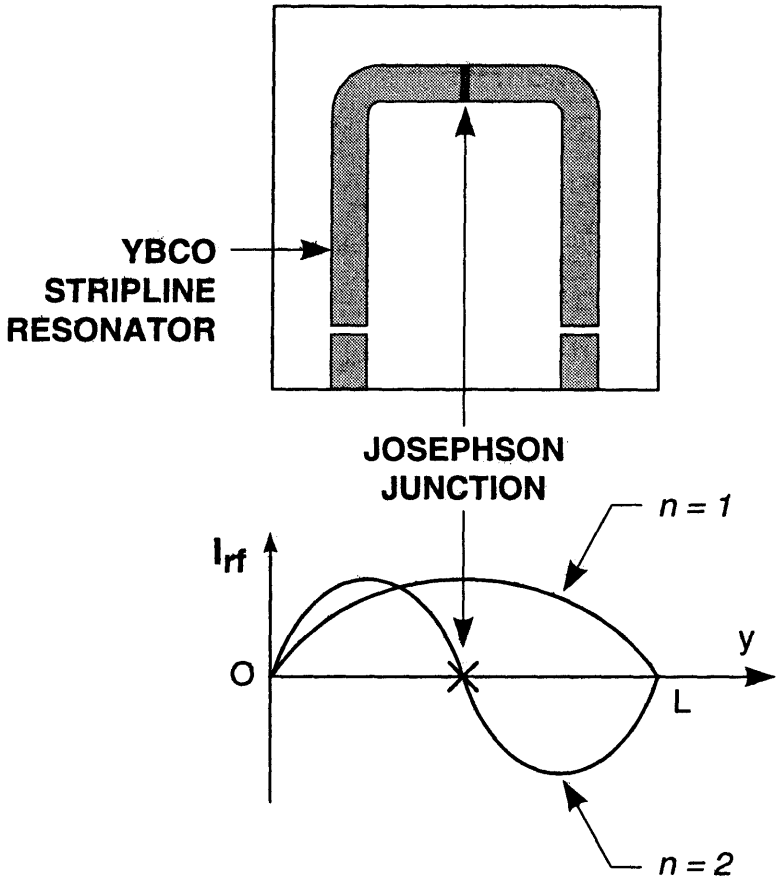

Figure 4-4: The upper figure shows the pattern of the YBCO stripline resonators used in this JJ study. The schematic includes the capacitive coupling strips at the resonator ends. The Josephson junction is positioned at the midpoint of the striplines length. The lower figure shows the rf current distribution $I_{rf}(x)$ along the length of the stripline for the standing waves of the first two resonant modes. The first ($n = 1$) mode has a current peak at the junction, while the second ($n = 2$) mode has a current node at the position of the JJ.

Microwave measurements were performed on the first two modes as a function of input power and temperature. The measurement technique that was employed, and the experimental equipment setup are the same as described in Chap. 3. Figure 4-6 shows the results of rf measurements on the 24° grain-boundary JJ, comparing the

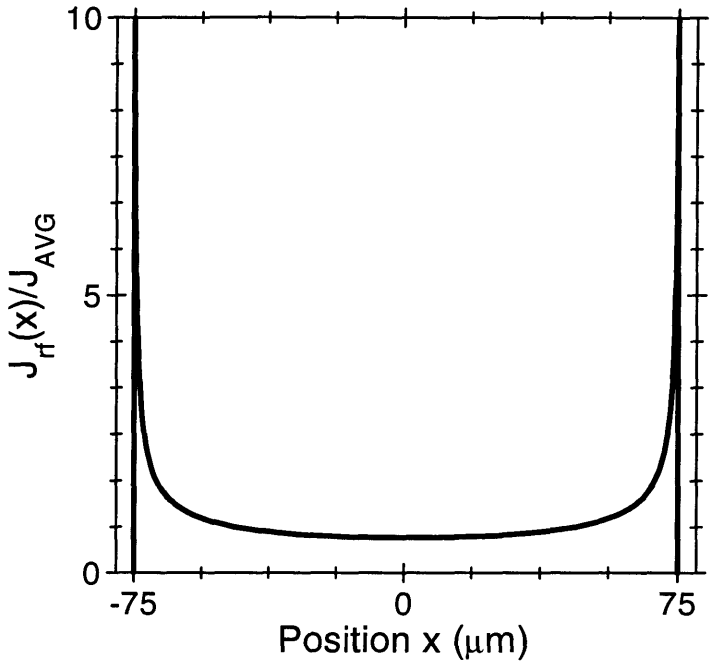

Figure 4-5: The current density distribution across the stripline-resonator center conductor showing the normalized current density $J_{rf}(x)/J_{\mathrm{AVG}}$ as a function of position x across the width ($w = 150\,\mu$m) of the stripline. The current density is peaked at the edges of the line and is approximately ten times greater at the edge than at the center. The current density is uniform through the thickness of the film.

normalized frequency shift $\Delta f_n/f_n$ (proportional to the reactance) and the inverse quality factor $1/Q$ (proportional to the resistance) as a function of rf current at $T = 50$ K for the $n = 1$ and $n = 2$ modes. At low levels of rf current, 0.1 mA $< I_{rf} <$ 1 mA, before the onset of the JJ effects, the values of $\Delta f_n/f_n$ and $1/Q$ are independent of I_{rf} with $\Delta f_n/f_n \approx 0$ for both modes, and the $1/Q \approx 0.1$ and $1/Q \approx 0.05$ for the $n = 1$ 1 and $n = 2$ modes respectively. The factor of 2 separating the value of $1/Q$ for the $n = 1$ and $n = 2$ modes corresponds to an f^2 (factor of 4) difference in the value of R_s given by Eq. 3.10 for the $n = 1$ and $n = 2$ modes. This low-power f^2 dependence is predicted by the two-fluid model and is typically observed in films without engineered JJs, as shown in Fig. 3-6. At $I_{rf} \approx 1$ mA, both the $\Delta f_n/f_n$ and $1/Q$ data rise sharply for the $n = 1$ mode. In contrast, for the $n = 2$ mode, the data still remain constant for almost two more orders of magnitude of increase in the rf current level. The significant rise in the $\Delta f_n/f_n$ and $1/Q$ data

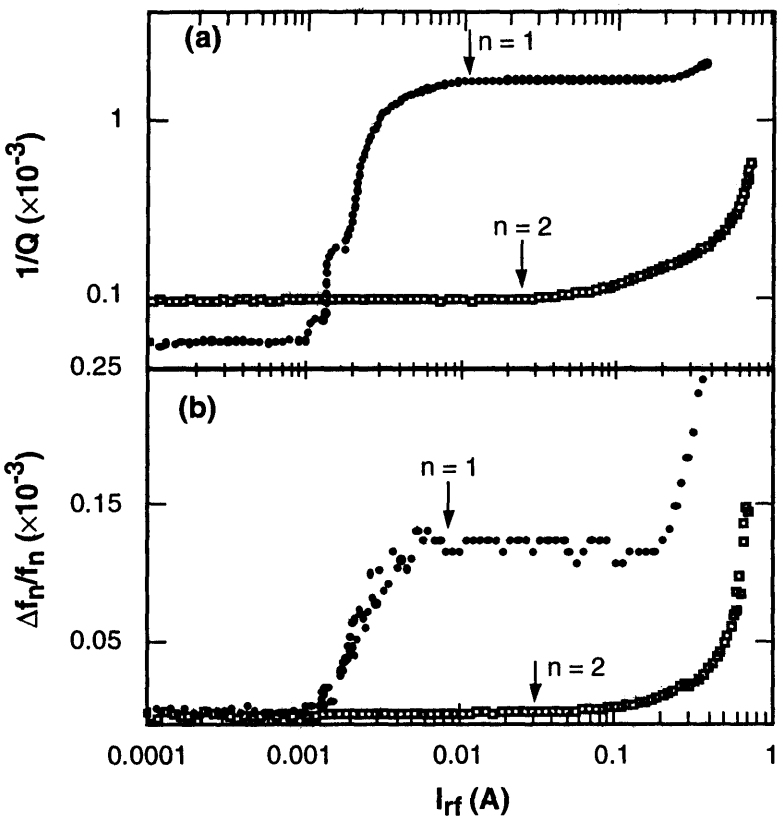

The measured $1/Q$ (a) and $\Delta f_n/f_n$ (b) data for a 24° grain boundary JJ as a function of rf current for the first two [$n = 1$ (filled circles) and $n = 2$ (open squares)] resonant modes at 50 K. Notice that both $1/Q$ and $\Delta f_n/f_n$ rise sharply at $I_{\rm rf} \approx 1$ mA for the $n = 1$ resonant mode, while both $1/Q$ and $\Delta f_n/f_n$ for the $n = 2$ mode remain almost

Figure 4-6: constant for nearly two more orders of magnitude of increase in I_{rf}. In the range 1 mA $< I_{\rm rf} <$ 200 mA, the $n = 1$ mode data are dominated by the effect of the JJ. The data for the $n = 2$ mode is similar to that seen in resonators without fabricated JJs. Also notice the step-like structures in the $1/Q$ data for the $n = 1$, mode which result from flux quantization in Josephson vortices nucleated by rf currents.

for the $n = 1$ mode at rf current levels where the $n = 2$ mode remains constant is due to the junction J_c being exceeded by the rf current. The distribution of J_{rf} into the JJ is peaked at the edges as shown in Fig. 4-5, thus as J_{rf} is increased, J_c will first be exceeded at the edges of the JJ. As the current is increased to $I_{rf} \approx 8$ mA, the $n = 1$ mode $\Delta f_n/f_n$ and $1/Q$ data saturate and become constant in current. The saturation level is shown below to be determined by R_n, and from the $1/Q$ data the effective JJ resistance is found to saturate at a value equal to the R_n value from dc measurements. Once saturation is reached the JJ is in the normal state for most of the rf cycle and JJ effects can no longer change the values of $\Delta f_n/f_n$ and $1/Q$. The saturation effect persists until the high-current limit of $I_{rf} \geq 200$ mA where the $n = 1$ mode $\Delta f_n/f_n$ and $1/Q$ data begin increasing again. This high-current limit increase occurs because the rf power losses in the superconducting film separate from the JJ have increased enough to dominate the measured data. The $n = 2$ mode data begin increasing at $I_{\rm rf} \approx 100$ mA and turn up sharply at $I_{\rm rf} \approx 400$ mA and this is attributed to the same loss mechanisms in the superconducting film that cause the $n = 1$ mode to increase in the high-current limit. The increases in $\Delta f_n/f_n$ and $1/Q$ with rf current occur at the same values of $I_{\rm rf}$ for each mode, respectively. The rf measurements performed on films grown on single crystal substrates shown in Figs. 3-6, 3-7, and 3-8 show a current dependence similar to the $n = 2$ mode data shown here, but markedly different from the $n = 1$ data. Interesting step structures begin to develop in Fig. 4-6 in the $n = 1$ mode $1/Q$ data at $I_{\rm rf} \approx 1$ mA, while the steps are not seen for the $n = 2$ mode or in films without engineered junctions. As shown below, the measured sharp rise in $1/Q$ and $\Delta f_n/f_n$ for the $n = 1$ mode is due to the nucleation of Josephson vortices in the grain-boundary JJ by the microwave input current.

Measurement of $1/Q$ as a function of I_{rf} performed on a ramp-type junction at $T = 40$ K is presented in Fig. 4-7, showing a comparison of the $n = 1$ and $n = 2$ resonant modes. As with Fig. 4-6, there are noticeable increases of $1/Q$ in the $n = 1$ mode data at rf current levels where the $n = 2$ mode data remain relatively constant. However, the complete saturation effect seen in the $n = 1$ mode data of Fig. 4-6 for

the grain-boundary JJ is not observed for the ramp JJ in Fig. 4-7. Measurements of the dc I-V curves on the ramp junction showed that $I_c = 43$ mA at 40 K and that $R_n \approx 10$ mΩ, independent of temperature. The dc I_c of the ramp junction is about an order on magnitude greater than for the grain-boundary junction at $T = 40$ K, while the R_n is about an order on magnitude smaller for the ramp type than the grain boundary JJ. However, comparison of Figs.4-7 and 4-6 show a very similar dependence of $1/Q$ on rf current for the $n = 2$ modes in both junction types, indicating that the YBCO film in both devices is of similar quality. Therefore, the saturation behavior observed in Fig. 4-6 for the grain-boundary junction is masked in Fig. 4-7 by film effects due to the relatively higher I_c and lower R_n values in the ramp-type junction. Interestingly, for both junction types step structures are observed in the $1/Q$ data at the rf current level where $1/Q$ begins to increase due to the JJ. Having established that the stripline-resonator technique provides a means to directly measure the rf power dependence of $1/Q$ and $\Delta f_n/f_n$ in the JJ, the next step is to relate these quantities to the junction resistance R_j and reactance X_j.

The rf-current dependence of the JJ resistance $R_j(I_{rf})$ is obtained from the unloaded Q as given by Eq. 3.7. As explained in Chap. 3, the Q_u is related to the ratio of the power dissipated in the resonator to the average energy stored in it,

$$\frac{1}{Q_u} = \frac{1}{\omega}\frac{\text{Power Dissipated}}{\text{Energy Stored}}, \tag{4.3}$$

with ω being the resonant angular frequency of the rf signal. The resonator resistance is proportional to the power dissipated by the rf current, and hence $1/Q_u$. To obtain the effective JJ resistance from the $1/Q_u$ data, the JJ is modeled by a very thin piece of material of uniform resistivity ρ_n placed at the center of the superconducting stripline across the entire width. The power dissipated per unit volume by the rf current density J_{rf} is $(1/2)\rho J_{rf}^2$ for both the resistive and superconducting parts of the line. The analysis of the resistivity of the superconducting line ρ_s is unchanged from Chap. 3 and is obtained from the complex conductivity in Eq. 3.8. The stored energy per unit volume is given by $(1/2)\mu_0 H_{\rm rf}^2$, where $H_{\rm rf}$ is the rf magnetic field generated by the rf current density in the resonator. The power dissipated and the

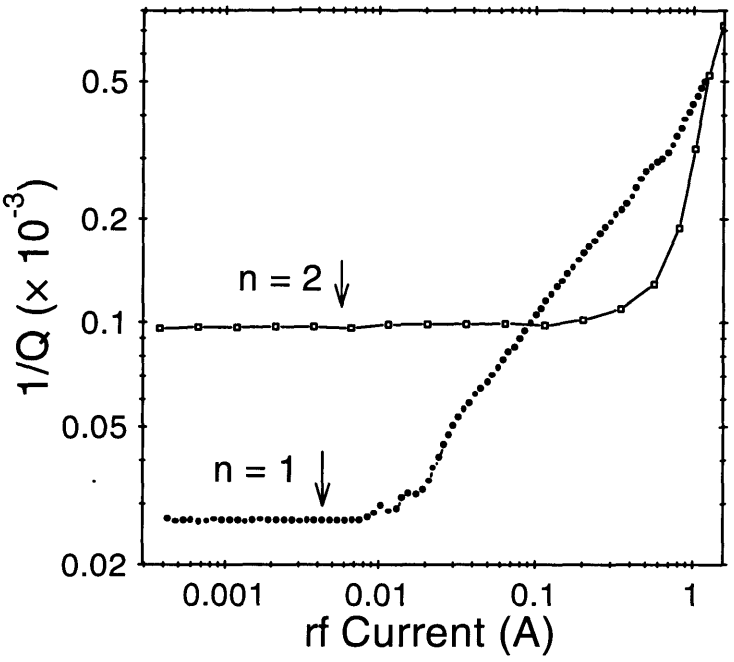

Figure 4-7: The $1/Q$ as a function of rf current measured on a ramp type junction engineered into a stripline resonator for the first two [$n = 1$ (filled circles) and $n = 2$ (open squares)] resonant modes at T = 40 K.

energy stored per unit volume are integrated over the length l of the stripline. Then, Eq. 3.9 can be modified to include the effects of the JJ on Q_u such that,[57, 58]

$$\frac{1}{Q_u} = \left[2R_s\lambda_l + \frac{2wtR_j}{L}\right] \frac{\int J_{rf}^2 dA}{\omega \int \mu_0 H_{\rm rf}^2 dA}. \tag{4.4}$$

The first term in the brackets is proportional to the power dissipated in the superconducting line and is identical to Eq. 3.9, while the second term is proportional to the power dissipated in the JJ for which the effective JJ resistance is $R_j = \rho_n d/wt$ where d is the thickness of the resistive material. The ratio of the area integrals in Eq. (4.4) is the same constant geometrical factor as in Eq. 3.9, which was calculated by the method of Sheen *et al.*[28]

As shown in Fig. 4-6, the measured $1/Q$ data for the $n = 1$ mode increases by over an order of magnitude in the rf current range 1 mA $< I_{rf} <$ 4 mA, while the $1/Q$ data for the $n = 2$ mode remains constant. The $1/Q$ for the $n = 1$ mode reaches

a saturation level for currents in the range 4 mA $< I_rf <$ 200 mA. Both the sharp rise and the saturation of $1/Q$ are due to the grain-boundary junction. When $I_{rf} <$ 1 mA, the measured value of $1/Q_u$ is completely related to the surface resistance of the YBCO film, but in the current range of 1 mA $< I_{rf} <$ 200 mA, the $1/Q_u$ data is dominated by JJ effects. Thus, while the JJ and the YBCO film both contribute to the measured value of $1/Q_u$, over the current range 1 mA $< I_{rf} <$ 200 mA the R_j term in Eq. (4.4) determines $1/Q_u$ as Fig. 4-6 shows. By properly normalizing the $1/Q(I_{rf})$ data on the entire JJ resonator structure with the coefficients of the R_j term in Eq. 4.4, the measured effective total JJ resistance $R_j(I_{rf})$ is obtained,

$$R_j(I_{rf}) = \frac{1}{Q_u(I_{rf})} \frac{L}{2wt} \frac{\omega \int \mu_0 H_{rf}^2 dA}{\int J_{rf}^2 dA} = \frac{\Upsilon f_1}{Q_u(I_{\mathrm{rf}})} \tag{4.5}$$

with f_1 being the resonant frequency of the $n = 1$ mode in GHz and $\Upsilon = 16.7\ \Omega$/GHz. This analysis applies to the stripline geometry shown in Fig. 4-4 and is correct for rf current levels large enough to exceed the junction J_c. However, below this current level, the term calculated by Eq. 4.5 is approximately 75 times the R_s of the YBCO film. Strictly speaking, the low current term proportional to R_s would be subtracted out to plot only $R_j(I_{rf})$. However, since it is small compared to R_j, and as seen below, the relevant data plots would be difficult to observe without a measurable R_s value.

The $R_j(I_{rf})$ as obtained from Eq. 4.5 for a range of temperatures is presented in Fig. 4-8 for a 24° grain-boundary JJ. In the low-current limit, where R_j is approximately constant as a function of rf current, the magnitude of R_j is proportional to the surface resistance of the superconducting film comprising the bulk of the resonator structure which is temperature dependent as shown. As the current is increased, Fig. 4-8 shows the existence of a critical rf current value where the resistance begins to increase precipitously. The rf current level where the sharp rise in R_j begins coincides with the onset of losses in the JJ when J_c is exceeded by J_{rf}. The JJ losses begin at lower rf current values with increasing temperature, similar to the measured dc value of I_c in Fig. 4-3. Step structures are apparent in the $R_j(I_{rf})$ curves above this critical rf current value. The steps are most pronounced at intermediate tem-

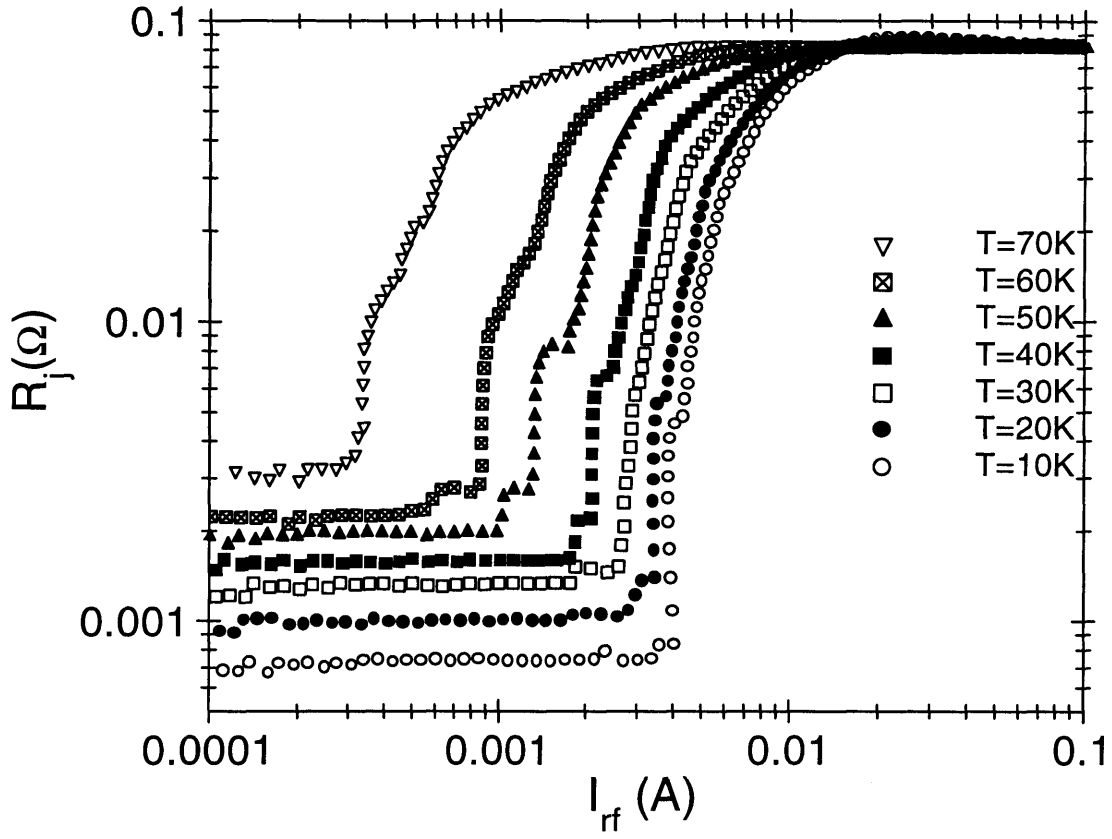

Figure 4-8: The measured effective resistance of a 24° grain-boundary JJ as a function of rf current $R_j(I_{rf})$ presented on a log-log plot for a range of temperatures. In the low-current limit, the value of $R_j(I_{rf})$ is independent of current and is proportional to the surface resistance of the film, rather than that of the junction. As the rf current is increased, there is a very sharp rise in the resistance curves, and step structures associated with fluxon quantization are observed. Also note that all curves saturate at the same $R_j^{\rm sat}$ value which is about the same as the R_n obtained from the dc measurements. As T is increased, the sharp rise in R_j occurs at lower values of I_{rf}.

peratures. As explained in detail in the next section, these steps result from the quantization of magnetic flux in the junction, and the sharp increases in resistance are due to Josephson vortices being created and annihilated by the rf current.[59] As the current is further increased beyond the region of the steps, R_j becomes independent of the rf current with all the curves saturating at essentially the same value of R_j independent of temperature; $R_j^{\rm sat} = 83\,m\Omega \pm 3m\Omega$, which agrees very well with

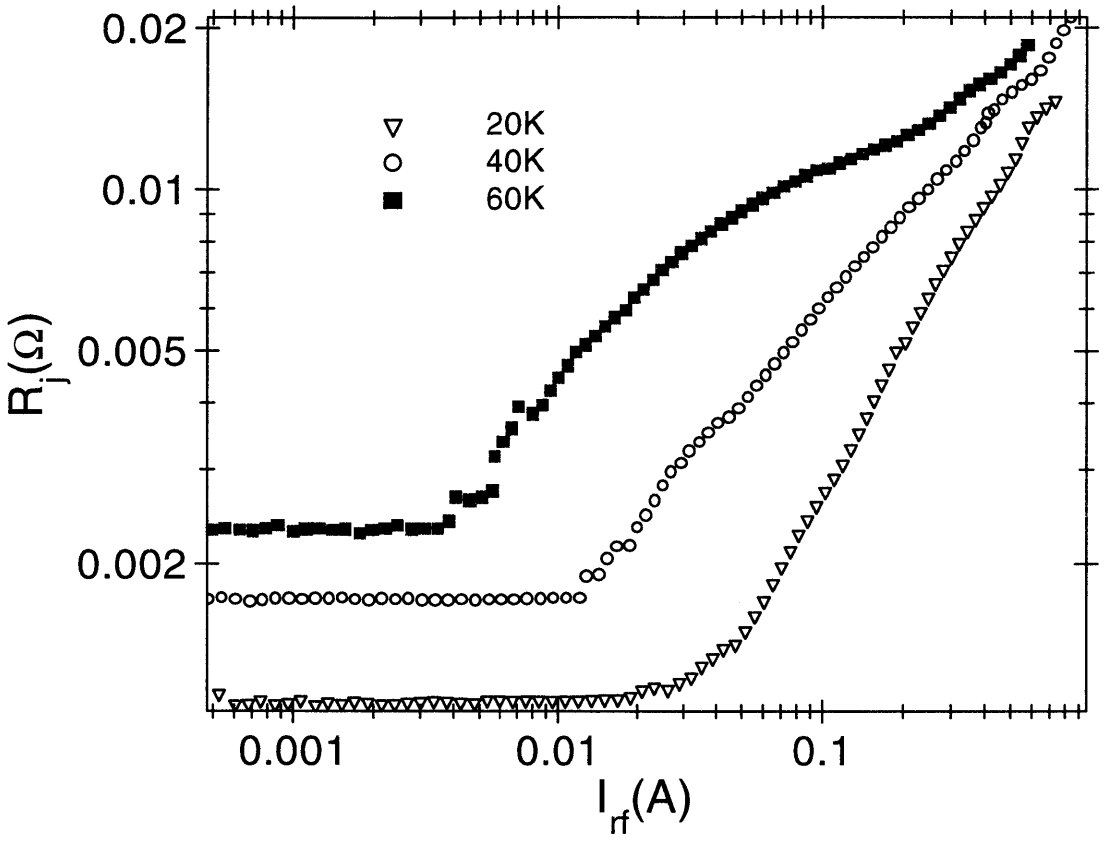

Figure 4-9: Measurements of $R_j(I_{rf})$ performed on a ramp-type junction for three different temperatures. As with Fig. 4-8, the $R_j(I_{rf})$ is independent of I_{rf} until a well-delineated current level is reached, where $R_j(I_{rf})$ increases sharply, showing some step-like structures. The complete saturation at $R_j = R_n$, seen in Fig. 4-8 is not observed for the ramp-type junction, due to its relatively higher I_c and lower R_n than the grain-boundary junction. The $T = 60$ K plot begins to roll over at 0.1 A but never fully saturates.

the measured dc value of $R_n = 80\,m\Omega \pm 10m\Omega$ presented in the previous section.

Figure 4-9 shows the measurement of $R_j(I_{rf})$ taken on a ramp-type junction at three different temperatures. The data clearly show the effects of the JJ on rf power handling. As seen in Fig. 4-8 the $R_j(I_{rf})$ is independent of I_{rf} until a critical rf current level is reached, where $R_j(I_{rf})$ increases sharply, with step-like structures evident. The saturation at $R_j = R_n$, seen in the 24° grain-boundary junction data in Fig. 4-8, is not as pronounced for the ramp-type junction, due to its relatively higher I_c and lower R_n than the grain-boundary junction. At low temperatures, the

I_c approaches the rf current level where losses occur in the film separate from the JJ, masking any saturation effect. However, the $T = 60$ K plot, which has the lowest I_c, does show a decrease in slope at $I_{rf} \approx 0.1$ A, corresponding to $R_n = 10$ mΩ obtained from dc measurements, although R_j then begins to increase due to film dissipation effects, before the saturation is complete. The relatively lower R_n in the ramp-type JJ allows film effects to influence the measurements, as can be observed in Fig. 4-7 where the $1/Q$ for the $n = 1$ and $n = 2$ modes converge at large rf current levels.

The Josephson-junction reactance X_j is obtained from the measured shifts in the resonant frequency in the following manner. The total reactance X_T of the entire stripline-resonator JJ device is proportional to the total inductance $\mathcal{L}_T$ of the device, $X_T = \omega \mathcal{L}_T$. The resonant frequency has a functional dependence on $\mathcal{L}_T$ given by $f = 1/2\pi\sqrt{\mathcal{L}_T C}$, with C, the geometric capacitance being a constant. From these relations it follows that

$$\frac{\Delta X_T}{X_T} = \frac{\Delta \mathcal{L}_T}{\mathcal{L}_T} = \frac{-2\Delta f}{f}. \tag{4.6}$$

The total inductance has three contributing terms, $\mathcal{L}_T = \mathcal{L}_g + \mathcal{L}_k + \mathcal{L}_j$ where $\mathcal{L}_g$ is the geometrical inductance of the stripline resonator, $\mathcal{L}_k$ is the kinetic inductance of the superconducting electrons, and $\mathcal{L}_j$ is the inductance due to the JJ. The $\mathcal{L}_g$ and $\mathcal{L}_k$ terms are assumed to be independent of the rf current level. From these assumptions, it follows that $\Delta X_T = X_T(I_{rf}) - X_T(0) = X_j$. Unlike the resistance, where the magnitude of the resistance due to the JJ is very large compared to the superconducting film, the reactance change due to the JJ is small compared to the total reactance of the rest of the film. A numerical value for $X_T = X_g + X_k + X_j \approx X_g + X_k$, is determined using values for $\mathcal{L}_g$ and $\mathcal{L}_k$ obtained from Sheen *et al.*[28] From this analysis, the JJ reactance is given by

$$X_j(I_{rf}) = \frac{-2\Delta f}{f}(X_g + X_k) = \Lambda \frac{f(0) - f(I_{rf})}{f(0)} \tag{4.7}$$

with $\Lambda = 93.2\,\Omega$. As with Eq. 4.5, this result applies to the stripline geometry shown in Fig. 4-4.

The results of measurement of $X_j(I_{rf})$ on the 24° grain-boundary junction is shown in Fig. 4-10 for three different temperatures. As with the JJ resistance shown

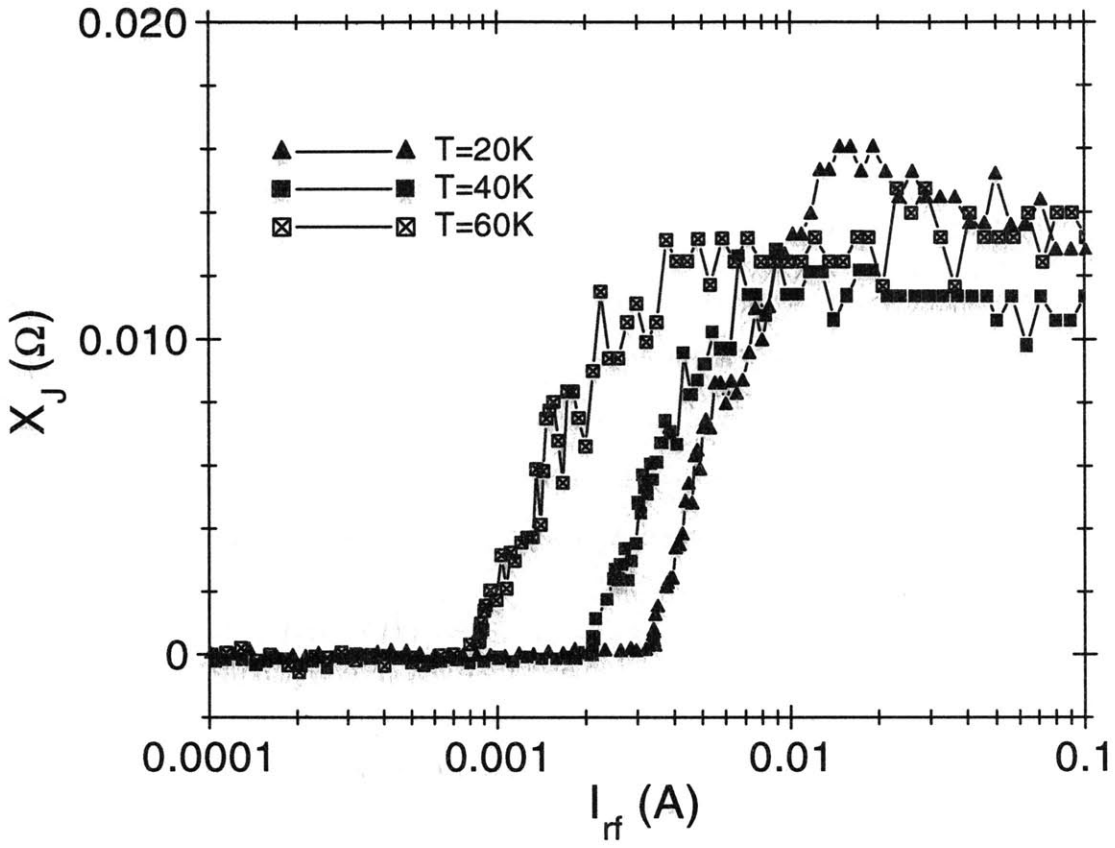

Figure 4-10: The measured JJ reactance as a function of rf current $X_j(I_{rf})$ presented on a semi-log plot for three different temperatures. These measurements were performed on the same 24° grain-boundary JJ as Fig. 4-8. The sharp onset in X_j is due to an inductance increase associated with the nucleation of fluxons in the junction by rf currents. As T is increased, the sharp rise in $X_j(I_{rf})$ occurs at lower values of I_{rf}. For a given temperature, the rise in X_j occurs at the same value of I_{rf} as the increase of R_j in Fig. 4-8.

in Fig. 4-8, the JJ reactance data show the existence of a critical rf current value where X_j begins to increase sharply. For a given temperature, the reactance increases in Fig. 4-10 occur at the same rf current level as the resistance increases shown in Fig. 4-8, because the increases in R_j and X_j result from the same JJ dynamics. The change in reactance is attributed to the inductance change associated with fluxon generation in the grain boundary by the rf currents, as will be explained in the next section. The reactance X_j at all temperatures in Fig. 4-10 is seen to rise sharply and then level off. On comparing Figs. 4-8 and 4-10, one sees that the current range from the initial rise

of X_j to the saturation level is about the same as that of R_j for a given temperature.

The stripline-resonator technique thus allows for the direct measurement of the microwave-frequency power handling of engineered Josephson junctions. Measurements of both ramp and grain-boundary type JJs show the existence of critical rf current levels where R_j increases sharply in a stepped like structure. A saturation $R_j = R_n$ was measured on the 24° grain boundary JJ. Comparison of $X_j(I_{rf})$ and $R_j(I_{rf})$ and their temperature dependences suggests that the increases in R_j and X_j are both due to a common mechanism. The electrodynamics of Josephson junctions at microwave frequencies are examined in the next section using a long-junction model.

4.2 Long Junction Model

Before introducing the long-junction model, it is necessary to give credit to my collaborators who worked on this project. While I was an active participant in the development of this model from inception to completion, Capt. Christopher J. Lehner in his M.S. thesis did most of the work necessary to implement the computer programming for the model.[60, 61] In addition, Dr. Nathan Belk, a former graduate student in our group, contributed to the early development of the model.

4.2.1 The Modeled System

The experimental grain-boundary JJ system being modeled is presented schematically in Fig. 4-11, showing a section of the center conductor of the stripline-resonator from Fig. 4-4 which consists of a superconducting transmission line incorporating the Josephson junction. The Cartesian coordinate system and relevant structural dimensions used in the modeling are defined in Fig. 4-11 which introduces d as the junction interlayer thickness. As previously defined, values of the stripline width and thickness were taken as $w = 150\,\mu$m and $t = 0.14\,\mu$m. The fundamental length scale that determines the electrodynamic properties of the JJ is the Josephson penetration

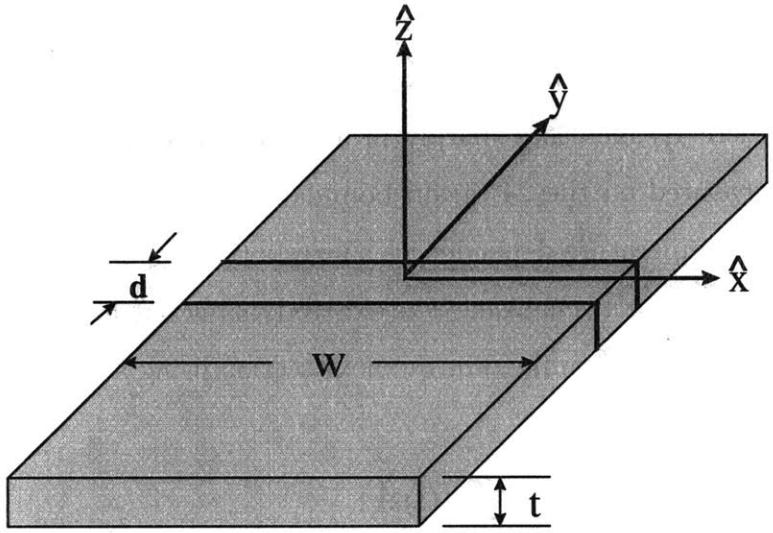

Figure 4-11: The Cartesian coordinate system and relevant structural dimensions used to model the experimental grain-boundary JJ system shown in Fig. 4-4. A section of the superconducting stripline-resonator transmission line incorporating the Josephson junction is shown. The JJ interlayer thickness is d, while w is the width and t the thickness of the YBCO film.

depth λ_j, given by

$$\lambda_j = \sqrt{\frac{\Phi_0}{2\pi\mu_0 J_c d_m}} \approx 2\mu\text{m}, \tag{4.8}$$

where $d_m = 2\lambda_l + d \approx 2\lambda_l$ is the magnetic thickness of the junction. The interlayer thickness d is negligible compared to λ_l since for a grain boundary, d is on the order of a few lattice constants, in the nanometer scale, while $\lambda_l \approx 0.2\,\mu$m. The electrodynamics of the JJ shown in Fig. 4-11 are completely described by the sine-Gordon equation,[21, 49]

$$\lambda_j^2 \nabla^2 \phi = \sin\phi + \tau_j \frac{\partial \phi}{\partial t} + \tau_{RC}\tau_j \frac{\partial^2 \phi}{\partial t^2} \tag{4.9}$$

where $\phi(x,z,t)$ is the gauge-invariant phase difference across the junction, τ_j is the Josephson time constant, and τ_{RC} is the capacitive time constant. The characteristic Josephson frequency f_j, or the time constant τ_j, is determined by Eq. 4.2 to be,

$$f_j = \frac{1}{\tau_j} = \frac{2\pi}{\Phi_0} I_c R_n = \frac{2\pi}{\Phi_0} J_c \rho_n d_e, \tag{4.10}$$

where $d_e \approx d$ is the effective electrical thickness of the JJ. The RC time constant τ_{RC} is given by

$$\tau_{RC} = R_n C_j, \tag{4.11}$$

where $C_j = \epsilon t w / d_e$ is the capacitance of the system in Fig. 4-11 using a parallel plate approximation and ϵ is the effective dielectric constant of the interlayer. Using the results of Zhang *et. al*[62] to determine the effective ratio of $d_e/\epsilon/ = 2.9$ Å for the YBCO grain-boundary, sets the upper limit for the value of $\tau_{RC} \approx 0.2$ ps. The maximum value of the $I_c R_n$ product determined from dc measurements is $I_c R_n = 1$ mV, which corresponds to a minimum value of $\tau_j \approx 0.3$ ns. The rf period of the 3 GHz fundamental resonance mode is $\tau_{rf} \approx 0.3$ ns. The relative values of the time constants determine that the term containing τ_{RC} in Eq. 4.9 is negligible since $\tau_{RC} \ll \tau_j$. A negligible capacitance is characteristic of an overdamped junction[21, 49] and is in agreement with the characteristics of the dc I-V measurements. In addition, since $t \ll \lambda_j$, any spatial variation of ϕ in the z-direction is also negligible.[19] However, since $\lambda_j \approx 2\mu$m $\ll w = 150\mu$m, the variation of ϕ in the x-direction is important and functionally $\phi = \phi(x,t)$. The dynamics of the junction being modeled are thus described by the one-dimensional, over-damped form of Eq. 4.9,

$$\frac{J(x,t)}{J_c} = \lambda_j^2 \frac{\partial^2 \phi}{\partial x^2} = \sin\phi + \tau_j \frac{\partial \phi}{\partial t} \tag{4.12}$$

which describes the dynamics of what is referred to as a long junction.

The rf impedance of a long junction can be calculated numerically using solutions to Eq. 4.12 for $\phi(x,t)$ subject to the condition that the rf driving current to the junction has the distribution shown in Fig. 4-5. In this work, an equivalent circuit model is employed which simulates the dynamics described by Eq. 4.12 while simultaneously imposing the condition that the rf driving current to the JJ has the

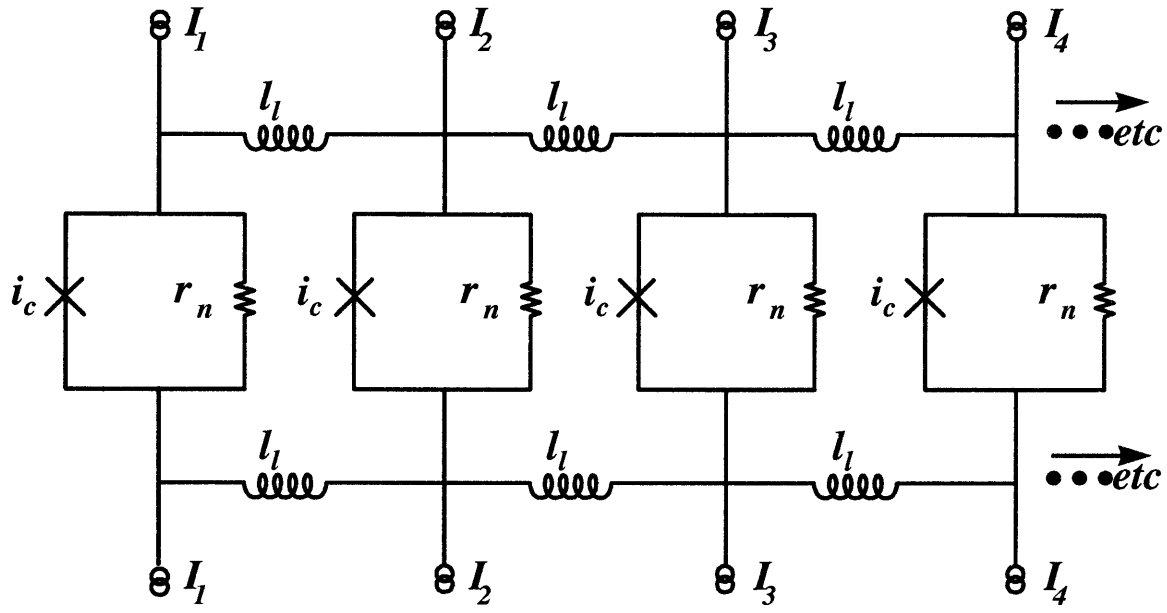

Figure 4-12: The extended resistively-shunted junction (ERSJ) model. An equivalent circuit is used to model the long-junction dynamics described by Eq. 4.12. A parallel array of ideal resistively-shunted junctions that are characterized by the parameters of critical current i_c and normal resistance r_n are linked by lateral inductors l_ℓ which simulate the magnetic coupling present in a long junction. Each individual RSJ cell has a separate rf current source that allows the stripline current distribution in Fig. 4-5 to be the driving source for the long junction. While only 4 RSJ cells are shown here for clarity, typical calculations used 100 or more.

distribution shown in Fig. 4-5. A part of the long-junction circuit model is shown schematically in Fig. 4-12. The model consists of a parallel array of N ideal resistively shunted junctions (RSJ). Each RSJ cell in the array is characterized by the

parameters of critical current i_c and normal resistance r_n. The RSJ cells are coupled by lateral inductors l_ℓ to simulate the magnetic coupling in the junction due to the finite λ_j. Each of the N individual RSJ cells has a separate rf current source that allows the stripline current distribution shown in Fig. 4-5 to be an input tp the model as the driving rf source current for the long junction. This JJ circuit model is referred to as the extended resistively-shunted junction (ERSJ) model.

To model a uniform junction, all the individual RSJ cells have identical parameters of i_c and r_n and all the coupling inductors l_ℓ have the same value, although this is not a fundamental limitation of the model. Each individual RSJ cell is governed by Eq. 4.1 and Eq. 4.2 which are sufficient to describe the dynamics of junctions with all dimensions small compared with λ_j. The total number of RSJ cells, N, must be large enough so that the spacing between the cells is less than λ_j. For typical model calculations, such as those shown here, $N \approx 100$. The long junction parameters used in the circuit are the normal resistance R_n, the critical current I_c, and the lateral inductance L_ℓ. The long JJ parameters are related to the individual circuit-element parameters as follows:

$$\frac{1}{R_n} = \frac{tw}{\rho_n d_e} = \sum_{i=1}^{N} \frac{1}{r_{ni}} = \frac{N}{r_n} \tag{4.13}$$

and

$$I_c = J_c h W = \sum_{i=1}^{N} i_{ci} = N i_c, \tag{4.14}$$

where r_n and i_c are the normal resistance and critical current of the individual RSJ cells all taken to be equal. The numerical values of I_c and R_n used in the model are obtained from the dc measurements. The value for the lateral inductance L_ℓ can be determined using two different methods that give the same results. From the dimensions of the system shown in Fig. 4-11, the geometrical inductance of a parallel-plate transmission line can be readily calculated from the following expression[18].

$$L_\ell = \frac{\mu_0 d_m w}{2t}. \tag{4.15}$$

Equivalently, L_ℓ can be derived by the method of Lehner *et al.* [60] by calculating the

inductance of an isolated Josephson-vortex in a long JJ which is given by

$$L_\ell = \frac{\Phi_0}{4\pi I_c}\left(\frac{w}{\lambda_j}\right)^2. \tag{4.16}$$

Then, the individual inductors in the model are determined by $L_\ell = 2Nl_\ell$.

Using these input parameters, the circuit in Fig. 4-12 is then evaluated numerically using JSIM[63], a circuit-solving computer program that incorporates JJ dynamics, to determine $\phi(t)$ at each node in the ERSJ circuit. The $\phi(t)$ is then used to calculate the voltages $V_i(t)$ and currents $I_i(t)$ of each of the circuit elements. The total ERSJ impedance is then determined using the power relation for an applied rf current $I_{\rm rf} = I_a \sin\omega t$ to calculate an effective time dependent junction voltage. Then, from the time-varying phases and voltages of the model junctions, the rf impedance, fields, and currents of the long junction can be calculated as described below.

4.2.2 Modeling Results

The effective resistance $R_{\rm eff}$ in the ERSJ model is given by the sum of the energy dissipated per rf period $\tau_{\rm rf}$ in the resistors divided by the root-mean square of the current. Fourier analysis of the junction voltage can be used to calculate both the resistance and reactance as well as the harmonic generation.[64] The spatial dependence of the currents in the ERSJ circuit is accounted for by calculating an effective voltage $V(t)$, that is determined from the total power $P(t)$ and total current $I(t)$ in the circuit, and is given by

$$V(t) = \frac{P(t)}{I(t)} = \frac{\sum_{i=1}^{N} V_i(t) I_i(t)}{I_0 \sin(\omega t)}, \tag{4.17}$$

where the sum over i includes contributions from the junction, resistor, and two inductors in each of the N unit cells of the model in Fig. 4-12. The lateral inductors l_ℓ must be included because they represent the magnetic-field energy stored in the long junction. The in-phase Fourier components R_m of the time-varying effective voltage are given by

$$R_m(I_a) = \frac{1}{\tau_{\rm rf} I_{\rm rms}^2}\int_{\tau_{\rm rf}} V(t) I_0 \sin(m\omega t) dt \tag{4.18}$$

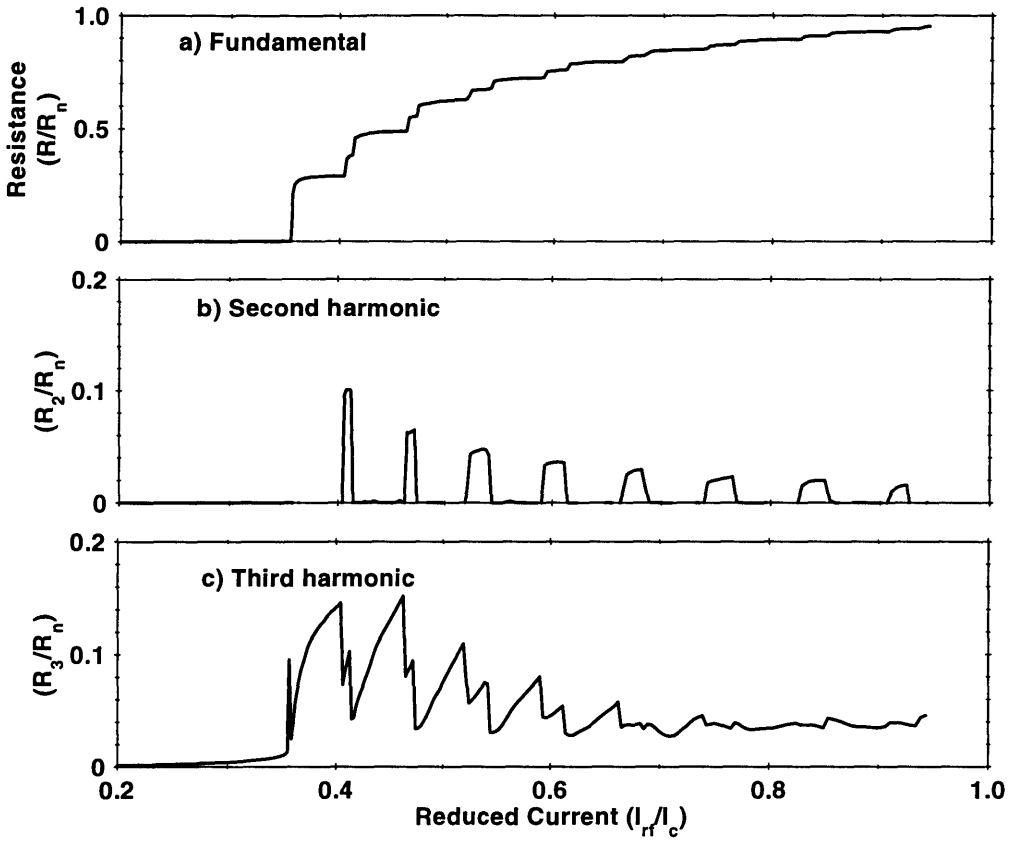

Figure 4-13: The results of the calculations using the ERSJ model. The normalized JJ resistance, the second, and third harmonics are shown as functions of the normalized rf current.

and the out-of-phase components X_m are given by

$$X_m(I_a) = \frac{1}{\tau_{\rm rf} I_{\rm rms}^2} \int_{\tau_{\rm rf}} V(t) I_0 \cos(m\omega_{\rm rf} t) dt \tag{4.19}$$

where $m = 0, 1, 2, \ldots$ is the harmonic index. The R_0 is always zero and X_0 is the dc component. The R_1 and X_1 terms give the effective resistance and reactance of the junction, respectively. The R_2 and X_2 terms are the in-phase and out-of-phase components of the second harmonic generated by the circuit and so forth. The results of the model calculations showing the normalized JJ resistance, the second, and third harmonics as functions of rf current are shown in Fig. 4-13. As with the measured data, the resistance shows a sharp increase beginning at a critical rf current level,

and the increase in the resistance is accompanied by steps in the current dependence. Interestingly, the modeling results show that a second harmonic is also generated. The origins of the steps in the resistance and the generation of second harmonic will be explained after the modeling results are compared with the experimental results.

4.3 Comparison of Measurements and Modeling

Examination of the limiting behavior obtained from the ERSJ model by changing L_ℓ substantially from the value of $L_\ell \approx 10^{-10}$ H obtained using Eq. 4.15, helps to verify that the long junction model is working properly. Making L_ℓ very small ($L_\ell \rightarrow 0$ limit) simulates the case where $\lambda_j \gg w$ which is a small junction RSJ limit. In this case, the ERSJ model reduces to the one-dimensional RSJ model with a uniform current distribution. On the other hand, if L_ℓ is increased substantially ($L_\ell \rightarrow \infty$ limit) without decreasing the effective junction spacing, the results obtained are identical to solving the one-dimensional RSJ model and then averaging the results over the current distribution shown in Fig. 4-5. This current averaged RSJ model has been presented for fitting measurements for the ramp-type SNS junctions.[57, 58] The effect of increasing L_ℓ is to uncouple neighboring cells in the ERSJ model so that each junction is independent and lateral currents are negligible. In both limiting cases, long-junction effects do not occur and Josephson vortices cannot exist in the circuit.

The measured rf current dependence of the JJ resistance $R_j(I_{rf})$ and the reactance $X_j(I_{rf})$ taken at 20 and 50 K are shown in Figs. 4-14 and 4-15, respectively. The solid lines in Figs. 4-14 and 4-15 are fits to the data using the results of the ERSJ model, which uses the inductance calculated in Eq. 4.15. The dashed line shows a fit using the model results in the $L_\ell \rightarrow \infty$ uncoupled (no vortices) limit, equivalent to the current averaged RSJ model. To fit the resistance data, the finite value of R_j in the low current limit due to the R_s of the YBCO film is added to the model results. A critical rf current level I_f where the resistance and reactance first increase abruptly in Figs. 4-14 and 4-15 is marked with arrows. The rf current level $I_{rf} = I_f$

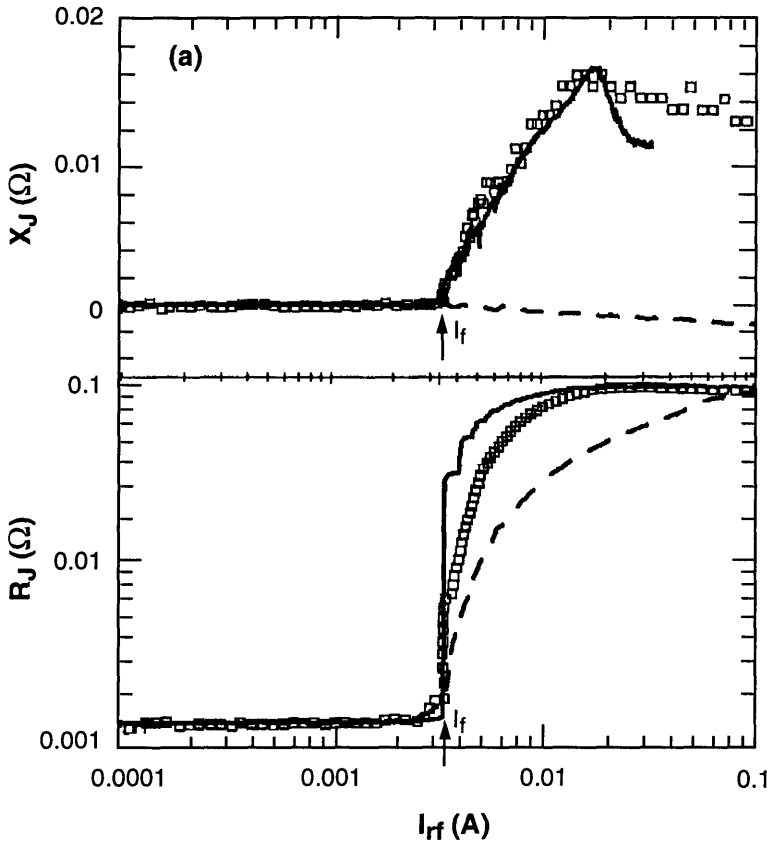

Measured effective JJ resistance and reactance vs rf current, $R_j(I_{rf})$ and $X_j(I_{rf})$ (points), for the $\theta = 24°$ grain boundary JJ at $T = 20$ K compared with two fits from the modeling (lines). The solid lines are from the ERSJ model which allows for Josephson vortex formation, while the dashed lines correspond to the model in the $L_l \to \infty$ limit where vortices (fluxons) play no role. The fluxon nucleation current I_f is marked with arrows in each plot. When vortices are allowed to exist in the model, both the stepped increases in the resistance and increases in the reactance occur, as is also observed in the measured data.

Figure 4-14:

is that which first exceeds the JJ critical-current density sufficiently on the edges of the stripline that a Josephson oscillation will occur at the stripline edge, nucleating a fluxon which results in a Josephson vortex moving into the junction. This concept is further developed in the next section.

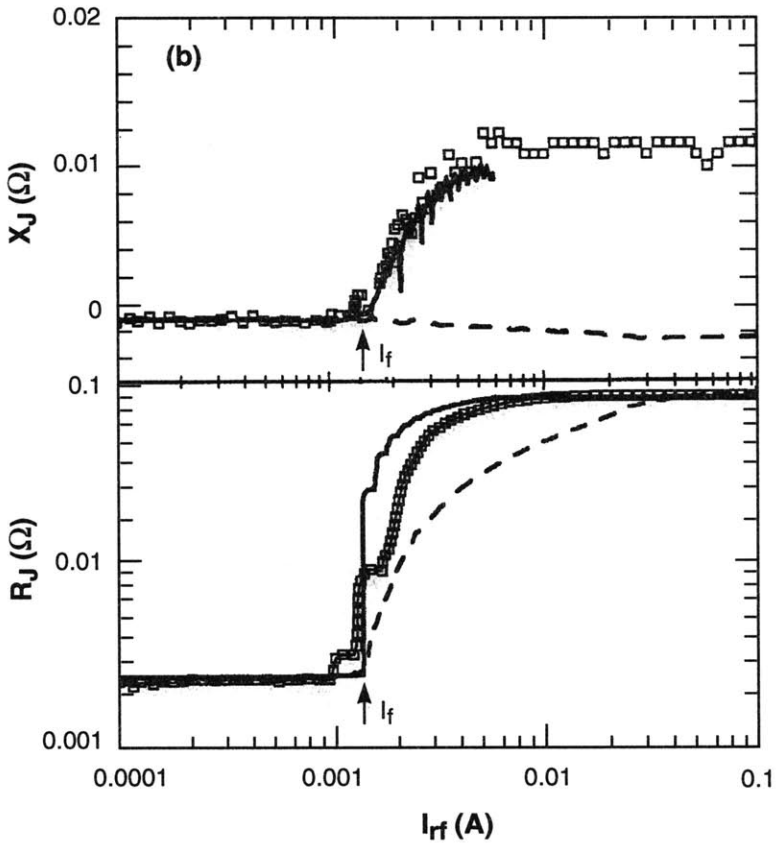

Figure 4-15: Measured effective JJ resistance and reactance vs rf current, $R_j(I_{rf})$ and $X_j(I_{rf})$ (points), for the $\theta = 24°$ grain boundary JJ at 50 K compared with two fits from the modeling (lines). The solid lines are from the ERSJ model which allows for Josephson vortex formation, while the dashed lines correspond to the model in the $L_l \to \infty$ limit where vortices (fluxons) play no role. The fluxon nucleation current I_f is marked with arrows in each plot. When vortices are allowed to exist in the model, both the stepped increases in resistance and increases in the reactance occur, as is also observed in the measured data.

Examination of the resistance plots in Figs. 4-14 and 4-15 shows step structures evident in the measured $R_j(I_{rf})$ in the vicinity of I_f. There are also steps in the $R_j(I_{rf})$ results obtained from the long junction model when currents are allowed to redistribute through the inductors and form vortices (solid lines). However, when current redistribution cannot occur ($L_l \rightarrow \infty$ limit), the modeling does not show steps (dashed lines). The steps in the modeled and measured data have different sizes, but the overall character of the curves is qualitatively the same. The lack of quantitative agreement of the step height and width could be due to imperfections in the engineered junction, which are not accounted for in the idealized model. The presence of defects in the engineered grain boundary samples could result in local variation in I_c or R_n and defects can also act as pinning sites for Josephson vortices. The origin of the steps in the calculated $R_j(I_{rf})$ curve is fluxon quantization, and the increases in resistance are due to the creation, annihilation and motion of Josephson vortices by rf currents in the long junction.

The values of I_c and R_n obtained from the dc measurements are compared in table 4.1 with those obtained by fitting the rf measurements with the modeling results. The dc results were used as initial inputs to the model, but the I_c values had to be adjusted to obtain good agreement with the I_f obtained in the rf measurements. The same parameters were used to fit the R_j and X_j data at a given temperature. The values of R_n obtained for the rf and dc cases are about the same. The rf value of R_n is equal to the saturation value of the $R_j(I_{rf})$ data. The I_c obtained from the rf results is higher than the dc value. The rf value of I_c is adjusted to obtain the best fit between the model and experiment. The general modeling results indicate that the rf value of I_c is about 4 times greater than I_f, as can be seen in Fig. 4-13, which is plotted on a current scale normalized to I_c. The difference between I_f and the rf I_c is due to the rf current distribution shown in Fig. 4-5, which causes J_c to be exceeded at the JJ edges while not being exceeded the center.

Examination of the $X_j(I_{rf})$ plots in Figs. 4-14 and 4-15 shows the measured reactance increasing sharply above I_f at both temperatures. This reactance change is due to the increased inductance associated with Josephson fluxons nucleating in the

Table 4.1: Comparison of the I_c and R_n values obtained from the dc measurements, with those obtained from fitting the rf measurement results using the ERSJ model.

Temperature	I_c mA		R_n mΩ	
	dc	rf	dc	rf
20 K	8.9	14.0	80	81
50 K	3.5	4.8	80	86

long JJ. The ERSJ model, which allows Josephson vortices, shows the same overall features as the measured data, including a rise and then a leveling off of X_j, with the height, onset and slope of the rise showing good agreement. On the other hand, the RSJ limit without vortices (dashed line in Figs. 4-14 and 4-15) predicts a slight decrease in $X_j(I_{rf})$ above I_f while the measurements clearly do not show such a decrease. This basic agreement between the long junction model and the measured data adds credence to the idea that fluxons are responsible for the measured reactance increase, and that the data show the effects of Josephson vortices nucleated by rf currents. The modeling is not presented over as large a current range as the data, because the modeling, which is all computationally intensive, becomes more so at higher current levels. Thus, the range of rf currents over which the simulations could be carried out for this work was limited by the available computer resources.

4.3.1 Josephson Vortex Generation by Microwave Currents

As has been asserted in the previous sections, it is the nucleation of Josephson vortices by rf currents in the JJ that causes the step structures in $R_j(I_{rf})$, and of the sharp increases in $X_j(I_{rf})$ and in $R_j(I_{rf})$. Josephson-vortex nucleation in the stripline geometry is initiated by the rf current at the edges of the junction, where the current density is greatest. When the rf input-current level to the ERSJ model is small enough to be well below I_c of the edge junctions in the circuit, all the current can flow through

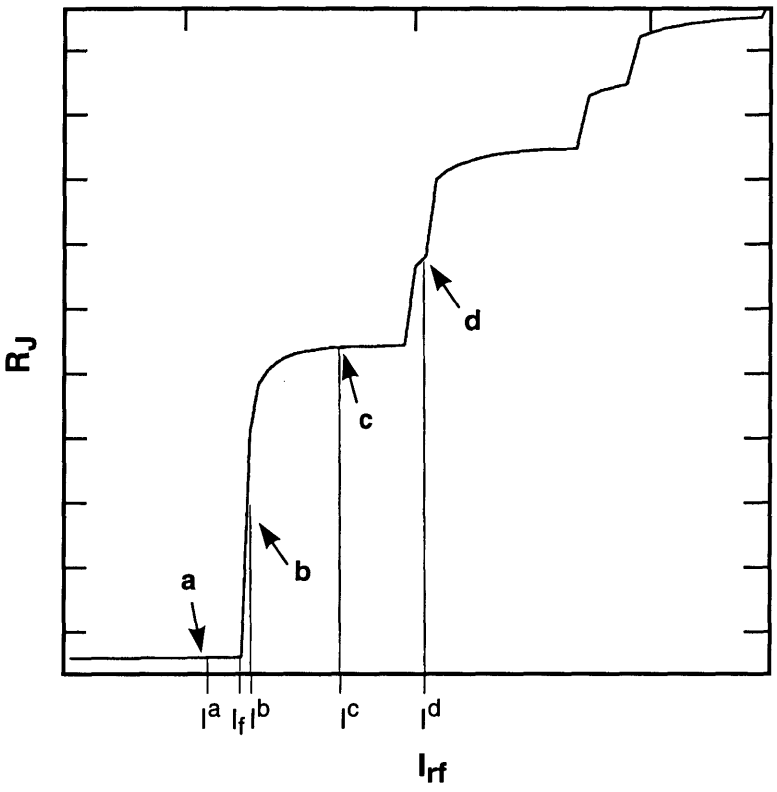

Figure 4-16: Calculated resistance as a function of rf current obtained from the ERSJ model. Four positions on the curve are marked a, b, c, and d, with each corresponding to an rf current level I^a, I^b, I^c, and I^d. Step structures are seen to evolve in the plot with increasing I_{rf}.

the JJs and negligible currents flow through the inductors. As the I_{rf} to the circuit is increased to a level approaching I_c of the edge JJs, some currents will go through L_ℓ and then flow through the inner junctions. Even when the input I_{rf} is sufficient to exceed the I_c of the edge JJs without redistribution, the currents can redistribute, and avoid triggering a Josephson oscillation at the edge. It is when I_{rf} reaches a level that causes a Josephson current oscillation (2π phase slip) at the edges of the long junction that stepped losses and sharp increases in the resistance and reactance begin to occur, and it is this level which is marked as I_f in Figs. 4-14 and 4-15). A Josephson oscillation occurs when the current in the junction first passes through I_c and then goes back to zero (phase change of π) in one half of an rf cycle. In the pendulum model of an overdamped JJ [19], ϕ is analogous to the deflection angle θ which will certainly fall to 2π when pushed past an angle of $\theta = \pi$. Similarly, once $\phi = \pi$ in the JJ, ϕ will necessarily slip another π in phase which then nucleates a fluxon as the phase change is directly related to the flux through the junction, $\Delta\phi(t)/2\pi = \Phi(t)/\Phi_0$. Concurrent with the 2π change in ϕ, the current redistributes itself through the ERSJ circuit forming a Josephson vortex. The Josephson oscillations cause more current to flow through the resistors in the RSJ cells, resulting in resistive losses. The increase in magnetic flux is responsible for increases in X_j while flux quantization results in the steps in R_j observed at 20 K (Fig. 4-15) and at 50 K (Fig. 4-14).

On the edge of the JJ, when $I_{rf} \geq I_f$, fluxons are nucleated on the positive half of the rf cycle and antifluxons are nucleated on the negative half of the cycle. These fluxons and antifluxons correspond directly to Josephson vortices and antivortices where an antivortex has current circulating in the opposite direction to the current circulation for a vortex. When vortices meet antivortices in the junction, they annihilate each other. Power is dissipated due to normal currents when Josephson vortices are created or annihilated, with resistive losses also being attributable to the motion of vortices under the influence of the rf currents. Since the junction is overdamped, the Josephson vortices move only under the influence of the rf current. As the rf current increases, more Josephson vortices and antivortices move in and out of the junction. Due to the symmetry of the system, when vortices are created on one edge

of the JJ, antivortices are created on the opposite edge. Moreover, when the rf current is large enough to create a vortex at the edge and move it to the center of the long JJ, the vortex will meet an antivortex coming from the other side and the two will annihilate in the center. A saturation level is reached where $R_j = R_n$, and X_j no longer increases with increases in I_{rf}, as shown in Figs. 4-14 and 4-15.[59]

The effect of fluxon generation and the creation of Josephson vortices by rf currents in a long junction can be further understood by sequentially examining the magnetic flux $\Phi(t)$ in the ERSJ circuit as a function of time to show fluxon nucleation and by examining the current distribution $I(x)$ as a function of position to show Josephson vortex formation. Fig. 4-16 shows the $R_j(I_{rf})$ which was used to fit the 20-K data in Fig. 4-14; the $R_j(I_{rf})$ curve shows clear stepped structures (the plot is on a linear scale, while the fitted data in Fig. 4-14 are plotted on a log-log scale). Marked with arrows in Fig. 4-16 are four positions on the curve a, b, c, and d, which correspond to the rf current levels denoted as I^a, I^b, I^c and I^d in Fig. 4-16. Also shown in Fig. 4-16 is the fluxon-nucleation current I_f, which was introduced in Figs. 4-14 and 4-15. When the input current I_{rf} is equal to I^a, which is slightly below I_f, the magnitude of $R_j(I_{rf})$ is almost constant upon variation of the rf current and $R_j(I_{rf} = I^a)$ has about the same value as $R_j(I_{rf} \approx 0)$. No appreciable losses have occurred in the junction at this current level. When the current is increased slightly to $I_{rf} = I^b$, with $I^b = I_f + \delta I$, it is apparent that $R_j(I_{rf})$ has risen abruptly [there is a very small plateau at (b), which is not resolved in Fig. 4-16]. The junction is now causing increased rf power losses at the point b in Fig. 4-16 due to the increased resistance relative to the point a in Fig. 4-16. When the current is increased to $I_{\rm rf} = I^c$, then $R_j(I_{rf})$ has further increased and reached a plateau. Finally, when $I_{\rm rf} = I^d$, the $R_j(I_{rf})$ has again increased and has reached another plateau which is narrower than the one marked c in Fig. 4-16. As the current is further increased, steps continue to develop, alternating between smaller and larger plateaus. Each stepped increase is due to an additional fluxon nucleating in the long JJ during each rf cycle. The plateaus correspond to ranges where the number of fluxons generated per cycle by the rf current is constant.

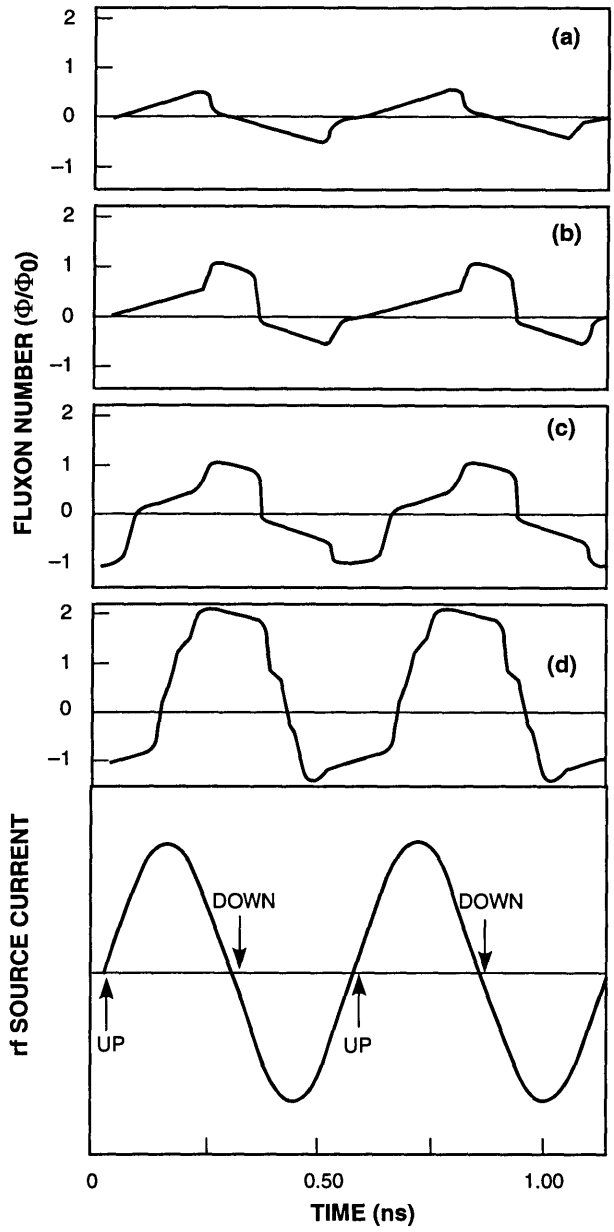

Figure 4-17: Fluxon number as a function of time, $\Phi(t)/\Phi_0$ for half the long junction as calculated by the ERSJ model. The four plots (a), (b), (c), and (d), correspond to the current levels marked accordingly in Fig. 4-16. This figure demonstrates how the flux increases in discrete quantized units. The bottom shows the rf source current using a common time scale for the source current and the flux. Any flux present at the source current nodes is due to Josephson vortices. Note that (a) and (c) are symmetric about $(\Phi(t)/\Phi_0) = 0$, while (b) and (d) are asymmetric.

The total magnetic flux $\Phi(t)$ existing in half the ERSJ circuit (i.e., half the 150-μm-long JJ) is shown in Fig. 4-17. Only half needs to be shown because the long junction is spatially symmetric about its midpoint, as is the current distribution in the stripline. In addition, when fluxons are generated on one side of the junction, antifluxons are generated on the other side, and while the nucleation of both fluxons and antifluxons causes losses, calculation of the total flux through the whole junction would sum to zero. Shown are four different $\Phi(t)$ plots in Fig. 4-17 (a), (b), (c) and (d), with each plot showing the $\Phi(t)$ generated in the JJ by rf current levels corresponding to I^a, I^b, I^c and I^d in Fig. 4-16 respectively. The $\Phi(t)$ is calculated from the ERSJ model by summing the flux due to the currents flowing in L_ℓ such that $\Phi(t) = \Sigma_{i=1}^{N-1} L_{li} I_i(t)$, where the sum on i is over the $N-1$ inductors in half the ERSJ circuit. Shown below the $\Phi(t)$ plots in Fig. 4-17 is the rf source current $I_{\rm rf}(t)$ ($f = 3$ GHz) on the same time scale as $\Phi(t)$. The nodes in the sine wave, where the rf source current is zero, are marked as up and down. Any flux present in the junction at the nodes is due only to Josephson vortices. Figure 4-17(a) depicts $\Phi(t)$ for the rf current level I^a in Fig. 4-16 which is slightly less than I_f. A small background flux ($|\Phi| < \Phi_0/2$) is seen with the same periodicity as the source current, corresponding to a maximum phase change along the junction of just less than π, showing an incipient but not fully formed Josephson oscillation (fluxon). We note that there is no flux present [i.e., $\Phi(t) = 0$] in Fig. 4-17(a) at the rf source current nodes which implies that the periodic flux seen is due to the source current.

When the current is increased to I^b in Fig. 4-16, which is a very small amount greater than the fluxon nucleation current $I^b = I_f + \delta I$, the corresponding $\Phi(t)$ plot, Fig. 4-17(b), shows one fluxon nucleating in the first half of the rf cycle and then annihilating in the second half of the rf cycle. The phase in the JJ changes by 2π (one fluxon) in each half of the rf cycle, indicating that a Josephson oscillation is occurring in each half cycle. Fig. 4-17(b) shows that there is a fluxon in the junction [$\Phi(t) = \Phi_0$] at the time of the down nodes in $I_{\rm rf}$, but the fluxon gets annihilated on the negative half of the rf cycle so that at the up node of the source current, the flux is zero. It is interesting that the nucleation event occurs on the downward part of the

positive rf cycle as the source current amplitude is decreasing. The nucleation and annihilation of one fluxon per rf cycle causes an abrupt and substantial increase in $R_j(I_{rf})$ as shown in Fig. 4-16.

When the current is increased to the level corresponding to I^c in Fig. 4-16, the corresponding $\Phi(t)$ plot, Fig. 4-17(c), shows that a fluxon nucleates and annihilates in each half of the rf cycle. Figure 4-17(c) shows that there is a fluxon in the junction at the time of the down nodes in the source current as in Fig. 4-17(b), but on the up nodes of the rf cycle, an antifluxon $[\Phi(t) = -\Phi_0]$ is in the junction. There are now two fully nucleated flux quanta existing in the JJ per rf cycle and consequently $R_j(I_{rf})$ in Fig. 4-16 has increased another step.

Figure 4-17(d), which corresponds to the current level I^d in Fig. 4-16, shows two fluxons present at the down nodes of the rf source current and only one antifluxon at the up node. Each time the magnitude of I_{rf} increases sufficiently to add another flux quantum (fluxon or antifluxon) to the junction per rf cycle, there is a step in the $R_j(I_{rf})$ in Fig. 4-16. The rf currents nucleate and annihilate fluxons in the long junction resulting in quantifiable losses. Note that there is no gradual increase in the flux present in the JJ at the rf nodes from one current level to the next, but only quantized increases in the total magnetic flux, one fluxon at a time. This type of bifurcation of phase, or equivalently flux, has been calculated by other researchers investigating similar systems.[64, 65, 66]

Figure 4-17 showed that fluxons can exist in the junction when the rf current is zero. The fluxons are sustained by circulating supercurrents that constitute Josephson vortices. In Fig. 4-18 we show the current $I(x)$ in the ERSJ circuit as a function of position x at the times when the rf source current is zero, i.e., at the nodes. The four plots shown in Fig. 4-18 (a), (b), (c) and (d), each corresponding to the similarly labeled current levels in Fig. 4-16 and the $\Phi(t)$ plots in Fig. 4-17. In each plot in Fig. 4-18 two current distributions are shown: the solid line is the current as a function of position at the down nodes of the rf source current shown in Fig. 4-17, while the dashed line is the current as a function of position at the up node of the rf source current. The plots in Fig. 4-18 show the current distribution starting at the

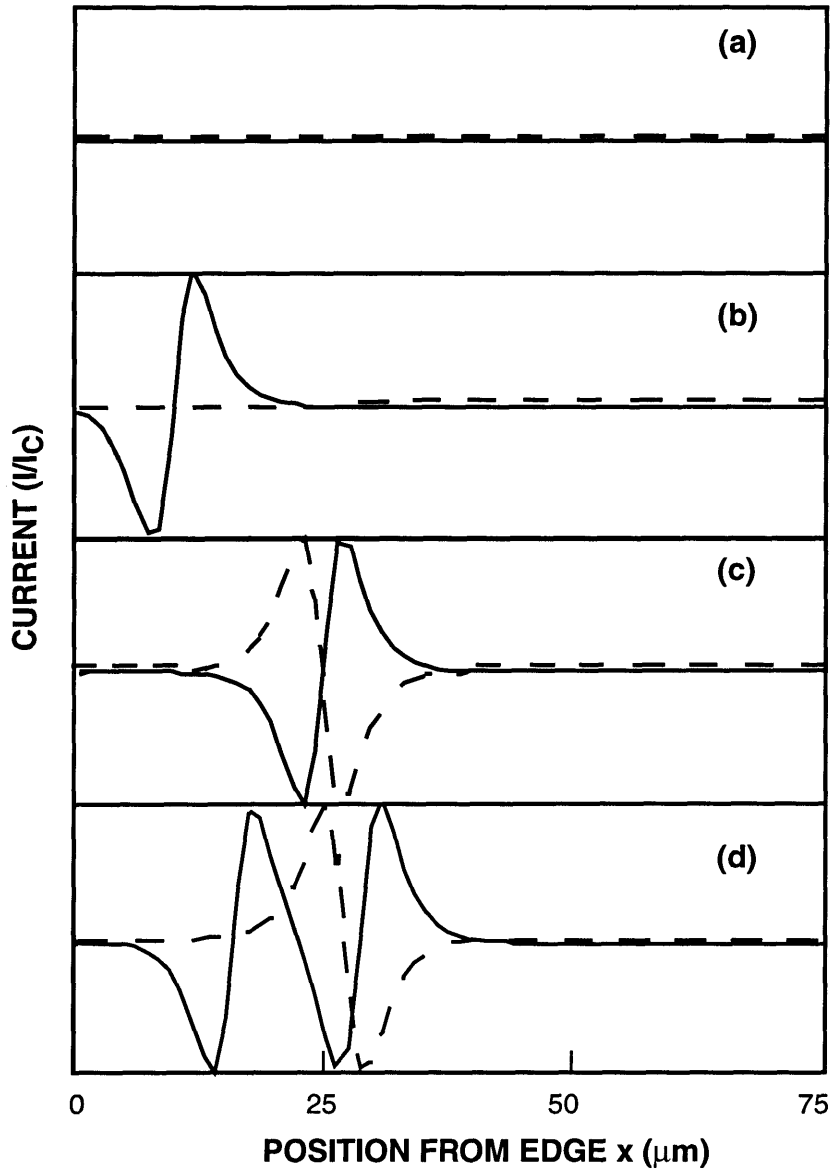

Figure 4-18: Normalized current as a function of position $I(x)$ taken at the rf source current nodes shown in Fig. 4-17. The four plots (a), (b), (c), and (d), correspond to the current levels marked accordingly in Fig. 4-16. The solid lines show the current at the down nodes of the source current, while the dashed lines show the current in the junction at the up nodes of the rf source. These plots show where the Josephson vortices are located in the junction at the source current nodes and how they move farther into the JJ with increasing rf current.

JJ edge and extending 75 μm into the 150-μm-long junction. In Fig. 4-18(a) there is no current present in the junction at either of the rf source nodes. The absence of current results from the condition of zero flux at the rf nodes shown in Fig. 4-17(a). In Fig. 4-18(b) there is one vortex present in the junction. The vortex is present at the down node of the rf source current but there is no antivortex (current distribution of opposite circulation) present in the up node. Again, this follows from Fig. 4-17(b) that shows a fluxon present at the down nodes of the rf source but no flux at the up nodes. Fig. 4-18(c) shows one vortex in the junction at the down nodes as in Fig. 4-18(b), and also an antivortex at the up node of the rf source current. This follows from Fig. 4-17(c) that shows a fluxon at the down nodes and an antifluxon at the up nodes of the rf source current. In Fig. 4-18(d) there are now two vortices at the down node of the rf source current and one antivortex at the up node. Again this follows from the $\Phi(t)$ plot in Fig. 4-17(d). It is worth noting that as more vortices (or antivortices) are generated by the rf current, they move farther into the long junction as is apparent in Fig. 4-18.

It is interesting to examine the symmetry in Figs. 4-17 and 4-18. In Fig. 4-17 plots (a) and (c) are symmetric about the $\Phi(t) = 0$ axis and they have the same periodicity as the rf source current, while (b) and (d) are asymmetric about this axis. This symmetry breaking is also seen in Fig. 4-18 where plots (a) and (c) have equal but opposite current distributions at the up and down nodes of the source current, while (b) and (d) have completely different current distributions at the up and down nodes of the source current. Since the ERSJ model and the rf source current are symmetric, these asymmetric states were unexpected. Upon further investigation of the ERSJ model results it is found that the asymmetric states generate second harmonic signals. This can be seen by comparing Fig. 4-13 with Fig. 4-16. The modeling results indicate that second harmonic generation is a clear indication of Josephson vortex creation by rf currents[67]. This will be further examined in Chap 6.

4.4 Conclusions

The results of the measurements and modeling presented in this chapter give strong evidence that it is possible to directly measure the complex impedance due to fluxons being nucleated in bicrystal grain-boundary junctions. The effect of the nucleation and motion of Josephson vortices by rf currents gives rise to a nonlinear impedance, that includes step structures in the resistance due to the quantization of the magnetic flux in the Josephson junction, and reactance changes due to the increased inductance associated with fluxon generation. The engineered JJ has very little effect on the power handling of the stripline resonator until the rf current reaches a level sufficient to nucleate the first fluxon in the JJ. Josephson-vortex creation causes a sharp increase in the resistance and an associated rise in the reactance. As the rf current is further increased, more fluxons are generated in the junction and there is a step in the $R_J(I_{rf})$ every time an additional fluxon is generated in an rf cycle. The junction then alternates between states with one more fluxon than antifluxon (asymmetric states) and those with equal numbers of fluxons and antifluxons (symmetric states) during each rf cycle. The asymmetric states produce second harmonics as a signature of the generation of Josephson vortices. When the rf current is sufficient to drive Josephson vortices to the center of the junction where they annihilate with antivortices, the resistance and reactance saturate because the JJ is now in the normal state for most of the rf cycle.

This work supports the premise that the observed nonlinear microwave power-handling effects observed in high-T_c films are due to grain-boundary weak links separating superconducting grains to form a mosaic of coupled JJs. This work shows direct observation and quantification of rf Josephson vortex effects in grain-boundary junctions. Recent work has shown that the nonlinearities in the high-T_c films can be explained by the coupled-grain model using a distribution of I_cR_n products in the grain boundaries.[68] Since grain-boundary weak links are an extrinsic property of the superconducting film, it follows that a further understanding of the rf electrodynamics of these structures should lead to the production of films with greater

power-handling capabilities.

Chapter 5

Grain Boundaries

The results of Chap. 3 demonstrated that the measured microwave-frequency (rf) surface impedance of YBCO thin films is linear at low levels of rf input power and becomes nonlinear as the power is increased.[25] This power dependence of the surface impedance, also known as power handling, has been attributed to the observed granularity of the films. Microstructural studies of YBCO thin films have revealed a granular composition, independent of both deposition technique and substrate material.[12, 13, 14] A proposed mechanism for the microwave power handling in YBCO thin films is that the film is an effective Josephson medium, a network of superconducting grains coupled by grain boundaries, which are Josephson-junction (JJ) weaklinks.[23, 41] The coupled-grain model agrees well with the measured results when the numerous grain boundaries distributed throughout the film have a distribution of physical characteristics.[68, 69] Thus, quantifying how the different grain-boundary properties affect rf-power handling is an important step toward the production of films with enhanced power handling capabilities.

An investigation of the rf power handling in YBCO Josephson junctions was presented in Chap. 4. The results of rf and dc measurements performed on engineered Josephson junctions (JJ), and the long-junction model calculations, provided a quantitative understanding of how Josephson vortices created by rf currents affect the rf-power handling. Microwave power-dependence measurements on a $\theta = 24°$ grain-boundary JJ demonstrated that Josephson vortices created at the grain boundaries

will cause strong nonlinearities in the impedance and result in significant power losses. In the context of the coupled-grain model, these results show that at rf current levels sufficient to exceed the critical current density of the weak links coupling the grains, the surface impedance will become nonlinear and rf power losses will increase.[59] However, microstructural studies show typical mosaic spreads of $0 - 2°$ [14, 15] implying that $\theta = 24°$ is a large-angle grain boundary. Clearly, it is important to quantify how the magnitude of θ affects the rf power handling of the grain-boundary.

In this chapter, I present a study of the dependence of the rf and dc electrodynamic properties of YBCO grain boundaries on the magnitude of θ. The results of this experimental study show that the value of θ significantly affects both the rf and dc measurement results. However, a comparison of the rf and dc results reveals a significant difference in the dependence of the I_c on θ in the rf and dc cases. I close this chapter with a discussion of how the measurement results can be interpreted in light of the coupled-grain model, and how other factors, such as the short coherence length, grain-boundary microstructure, and possible d-wave symmetry of the order parameter in YBCO influence the experimental results.

5.1 Angular Dependence of the rf and dc Electrical Properties of YBCO Grain Boundaries

5.1.1 Experiment

This study of the rf and dc properties of engineered grain boundaries (EGB) as a function of misorientation angle was conducted by first growing epitaxial, c-axis-oriented YBCO films on r-plane (1012) sapphire bicrystal substrates with misorientation angles of $\theta = 24°$, $10°$, $5°$ and $2°$. In addition, reference-film samples (RFS) were grown on single-crystal sapphire substrates. The films were all grown to a thickness of 1400 Å by pulsed-laser deposition after an epitaxial buffer layer of CeO_2 was deposited on the substrate, as has been described in Chap.2.[10] On each substrate, both a $\lambda/2$-resonator line to be used for the rf measurements and a four-point test structure

for dc measurements was patterned. Each patterned line is 150-μm wide, which corresponds to the length of the EGB. After performing the dc measurements, the dc test structure was etched off, and the resonator line was packaged with ground planes to form a stripline resonator. All measurements were performed in a magnetically shielded environment to ensure that the ambient magnetic field is less than 10^{-7} T. The rf and dc measurement techniques are the same as described in Chaps. 3 and 4.

5.1.2 rf Measurements

The rf measurements were performed using the stripline-resonator technique described in Chap. 4 that uses the properties of standing waves to directly measure the effect EGBs have on the rf power handling.[57, 59] Since the aforementioned technique has been shown to be experimentally effective, to demonstrate the effect of the EGB's on the rf power handling, all the data presented in this chapter are for the fundamental resonant mode $f_1 \approx 3$ GHz.

The loaded quality factor Q and fundamental resonant frequency f_1 of each stripline resonator was measured as a function of rf input power at temperatures from 10 to 70 K. The inverse unloaded quality factor $1/Q_u$ and the normalized resonant frequency shift $\Delta f_1/f_1(0)$ ($\Delta f_1 = f_1(0) - f_1(I_{rf})$) as a function of peak rf current (I_{rf}) were obtained from the measured data [24] as previously described. In the usual stripline-resonator method for measuring the power handling of superconducting thin films grown on single crystal substrates, the $1/Q_u$ and $\Delta f_1/f_1(0)$ data were shown to be related to the surface impedance of the film through Eqs. 3.10 and 3.24.[23] However, for a lumped-element JJ as presented in Chap. 4, the concept of surface impedance does not apply and the $\Delta(1/Q_u)$ and $\Delta f_1/f_1(0)$ are related to the resistance and inductance of the JJ through Eqs. 4.5 and 4.7.[59, 70] In this chapter, the power handling of these two cases and the intermediate values of θ are explored, so accordingly, the rf data are presented simply as the dependence of $1/Q_u$ and $\Delta f_1/f_1(0)$ on rf current to best compare the different grain-boundary orientations of the devices studied here.

The results of rf measurements performed on EGBs with misorientation angles

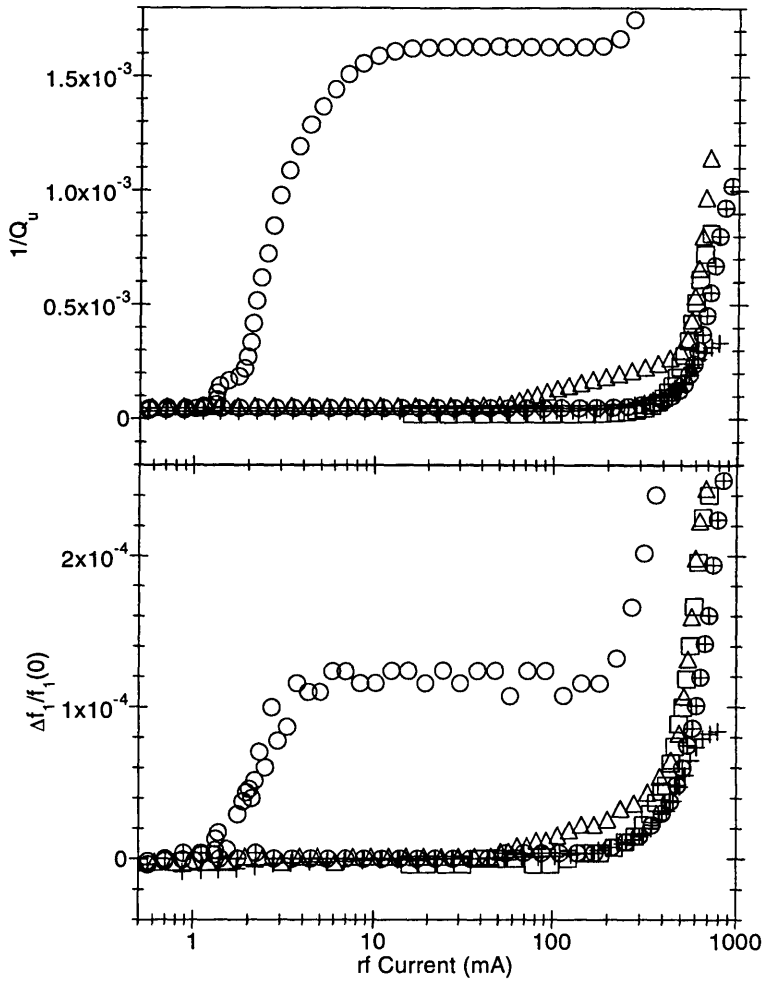

Figure 5-1: (a) Plot of $1/Q_u$ as a function of rf current. (b) Plot of $\Delta f_1/f_1(0)$ as a function of rf current. Both plots are at T = 50 K. The curves are largely indistinguishable until the rf current reaches a level where the engineered grain boundary (EGB) causes the $1/Q_u$ and $\Delta f_1/f_1(0)$ to increase relative to the reference film sample (RFS). This increase is only seen in the 24° and 10° EGBs. The symbols correspond to the different θ values as follows: $\bigcirc$ is the $\theta = 24°$ EGB, $\triangle$ is the $\theta = 10°$ EGB, $\oplus$ is the $\theta = 5°$ EGB, $\square$ is the $\theta = 2°$ EGB, and $+$ is the RFS.

of $\theta = 24°$, 10°, 5°, 2°, and the RFS, showing $1/Q_u$ and $\Delta f_1/f_1(0)$ as a function of rf current are presented in Figs. 5-1 (a) and (b) respectively,. These measurements were performed at $T = 50$ K. A similar dependence of $1/Q_u$ and $\Delta f_1/f_1(0)$ on θ and $I_{\rm rf}$ was observed at the other temperatures investigated from 10 to 70 K. At low rf current levels, $I_{rf} \leq 1$ mA, the $1/Q_u$ and $\Delta f_1/f_1(0)$ data for all the samples have a constant dependence on current, and they are indistinguishable from one another. As the rf current is increased, any effect that the EGBs have on the rf power handling will be seen as a change in $1/Q_u$ and $\Delta f_1/f_1(0)$ relative to the values of the RFS. In both Fig. 5-1 (a) and Fig. 5-1 (b), the results for the 24° EGB stand out from the other devices. When the rf current level reaches $I_{rf} \approx 1.5$ mA, both the $1/Q_u$ and $\Delta f_1/f_1(0)$ increase sharply and abruptly for the 24° EGB, while the $1/Q_u$ and $\Delta f_1/f_1(0)$ data for the other EGB misorientation angles and for the RFS remain essentially constant as the rf current is increased further by more than an order of magnitude. The sharp increases in $1/Q_u$ and $\Delta f_1/f_1(0)$ for the 24° EGB were shown in Chap. 4 to be due to Josephson vortex creation, annihilation, and motion, induced by the rf current.[59] In clear contrast to the 24° EGB, the $1/Q_u$ and $\Delta f_1/f_1(0)$ data for the $\theta = 5°$ and $\theta = 2°$ EGBs show approximately the same dependence on rf current as the RFS. When $I_{\rm rf}$ is increased to $I_{\rm rf} \approx 200$ mA, the $1/{\rm Q}_u$ and $\Delta f_1/f_1(0)$ for the RFS, 2° EGB, and 5° EGB samples all begin to increase in a similar manner that is characteristic of films grown on single-crystal substrates. The 10° EGB does have a relatively small, yet clearly discernible effect on the rf power handling, causing the $1/Q_u$ and $\Delta f_1/f_1(0)$ data to increase at $I_{rf} \approx 55$ mA. As the rf current is further increased to $I_{rf} \approx 500$ mA, the $1/Q_u$ and $\Delta f_1/f_1(0)$ data for the 10° EGB converges with that for the 2° and 5° EGBs and for the RFS.

To quantify the dependence of the rf power handling on the magnitude of θ, it is necessary to determine the relative critical currents $I_c(\theta)$ from the rf data. As discussed in Chap. 4, the rf current density distribution $J_{rf}(x)$ across the resonator linewidth is strongly peaked at the edges of the line as shown in Fig. 4-5, with an edge value of J_{rf} approximately ten times greater than the value of J_{rf} at the center of the line.[28] Thus, as I_{rf} is increased, a level is reached where J_{rf} at the edges of the line

Table 5.1: The critical currents I_c for the $\theta = 24°$, $\theta = 10°$, $\theta = 5°$, $\theta = 2°$ EGBs and the RFS obtained from the dc and rf measurements at T = 50 K. To convert the dc I_c in A, to critical current density J_c in A/m^2, multiply the I_c by 4.8 x 10^{10}. The dc value of I_c for the 2° EGB at 50 K was obtained by extrapolating temperature dependence data of I_c at higher temperatures.

Sample	I_c (A)	
	dc	rf
RFS	2.65	0.580
2° EGB	2.73	0.670
5° EGB	0.98	0.745
10° EGB	0.045	0.265
24° EGB	0.0035	0.006

begins to exceed J_c causing rf power losses and an increase in $1/Q_u$.[57] The results of the modeling presented in Chap. 4 demonstrated that the peaked current density at the edge causes the $1/Q_u$ to begin increasing when I_{rf} is approximately one-fifth of the critical current I_c value. The $I_c(\theta)$ values are then obtained from the rf data as five times the rf current level at which $1/\mathrm{Q}_u(I_{rf})$ increases by 20% from the low-current value ($I_{rf} \leq 1$ mA) and these data are given in Table 5.1. A 20% increase in $1/\mathrm{Q}_u(I_{rf})$ demonstrates a significant increase in rf power loss and has been accepted by other researchers as a critical rf current level.[43] This criterion for determining I_c from the rf data makes a quantitative comparison possible, but any reasonable definition will yield the same relative $I_c(\theta)$ and lead to the same conclusions.

5.1.3 dc Measurements

The results of dc measurements performed on the $\theta = 24°$, 10°, 5° and 2° EGBs and the RFS, taken at T = 68 K, are presented in Fig. 5-2 (a) showing the $I - V$ curves for all five samples. This is the lowest temperature for which the dc $I - V$ plots for all

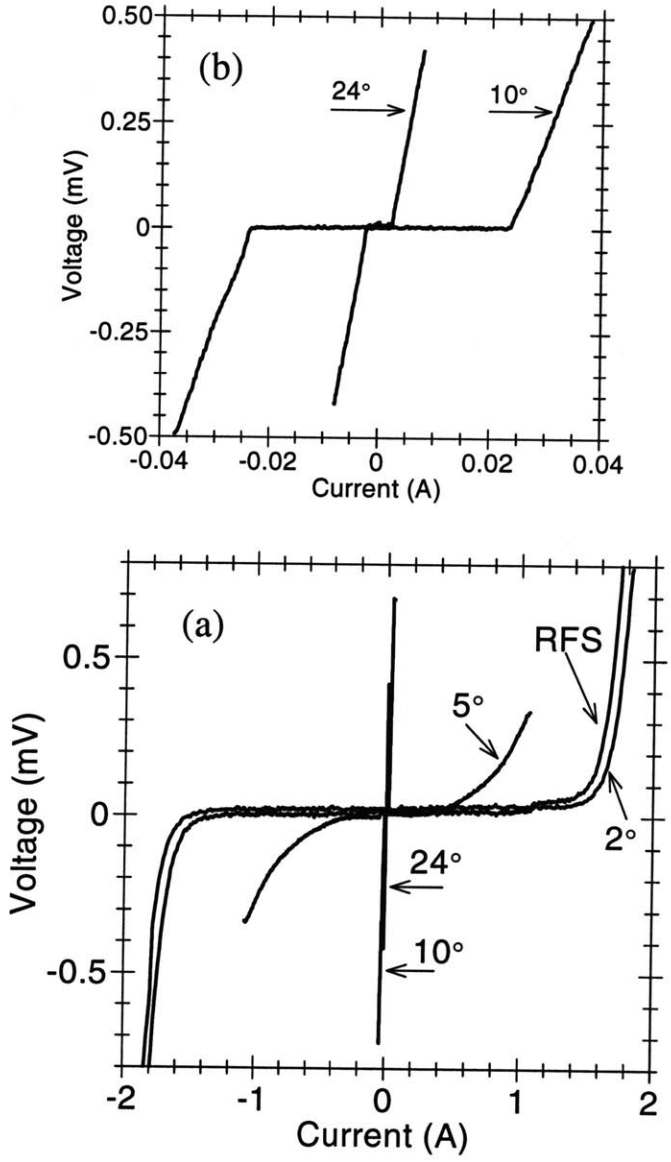

Figure 5-2: (a) The measured current-voltage $I-V$ curves for the $\theta = 24°$, $\theta = 10°$, $\theta = 5°$, $\theta = 2°$ EGBs and the RFS taken at T = 68 K. (b) The current-voltage $I - V$ curves for the $\theta = 24°$, $\theta = 10°$ EGBs under higher magnification of the current scale.

of the same samples used for the rf measurements were taken. The lower temperature (higher J_c) dc measurements sometimes damage the films irreversibly due to heating

effects that occur for $I > I_c$. The $I-V$ curves for the 10° EGB and 24° EGB samples are shown again in Fig. 5-2 (b) on a finer scale so that their detailed structure can be observed more clearly. The I_c obtained from the $I-V$ curves (10-μV criterion) are given in Table 5.1. The 2° EGB and the RFS have very similar $I-V$ plots showing the flux-flow behavior that is characteristic of films grown on single-crystal substrates. The 5° EGB still shows resistance due to flux-flow in the $I-V$ curve, although the I_c is reduced by a factor of three compared to that of the 2° EGB and the RFS shown in Fig. 5-2 (a). Between 5° and 10° the $I-V$ curves are transformed from a flux-flow-resistivity type of curve to a resistively shunted-junction (RSJ) type of coupling [53], accompanied by a decrease in critical current of more than an order of magnitude. The RSJ coupling is evident in Fig. 5-2 (b) by the sharp break to a constant-slope resistive state for the 10° and 24° EGBs at their respective critical current levels. The dc critical currents for the 10° and 24° EGBs have been suppressed by approximately two and three orders of magnitude, respectively, compared to the RFS I_c value.

5.1.4 Comparison of rf and dc results

From the measured data, the values of the rf and dc critical currents were determined and the results are presented in Table 5.1. A plot showing the rf and dc I_c data normalized to their respective maximum values I_{cMAX} are presented in Fig. 5-3, showing the relative dependence of I_c/I_{cMAX} on θ. By normalizing the I_c data, the dependence of I_c on θ is independent of the detailed definition of I_c and the rf and dc results can be quantitatively compared. The RFS is plotted as $\theta = 0°$ in Fig. 5-3.

A significant result seen in Fig.5-3, is that as the misorientation angle θ increases, the EGBs cause a greater decrease in the normalized I_c determined from dc measurements than that determined by the rf data. The normalized dc critical current changes by three orders of magnitude as θ goes from 0° to 24°. The greatest difference in the rf and dc results in Fig. 5-3 is for the $\theta = 10°$ data, where the relative values differ by over an order of magnitude.

The rf data presented in this chapter indicate that grain boundaries with a mis-

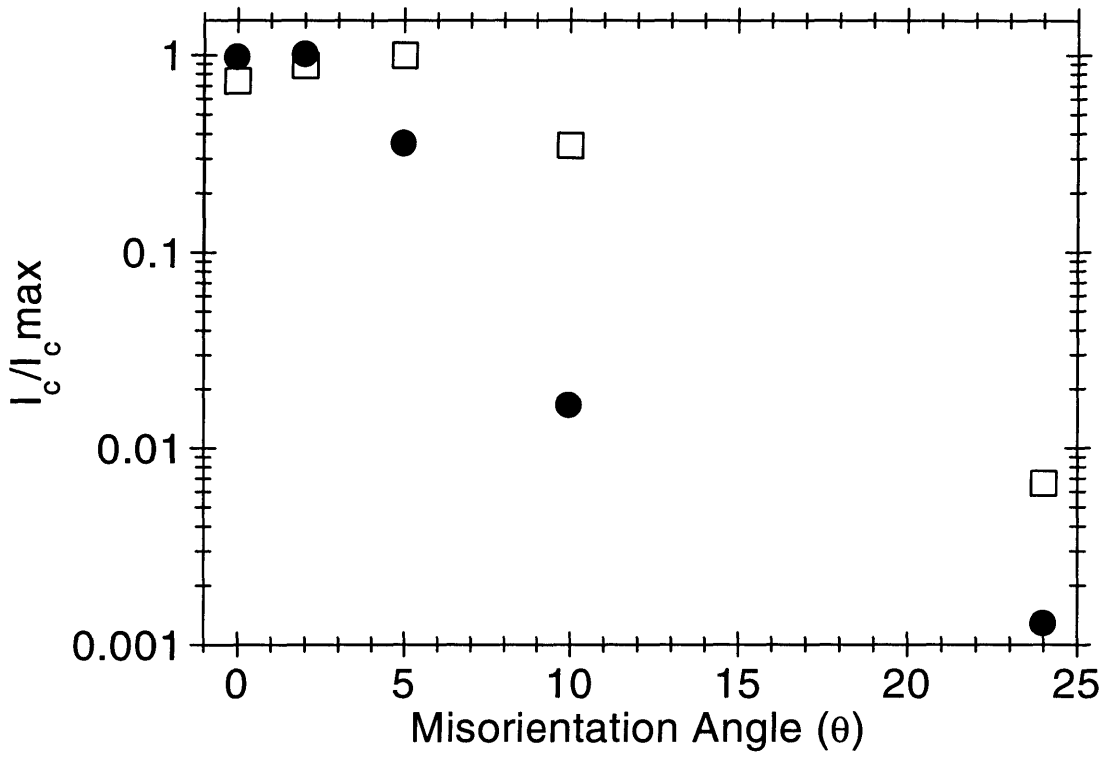

Figure 5-3: Comparison of the dependence of I_c on θ as determined by dc (●) and rf (□) measurements normalized to their respective maximum I_c values I_{cMAX} at T = 50 K. The RFS is plotted as $\theta = 0°$. The y-axis is on a log scale showing a three order of magnitude change in the dc I_c/I_{cMAX} as a function of θ.

orientation angle $\theta \leq 5°$ do not affect the rf power handling in YBCO thin films. That the 2° EGB did not affect either the rf or dc measurements compared to the RFS could suggest that 2° grain boundaries are naturally present in these films. The 5° EGB reduced the I_c determined from dc measurements but not its rf counterpart, suggesting that a different mechanism determines I_c in the dc and rf cases. The 24° and 10° EGBs, which show RSJ coupling in the $I - V$ curves, also cause nonlinearities in the rf power handling, suggesting that the grain boundary must suppress the order parameter sufficiently to form a RSJ before rf power handling is affected. The rf data show a large difference in the power handling between the 24° and 10° EGBs, warranting a future investigation of intermediate angles.

5.2 Discussion

The measurements presented in Figs. 5-1, 5-2, and 5-3 demonstrate that grain boundaries in YBCO thin films can have a deleterious effect on the rf and dc current transport properties. The extent of the degradation in the critical current is strongly dependent on the misorientation angle θ of the grain boundary. Many studies of the dc $I-V$ characteristics of YBCO grain boundaries engineered on bicrystal substrates show an exponential dependence of the dc I_c on θ [52, 71, 72, 73] and overdamped RSJ behavior for $\theta \approx 10°$ and larger. The RSJ grain boundaries also cause a nonlinear impedance due to Josephson-vortex nucleation in the weak link which results in power losses. [59, 64, 65] While the physical mechanisms determining the properties of the grain boundaries are not well established [41, 74], there are some prevailing trends in the observed experimental results and theoretical explanations.

Experimental studies on how the dc transport properties of engineered YBCO grain boundaries depend on the magnitude of θ show some common features that are independent of the bicrystal-substrate material and the deposition technique. The measured values of J_c show an overall exponential dependence on θ [52, 71, 72, 73, 75], although the reported values of J_c for a given misorientation angle can vary substantially. The results of the dc measurements from this thesis work are compared in Fig. 5-4 with results of similar measurements from other studies, showing the normalized critical-current density as a function of θ, $J_c(\theta)/J_c(\theta = 0)$. Although there is a large spread in the data shown in Fig. 5-4, there is an overall exponential dependence on θ demonstrated by the exponential function $J_c(\theta) = J_c(0)\exp(-\theta/\theta_0)$ plotted with the data using $\theta_0 = 4°$. Possible physical origins for this dependence are explained below. The early pioneering work by Dimos et al. [52] (1988), found that J_c saturates for $\theta \geq 20°$ in their study of YBCO films grown on symmetric $SrTiO_3$ bicrystal substrates with a critical current dependence of $1/\theta$ at low angles. Recently, (1998) Hilgenkamp et al.[72] found a continued exponential decrease in I_c up to $\theta = 45°$, and they found this exponential behavior to be independent of whether the $SrTiO_3$ bicrystal substrates used were symmetric or asymmetric. The results of

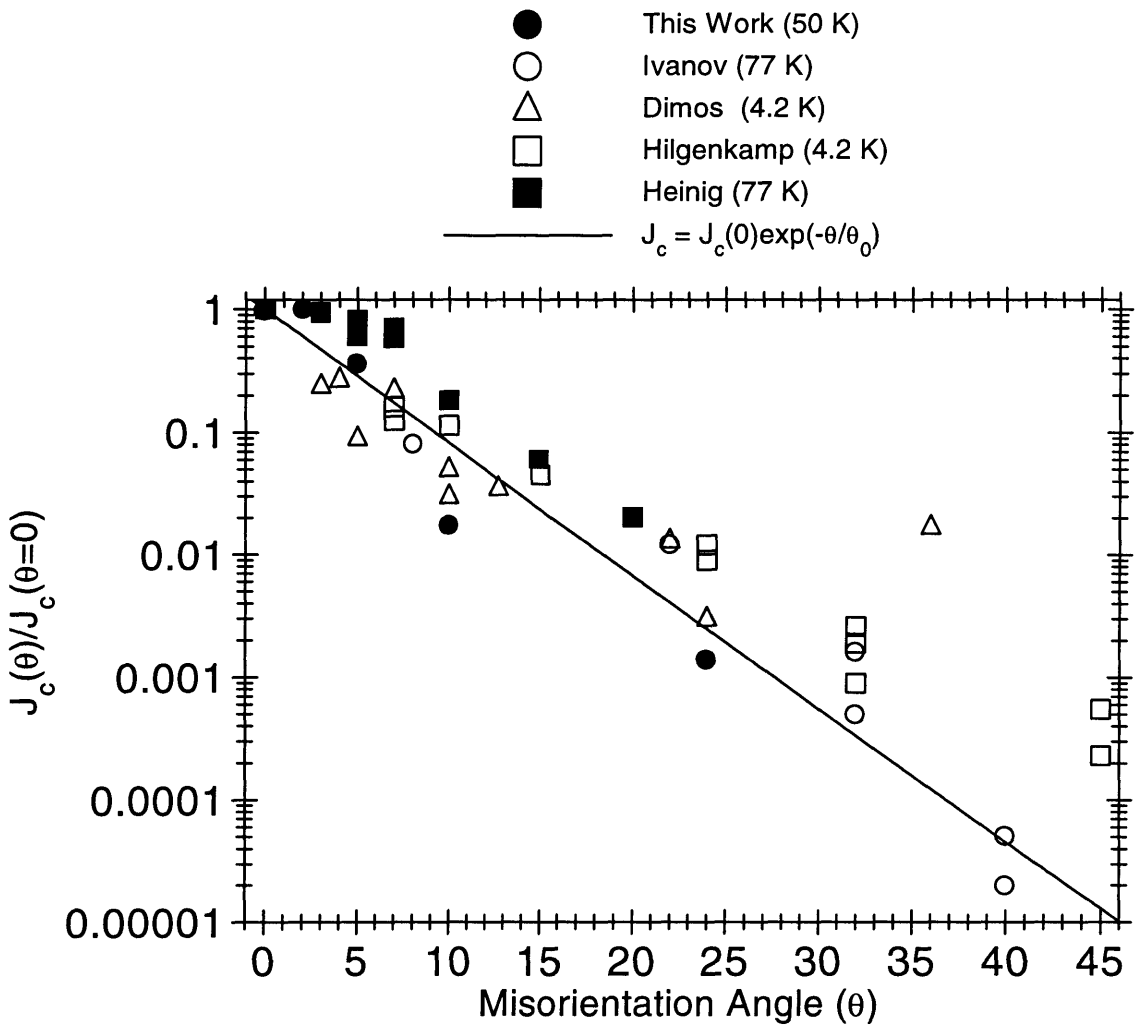

Figure 5-4: The dependence of the normalized critical current density on θ, $J_c(\theta)/J_c(\theta = 0)$ comparing the results of this thesis study with the results of similar measurements by other researchers. The results of Dimos et al. and Heinig et al. show the ratio of the film J_c to the grain boundary J_c as measured on separate test structures patterned from a film grown on a single bicrystal substrate.

Ivanov et al.[73], using asymmetric YSZ bicrystals, and Heinig et al., using symmetric $SrTiO_3$ bicrystals agree with the exponential dependence of J_c on θ. In addition, the dc measurements all show that θ has a transition value where the $I-V$ characteristics change from a flux-flow to an overdamped RSJ type of curve. The results of Heinig et al. [71] show that the crossover from a low-angle flux-flow $I-V$ curve, to a high-angle RSJ behavior in the $I-V$ occurred around $\theta = 7°$, while Hilgenkamp et al.[72]

found that this crossover occurred near $\theta = 15°$. The results of this thesis work show the transition from low- to high-angle properties occurs for θ between 5° and 10°. Another common finding of most angular dependence studies is that the value of R_n for high-angle RSJ-type grain boundaries is independent of temperature. From these experimental results, one can conclude that a J_c that depends exponentially on θ, and the existence of a crossover θ value, where the grain boundary becomes a RSJ with an R_n independent of temperature, are intrinsic properties of YBCO.

There are no other similar studies in the literature of the rf angular dependence shown in Figs. 5-1 and 5-3 with which to make a comparison. However, some general conclusions can be drawn about the effect of large-angle RSJ grain boundaries on rf power handling. Measurements of the rf current dependence of $1/Q$ by Hein et al. [76] performed on a step-edge grain-boundary JJ incorporated into a microstrip resonator show the same characteristic features observed in Fig. 4-8; these include, (1) a linear dependence of $1/Q$ on rf current below a well defined, temperature dependent, critical rf current level, $I_{rf} = I_c$, where the $1/Q$ increases sharply and abruptly with step structures evident, and (2) a saturation value of $1/Q$ at large I_{rf}, that is independent of temperature, and from which an rf JJ saturation resistance, R_j^{sat}, is calculated and found to agree with the measured dc value of R_n. While Hein et al. attributed the steps in $1/Q$ vs. I_{rf} to defects in the grain boundary, the modeling work of Chap. 4 [59] suggests that the steps they found were due to flux quantization in Josephson vortices created by rf currents. The long-junction modeling work of McDonald et al.[64] and Xie et al.[65] agree with the results of Chap. 4, showing that the step structures occurring in the JJ resistance as a function of I_{rf} occur when the gauge invariant phase difference across the JJ bifurcates by 2π as in Fig. 4-17 corresponding to an additional Josephson vortex being created per rf cycle. These rf JJ effects cause nonlinearities in the impedance and power losses. The results of this thesis work show that low-angle grain boundaries do not affect the rf power handling in YBCO films. The observed angular dependence of I_c/I_c^{MAX} suggests that mechanisms other than low-angle grain boundaries cause the onset of nonlinear behavior at values of I_{rf} below the I_c corresponding to the low-angle grain boundary.

The underlying physical mechanism that causes grain boundaries to suppress the J_c in YBCO films with a strong dependence on misorientation angle remains to be determined. Recent tunneling experiments between Pb and YBCO [77], and the observation of half-integer flux quanta in tricrystal rings of YBCO [78], seem to indicate that the symmetry of the order parameter in YBCO is a combination of s-wave and $d_{x^2-y^2}$-wave dependence. An anisotropic order parameter could explain some of the unique features of high-T_c cuprates. It has been proposed [74, 79] that a boundary region with a depressed order parameter is intrinsically created at the interface between two $d_{x^2-y^2}$ wave superconductors which form a misoriented contact rotated by θ in the basal plane. The angular dependence of the phase of the $d_{x^2-y^2}$ wave order parameter determines that for an ideal misorientation contact as shown in Fig.4-2, the value of ϕ will increase from 0 to $\pi/4$, as θ is increased from 0° to 45°, by virtue of the misorientation of the anisotropic d-waves. Such a contact depends only on the magnitude of θ and can form a JJ without any nonsuperconducting interlayer material in between the oriented superconducting electrodes. Thus, the d-wave picture is consistent with an angular dependent I_c and the observed crossover θ value where the I_V characteristics change from a low-angle, flux-flow resistivity, to a high-angle RSJ type of $I-V$ curve, that is calculated to occur at a value of $\theta \approx 10°$. Calculations of the dependence of J_c on θ done by considering the $d_{x^2-y^2}$ wave symmetry of the order parameter, and the observed microstructural faceting of some YBCO bicrystal grain boundaries, show an exponential dependence of J_c on θ [80]. However, this work can only account for a one-order-of-magnitude decrease in J_c when θ increase from 0° to 45°, while the experimental results in Fig. 5-4 show a decrease of 4-5 orders of magnitude.

The dependence of the electronic properties of YBCO grain boundaries on θ can be understood using a phenomenological approach based on the observed microstructural evolution of grain boundaries as a function of θ. For very low-angle bicrystal substrates, $\theta \leq 3°$, as the YBCO film is deposited, strain fields due to the relative misorientation will cause localized dislocation cores to form in a linear array along the boundary length.[81, 82] These dislocation cores have been imaged by STEM [83]

showing that small islands of nonsuperconducting material form on a nanometer scale. In the very low-angle limit, the dislocation cores are spaced by a distance $l_d \gg \xi$, leaving channels of undisturbed superconducting lattice between the dislocation cores. Thus, very low-angle grain boundaries will not affect J_c. As θ is increased to a range $\theta_0 \approx 4° - 5°$, the value of l_d becomes comparable to ξ resulting is a suppression of the order parameter and hence J_c.[81] As θ is further increased, there exists a critical value θ_c where the dislocation cores begin to overlap and l_d goes to zero. At values of $\theta \geq \theta_c$ the grain boundary is completely non superconducting and a RSJ is formed. As θ is further increased above θ_c the effective width of the grain boundary increases [83] resulting in a further reduction of J_c and an increase in R_n. The almost universally observed exponential dependence of J_c on θ can be related to the evolution of the grain boundary with increasing θ. Phenomenologically, it is found that

$$J_c(\theta) = J_c(0)e^{-\theta/\theta_0} \tag{5.1}$$

yields good agreement with the experimental results. Intuitively, it seems reasonable to normalize θ to the value θ_0 where a reduction in J_c begins to occur. This dependence is plotted in Fig.5-4 for $\theta_0 = 4°$.

It is established that YBCO film growth occurs through the nucleation of three dimensional islands, and takes place in non equilibrium conditions. [83, 84] Therefore, it is probable that the YBCO grain boundary will not follow the substrate boundary exactly. In fact it has been shown that the boundaries tend to facet and meander,[82, 85, 86] and this could account for the large spread in the data shown in Fig. 5-4 for a given θ value. Thus, there exists a range of values for θ_0 and θ_c which will depend on the film deposition parameters. In this context, a possible explanation for the observed difference in the rf and dc dependence on θ shown in Fig. 5-3 is that the value of θ_0 is effectively larger in the rf than in the dc case. The best fit to the rf data is for $\theta_0 = 6°$, however, the functional form of Eq. 5.1 does not fit the rf data well. While many universal trends in the dependence of J_c on θ can be identified, a complete description is still lacking.

Chapter 6

Second-Harmonic Generation

The long-junction-modeling results presented in Fig. 4-13 showed the generation of a second harmonic by the rf currents in the JJ. The calculation presented in Fig. 4-13 predicts a second harmonic amplitude that depends on the rf current level, and this signal appears and disappears as the rf current is increased. Since the ERSJ model represents a uniform JJ with an input source current that is both spatially and temporally symmetric, the presence of a current dependent second harmonic was not anticipated,. However, a closer investigation of the modeling results revealed that the source of the second-harmonic signal is time-reversal symmetry breaking in the long junction, resulting in unequal numbers of Josephson vortices being created in each half of the rf cycle at certain rf current levels. This effect can be seen in Fig. 4-17, by noting that in Fig. 4-17 (a) and (c), the plots are symmetric about $\Phi/\Phi_0 = 0$, while in Fig. 4-17 (b) and (d), the plots are asymmetric about $\Phi/\Phi_0 = 0$. It is the asymmetric states that generate the second harmonic amplitude shown in Fig. 4-13. The second harmonic generation is present at the small plateaus in the resistance vs. rf current plot in Fig. 4-13, while at the larger plateaus, the second harmonic disappears. As the rf input current to the JJ is increased, the resistance increases in a stepped structure as the state of the JJ alternates between symmetric, where equal numbers of Josephson vortices are created on each half of the rf cycle, and asymmetric, where one more Josephson vortex is created on one half of the rf cycle than the other resulting in a second harmonic. A similar dependence of second harmonic amplitude on rf field was

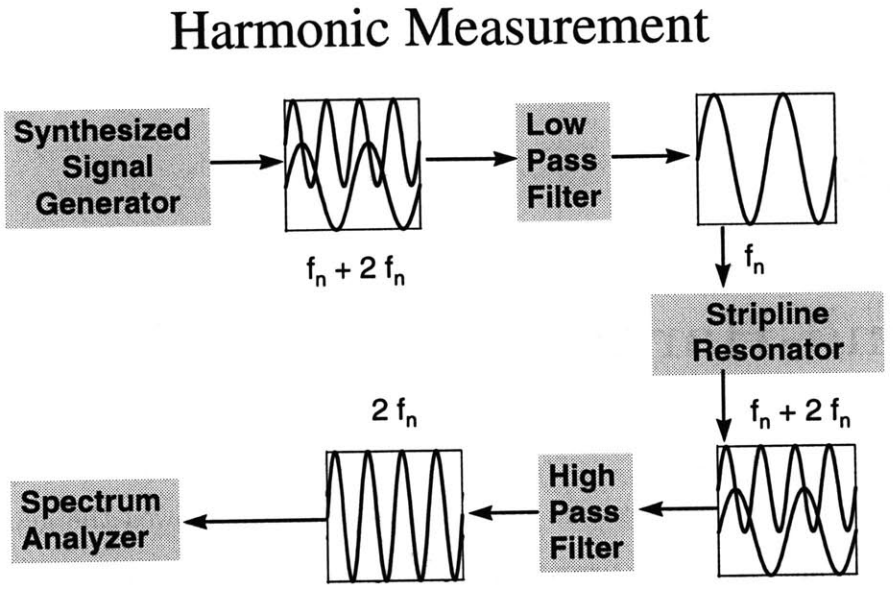

Figure 6-1: Schematic of the experimental set up used to measure second harmonic generation. A synthesized signal output at frequency f_n goes through a low-pass filter to eliminate any second harmonic at $2f_n$. Then the signal at f_n may produce an output from the stripline resonator at the second harmonic $2f_n$. This amplitude of the second harmonic is measured using a spectrum analyzer after the fundamental signal at f_n is removed using a high-pass filter to avoid any spurious second harmonic generation in the spectrum analyzer.

predicted independently in the long junction modeling work of McDonald et al.[64] Motivated by these theoretical predictions, I present below the results of a series of experiments undertaken to directly measure second harmonic generation.

To investigate the predictions of the ERSJ model experimentally, I performed a series of measurements of the second harmonic amplitude generated in stripline resonator devices as a function of rf input power. These measurements were performed using YBCO films grown on both bicrystal and single crystal substrates. In this

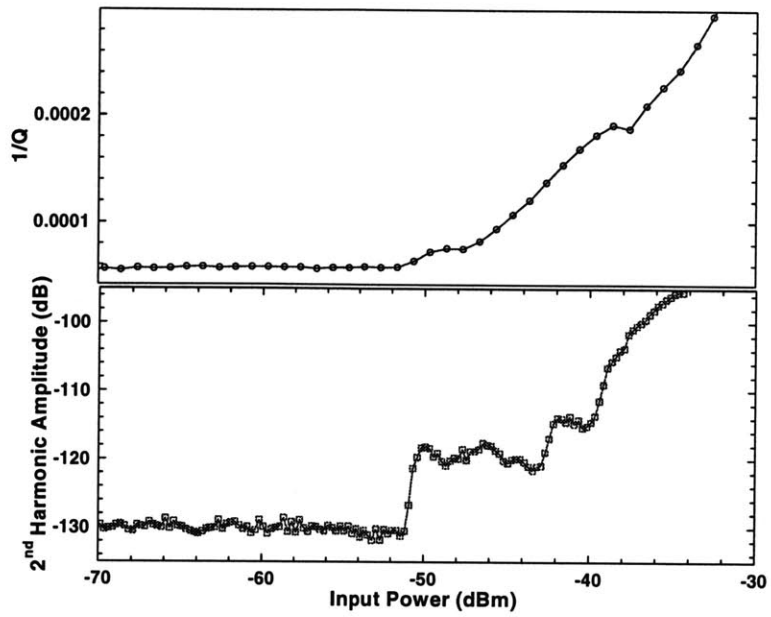

Figure 6-2: Comparison of $1/Q$ and the second harmonic amplitude as a function of rf input power measured on a 24° grain boundary JJ at T = 50 K. The increase in the second harmonic begins at the same input power level where the $1/Q$ begins to increase.

chapter, I present the results of a preliminary study of second-harmonic generation in YBCO thin films and grain boundaries.

The experimental set up used is shown schematically in Fig. 6-1. The measurement is performed by using a synthesizer to generate a CW rf signal at the resonant frequency f_n of a stripline resonator. This signal then goes through a low-pass filter to eliminate any second harmonic emanating from the synthesizer. The temperature of the device is stable to one part per thousand over the entire measurement period and magnetic shielding is used to ensure that the ambient field is less than 100 nT. The amplitude of the second harmonic is recorded using a spectrum analyzer. High pass filters are used between the resonator and the spectrum analyzer to suppress the signal at f_n sufficiently to prevent any spurious second harmonic generation in the

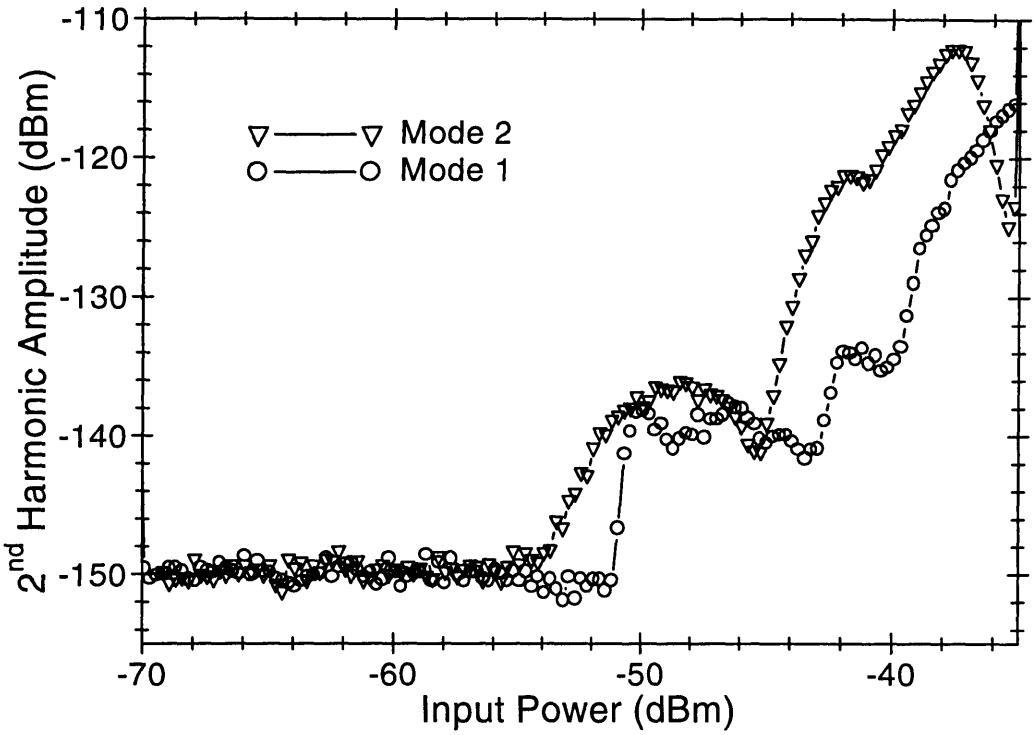

Figure 6-3: A comparison of the second harmonic amplitude as a function of rf input power for the $n = 1$ and $n = 2$ resonant modes. This measurement was performed on a 24° grain boundary JJ and taken at T = 50 K.

spectrum analyzer. A spectrum analyzer is used as a small bandwidth, low-noise receiver to record the power transmitted. An amplifier, which is not shown in Fig. 6-1, is used after the high-pass filter to increase the signal to noise ratio. The second harmonic amplitude at $2f_n$ is measured as a function of input power. This experimental set up was calibrated and tested using reference loads to ensure that the only source of a second harmonic was the stripline resonator device being tested.

The ERSJ model calculations of the junction impedance as a function of rf current were in good agreement with the measured results on a 24° grain-boundary JJ presented in Figs. 4-14 and 4-15. Hence, the first measurements of second harmonic generation were performed on a 24° grain-boundary JJ. The results of this measurement for the $n = 1$ resonant mode are presented in Fig. 6-2, showing a comparison of the second harmonic amplitude as a function of rf input power, with the $1/Q$, taken on the same power scale. Both sets of data in Fig. 6-2 were taken at T = 50 K.

The onset of the second-harmonic signal occurs at approximately the same rf power level where the $1/Q$ begins to increase, and the second harmonic shows interesting structure. Although this result (Fig.6-2) differs from the modeling shown in Fig. 4-13, this seemed like a very encouraging result. However, subsequent measurement of the second harmonic generation in the $n = 2$ mode revealed a larger amplitude in the $n = 2$ mode than in the $n = 1$ mode. The results of measurements performed on a 24° grain-boundary JJ comparing the $n = 1$ and $n = 2$ mode second-harmonic amplitudes as a function of rf input power are shown in Fig. 6-3. This result was surprising, since no JJ effects were detected in the $n = 2$ measurements of the $1/Q$ and $\Delta f_n/f_n$ data shown in Fig. 4-6. Measurement of the second-harmonic generation performed an a 10° grain-boundary JJ are shown in Fig. 6-4. As with the 24° grain-boundary JJ, the 10° grain-boundary JJ shows a similar dependence of the second harmonic amplitude on rf input power for the $n = 1$ and $n = 2$ modes. The conclusion drawn from the data in Figs. 6-3 and 6-4 is that the measured second harmonic amplitude was not due to the grain boundary JJ, but is originating in the background film.

Measurements of the second harmonic were next performed on YBCO films grown on single crystal sapphire substrates, to investigate the conclusions drawn from the measurements on engineered grain boundaries that the second harmonic is generated in the YBCO film independent of the engineered grain boundary. The results of these measurements are presented in Fig. 6-5 showing the second harmonic amplitude as a function of rf input power for the $n = 1$ mode at T = 10, 40, and 70 K. The rf input power level at which the second harmonic rises from the noise floor is more than two orders of magnitude lower than for any of the measurements performed on films grown on bicrystal substrates. There is significant structure evident in the curves with quasi-periodic cancellations of the second harmonic signal.

To investigate whether the second-harmonic generation is unique to YBCO, the measurements were also performed on niobium films grown on single-crystal sapphire substrates. The results of these measurements are presented in Fig. 6-6 showing a comparison of the second harmonic amplitude as a function of rf current in YBCO and niobium. The results are clear, although the niobium does show a second harmonic,

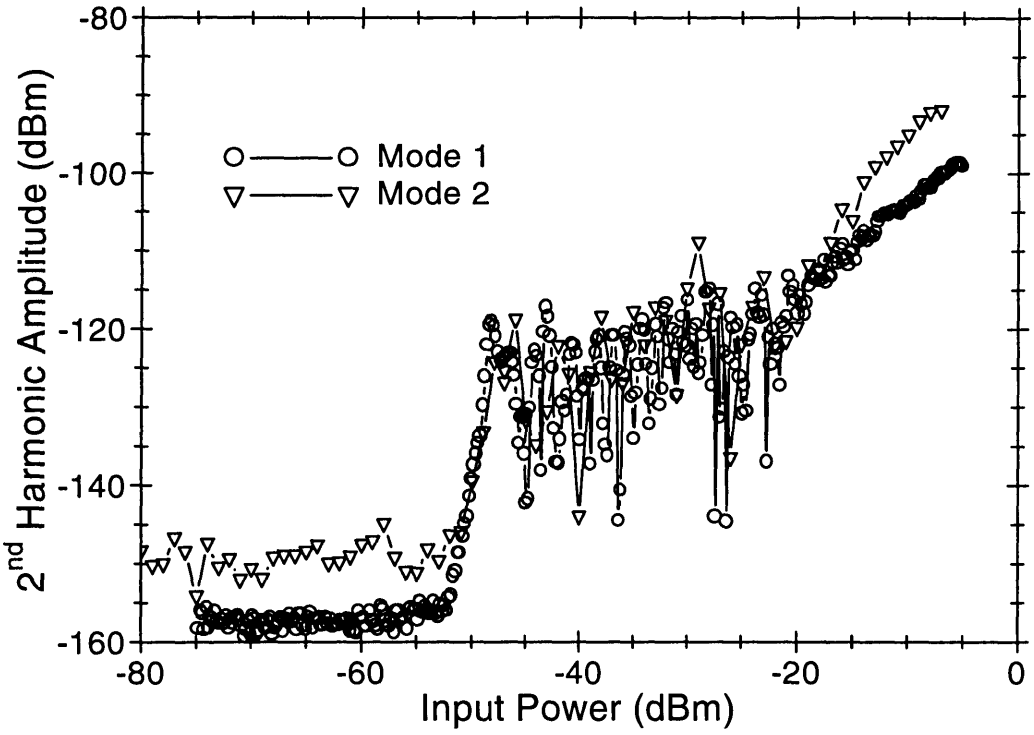

Figure 6-4: A comparison of the second harmonic amplitude as a function of rf input power for the $n = 1$ and $n = 2$ resonant modes. This measurement was performed on a 10° grain boundary JJ and taken at T = 70 K.

in YBCO it is initially generated at more than three orders of magnitude less rf current than in niobium. The magnitude of the second harmonic amplitude in YBCO remains orders of magnitude greater than in niobium over the entire measurement range. These results suggest that YBCO films may generate the second harmonic signal through intrinsic mechanisms.

The origins of the second harmonic generation in YBCO films are unclear at this time. A second harmonic will be generated by the rf current if a dc field is simultaneously applied, and this effect had been measured in high-T_c thin films,[87, 88, 89] although references are scarce. The dc field acts to break the symmetry of the system, generating a second harmonic signal. A possible explanation of the zero-field second harmonic presented in this work is that time-reversal symmetry is intrinsically broken in d-wave superconductors due to scattering at surfaces, as has been proposed. [90] Another possibility is that the second harmonic is generated by magnetic scatter-

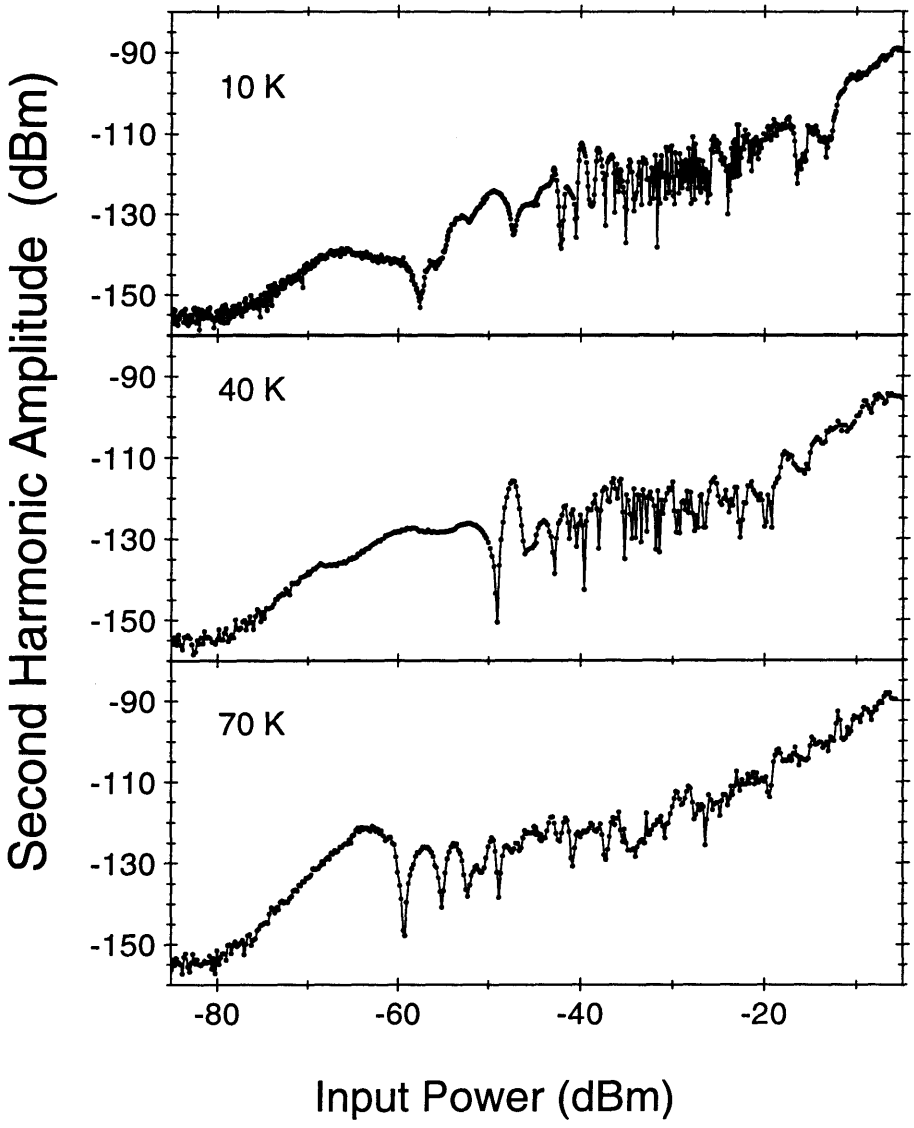

Figure 6-5: The second harmonic amplitude as a function of rf input power as measured on a YBCO film grown on a single crystal sapphire substrate. The results are shown at three different temperatures.

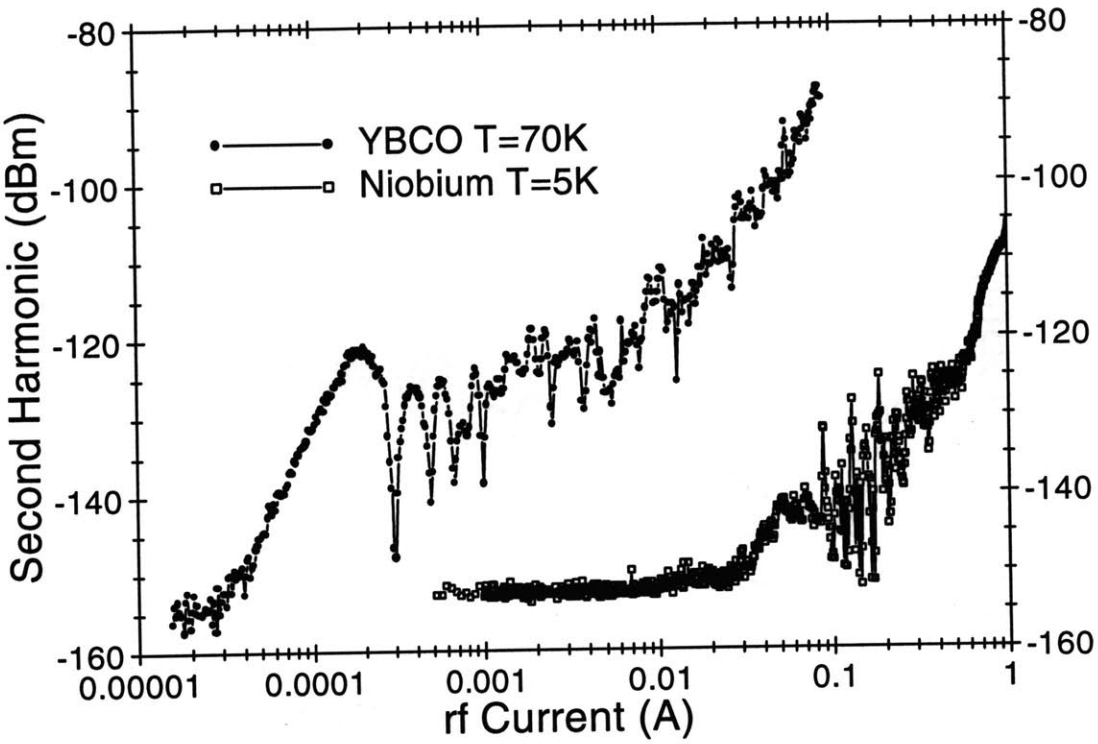

Figure 6-6: A comparison of second harmonic generation in YBCO and niobium. This plot shows the second harmonic amplitude as a function of rf current. These measurements were performed on YBCO and niobium stripline resonators patterned from films grown on single-crystal sapphire substrates.

ing due to oxygen overdoping, although this is speculative. [91] While the physical origin of the second harmonic remains to be determined, the measurement results presented here were reproducible. The reproducibility was confirmed by performing the measurements at both the Lincoln laboratory and the Air Force Research laboratory and also performing the measurements on different YBCO films. The results were independent of both the laboratory where the measurement was done and the sample used, effectively eliminating the possibility of experimental error. Since the magnitude of the second harmonic presented in Fig. 6-5 is relatively large, this type of measurement could turn out to be a very sensitive probe of the fundamental properties of high-T_c superconducting systems.

Chapter 7

Conclusions

The motivation for the work presented in this thesis is the desire to understand the physical mechanisms responsible for the observed rf power-handling properties of YBCO thin films. The high critical temperature and ease of manufacture make YBCO a very attractive material for use in technological applications of superconductors. However, the surface impedance, $Z_s = R_s + iX_s$, is dependent on rf power. The power dependence of Z_s limits the potential uses of YBCO films for microwave-frequency device applications, due to power losses and nonlinearities that occur at rf power levels necessary for practical exploitation of the material. Due to the numerous imperfections observed in even the highest quality films, it is probable that the limited rf power handling capabilities of YBCO, as demonstrated in Chap. 3, result from the presence of microscopic defect structures, and not from intrinsic material limitations. Based on the almost universally observed granularity of YBCO films, it has been proposed that Josephson-junction effects occurring at grain-boundary weak links are responsible for the nonlinearities and the resulting power losses. Thus motivated, in this work a study of the rf power dependence in YBCO thin films, grain boundaries, and Josephson junctions was presented.

The results of measurements and modeling of the rf impedance in Josephson junctions presented in Chap. 4 demonstrated that the nucleation of Josephson vortices by rf currents does indeed cause substantial power loss and nonlinearity. The JJs used showed classic RSJ behavior in dc measurements performed prior to the rf character-

ization. The rf measurements resulted in a direct observation of how the nucleation of individual flux quanta affects the impedance. A comparison of the long-junction modeling results, with the rf measurements on a 24° grain-boundary JJ, provided a quantitative understanding of how the JJ impedance depends on rf current. The rf value of J_c occurs when the rf current level is sufficient to nucleate one Josephson vortex per rf cycle. The nucleation is initiated at the JJ edges, where J_{rf} is a maximum in the stripline. As the rf current is increased, their are stepped increases in the resistance due to the quantization of magnetic flux in the JJ. Each sequential increase in the number of Josephson vortices created per rf cycle is associated with a stepped increase in resistance, and a related reactance increase. Due to the finite length of the junction, a saturation level is reached when the number of Josephson vortices is large enough so that a vortex nucleated on one edge of the JJ is pushed to the center of the JJ, where it meets an antivortex that originated on the other side of the JJ, and the two annihilate each other. Above this current level, the JJ is in the normal resistive state, and the impedance can no longer increase due to JJ effects. The saturation level of the rf JJ resistance is identical to the R_n obtained from dc measurements.

The study of the rf dynamics of JJs presented in this thesis leads to the conclusion that the presence of a JJ in a superconducting thin film can severely degrade its power handling capabilities. The important parameters of the JJ are the I_c and R_n, and the values of these parameters depends strongly on the specific microstructural composition of the JJ. The degree to which a particular defect structure behaves as a weaklink is a consequence of the amount of suppression of the superconducting order parameter. For the case of a grain-boundary weak link in a c-axis oriented YBCO film, the magnitude of the basal plane misorientation angle θ is known to have a large effect on the dc electrodynamic properties. Thus, a comparative study of how the magnitude of θ affects both the dc and rf properties was undertaken. The results of the angular dependence study in Chap. 5 showed that the measured effect that engineered grain boundaries have on the rf properties is not directly correlated with the results of dc measurements. In fact, the relative effect that the grain boundaries

have on the I_c value shows a greater dependence on θ in the dc case than in the rf case. For example, a $\theta = 5°$ grain boundary had no effect on the I_c determined from rf measurements, while it reduced the dc I_c substantially. It appears that unless the grain boundary suppresses the order parameter sufficiently to form a RSJ, the rf properties are not affected by the presence of the grain boundary. Since the impact of low-angle grain boundaries on the rf power handling is inconsequential, their presence should not be a concern to film growers.

The prediction of the modeling that a second harmonic is generated by rf currents in long JJs, was also investigated experimentally, and it was found that the second harmonic is in fact generated in the YBCO film, without a JJ necessarily being present. The modeling results showed that the second harmonic is generated by time reversal symmetry breaking in the JJ. Possibly, the results in Chap. 6 indicate that time-reversal symmetry is broken by intrinsic mechanisms in YBCO films. If so, the measurements of second-harmonic generation could turn out to be a very sensitive probe of the superconducting state of the YBCO system. While the results presented in this thesis are preliminary, they certainly suggest that further study is warranted.

There are some other aspects of this thesis work that could be expanded on in the future. It would be useful to investigate the rf properties of grain boundaries with other values of θ than those investigated here, particularly in the range $11° \leq \theta \leq 23°$, and $\theta \geq 25°$. An investigation of the effect that an externally applied dc magnetic field has on the rf properties of engineered grain boundaries could prove useful in interpreting the dc field dependence of Z_s in thin films, by providing information on the role grain boundaries have on flux pinning.

Bibliography

[1] K. Mendelssohn. *The Quest for Absolute Zero.* Halsted Press N.Y., New York, 1977.

[2] M. Cyrot and D. Pavuna. *Introduction to Superconductivity and High-Tc Materials.* World Scientific, New Jersey, 1992.

[3] J. G. Bednorz and K. A. Mueller. *Z. fur Phys.*, 64:189–195, 1986.

[4] P. Chu. In *Quantum Theory of Real Materials*, pages 411–424. The Unusual High Temperature Superconductors, Kluwer Academic, Norwell MA, 1996.

[5] R. Beyers and T. M. Shaw. In *Solid State Physics*, volume 42, page 135. The Structure of $YBa_2Cu_30_{7-\delta}$ and its Derivatives, 1989.

[6] A. M. Portis. *Electrodynamics of High-Tempersture Superconductors.* World Scientific, New Jersey, 1993.

[7] T. Seigrist, S. Sunshine, D. W. Murphy, R. J. Cava, and S. M. Zahurak. *Phys. Rev. B*, 35:7137, 1987.

[8] C. McCarroll, B. Zhou, S. Han, and L. Luo. *IEEE Trans Appl. Supercond*, 3, 1993.

[9] T. Konaka, M. Sato, H. Asano, and S. Kubo. *J. Supercond.*, 4:283–288, 1991.

[10] L. R. Vale, R. H. Ono, and D. A. Rudman. *IEEE Trans. Appl. Supercond*, 7:3193–3196, 1996.

[11] A. Westerheim, A. Anderson, D. Oates, S. Basu, D. Bhatt, and M. Cima. *J. Appl. Phys.*, 75:393–403, 1994.

[12] O. Martinez, J. Jimenez, P. Martin, D. Chambonnet, C. Nelouet, S. Nicoletti, and L. Correra. *Physica C*, 270:144–153, 1996.

[13] G. Kastner, D. Hesse, R. Scholz, H. Koch, F. Ludwig, M. Lorenz, and H. Kittel. *Physica C*, 243:281–293, 1995.

[14] A. F. Marshall and R. Ramesh. In *Interfaces in High-T_c Superconducting Systems*, pages 71–115. Microstructure of Interfaces in $YBa_2Cu_3O_{7-x}$ Thin Films, Springer-Verlag, 1993.

[15] A. V. Velichko, N. T. Cherpak, E. V. Izhyk, A. Kirichenko, and A. V. Moroz. *Supercond. Sci. Technol.*, 11:716–729, 1998.

[16] J. Hudner, O. Thomas, D. Boursier, E. Mossang, J. Senateur, J. Villegier, H. Moriceau, M. Schwerdtfeger, J. Jager, and H. Ohlsen. *Supercond. Sci. Technol*, 7:195–205, 1994.

[17] T. Van Duzer and C. W. Turner. *Principles of Superconductive Devices and Circuits.* Elsevier, New York, 1981.

[18] D. M. Pozar. *Microwave Engineering.* Addison-Wesley, Reading MA, 1990.

[19] M. Tinkham. *Introduction to Superconductivity.* McGraw-Hill, New York, 1996.

[20] N. W. Ashcroft and N. D. Mermin. *Solid State Physics.* W. B. Saunders, Philadelphia PA, 1976.

[21] T. P. Orlando and K. A. Delin. *Foundations of Applied Superconductivity.* Addison-Wesley, Reading MA, 1990.

[22] S. M. Anlage and D. Wu. *J. Supercon.*, 5:395–402, 1992.

[23] P. P. Nguyen, D. E. Oates, G. Dresselhaus, and M. S. Dresselhaus. *Phys. Rev. B*, 48:6400–6412, 1993.

[24] D. E. Oates, A.C. Anderson, and P.M. Mankiewich. *J. Supercon.*, 3:251–259, 1990.

[25] D. E. Oates, A. C. Anderson, D. M. Sheen, and S. M. Ali. *IEEE Trans. Microwave Theory and Tech.*, 9:1522–1529, 1991.

[26] J. H. Oates, R. T. Shin, D. E. Oates, M. J. Tsuk, and P. P. Nguyen. *IEEE Trans. Appl. Supercon.*, 3:17–23, 1993.

[27] P. P. Nguyen. *Magnetic, DC Transport, and Microwave Properties of High Temperature Superconductors.* PhD thesis, Dept. of Physics, MIT, Cambridge MA, 1994.

[28] D. M. Sheen, S. M. Ali, D. E. Oates, R. S. Whithers, and J. A. Kong. *IEEE Trans. Appl. Supercon.*, 1:108–114, 1991.

[29] G. L. Matthaei, L. Young, and E. M. T. Jones. *Microwave Filters, Impedance-Matching Networks, and Coupling Structures.* McGraw-Hill, New York, New York, 1964.

[30] B. Avenhaus, A. Porch, M.J. Lancaster, S. Hensen, M. Lenkens, S. Orbach-Werbig, G. Muller, U. Dahne, N. Tellmann, N. Klein, C. Dubourdieu, J. Senateur, O. Thomas, H. Karl, B. Strizker, J. Edwards, and R. Humphreys. *IEEE Trans Appl. Supercond*, 5:1737–1740, 1995.

[31] M. Hein. In *Studies of High-Temperature Superconductors Vol. 18*, volume 42, pages 141–203. Microwave Properties of High-Temperature Superconductors: Surface Impedance, Circuits and Systems, Nova Science, Commack, NY, 1996.

[32] B. A. Willemsen, J. S. Derov, J. H. Silva, and S. Shridhar. *IEEE Trans. Appl. Supercond.*, 5:1753–1755, 1995.

[33] G. P. Srivastava, M. V. Jacob, M. Jayakumar, and P. K. Bhatnagar. *J. Appl. Phsy.*, 81:6272–6276, 1997.

[34] G. Muller, B. Ascherman, H. Chaloupka, W. Deite, M. Getta, M. Hein, S. Hensen, F. Hill, M. Lenkens, S. Orbach-Werbig, T. Patzelt, H. Peil, J. Rembesa, H. Schlick, T. Unshelm, and R. Wagner. *IEEE Trans. Appl. Supercond.*, 5:1729–1732, 1995.

[35] T. L. Hylton, A. Kapitulnik, M. R. Beasley, J. P. Carini, L. Drabeck, and G. Gruner. *Appl. Phys. Lett.*, 53:1343–1345, 1988.

[36] C. Attanasio, L. Mariitato, and R. Vaglio. *Phys. Rev. B*, 43:6128–6131, 1991.

[37] P. P. Nguyen, D. E. Oates, G. Dresselhaus, M. S. Dresselhaus, and A. C. Anderson. *Phys. Rev. B*, 51:6686–6695, 1995.

[38] D. E. Oates, P. P. Nguyen, G. Dresselhaus, M. S. Dresselhaus, C. W. Lam, and S. M. Ali. *J. Supercond*, 5:361–369, 1992.

[39] D. E. Oates, P. P. Nguyen, G. Dresselhaus, M. S. Dresselhaus, G. Koren, and E. Polturak. *J. Supercond.*, 8:725–733, 1995.

[40] J. Halbritter. *Phys. Rev. B*, 48:9735–9746, 1993.

[41] J. Halbritter. *J. Supercond.*, 8:691–703, 1995.

[42] J. Halbritter. *J. Supercond.*, 10:91–96, 1997.

[43] M. Hein, W. Diete, M. Getta, S. Hensen, T. Kaiser, G. Muller, H. Piel, and H. Schlick. *IEEE Trans. Appl. Supercond.*, 7:1264–1267, 1997.

[44] M. Hein, C. Bauer, W. Deite, S. Hensen, T. Kaiser, G. Muler, and H. Piel. *J. Supercond.*, 10:109–120, 1997.

[45] G. Hampel, P. Kolodner, P. L. Gammel, P. A. Polakos, E. Obaldia, A. Anderson, R. Slattery, D. Zhang, G. Liang, and C. Shih. *Appl. Phys. Lett.*, 69:571–573, 1996.

[46] D. Bhatt, S. N. Basu, A. C. Anderson, and A. C. Westerheim. *Physica C*, 222:283–296, 1994.

[47] D. K. Fork, S. M. Garrison, M. Hawley, and T. H. Geballe. *J. Mater Res.*, 7:1641–1651, 1992.

[48] T. L. Hylton and M. R. Beasley. *Phys. Rev. B*, 339:9042–9048, 1989.

[49] A. Barone and G. Paterno. *Physics and Applications of the Josephson Effect.* Wiley, New York, 1982.

[50] K. K. Likharev. *Dynamics of Josephson Junctions and Circuits.* Gordon and Breach, New York, 1986.

[51] G. Koren, E. Polturak, D. Cohen, E. Aharoni, and L. Patlagan. *Physica C*, 157-160, 1994.

[52] D. Dimos, P. Chaudhari, J. Manhart, and F. LeGoues. *Phys. Rev. Lett*, 61:219–222, 1988.

[53] R. Gross. In *Interfaces in High-T_c Superconducting Systems*, pages 176–209. Grain Boundary Josephson Junctions in High Temperature Superconductors, Springer-Verlag, 1993.

[54] A. Marx, U. Fath, L. Alff, and R. Gross. *Appl. Phys. Lett.*, 67:1929–1931, 1995.

[55] Y. M. Zhang, D. Winkler, P. A. Nilsson, and T. Cleason. *Phys. Rev. B*, 51:8684, 1995.

[56] T. Ogawa and T. Yamashita. *IEEE Trans. Appl. Supercond*, 5:2204–2207, 1995.

[57] D. E. Oates, P. P. Nguyen, Y. M Habib, G. Dresselhaus, M. S. Dresselhaus, G. Koren, and E. Polturak. *Appl. Phys. Lett*, 68:705–707, 1996.

[58] Y. M Habib, D. E. Oates, G. Dresselhaus, and M. S. Dresselhaus. *IEEE Trans. Appl. Supercond.*, 7:2553–2557, 1997.

[59] Y. M Habib, C. J. Lehner, D. E. Oates, L.R. Vale, R. H. Ono, G. Dresselhaus, and M. S. Dresselhaus. *Phys. Rev. B*, 57:13833–13844, 1998.

[60] C. J. Lehner. Modeling and measurement of microwave effects in high-t_c long josephson junctions. Master's thesis, Dept. of Physics, MIT, Cambridge MA, 1998.

[61] C. J. Lehner, D. E. Oates, Y. M Habib, G. Dresselhaus, and M. S. Dresselhaus. *J. Supercond*, In Press, 1998.

[62] Y. M. Zhang, D. Winkler, and T. Claeson. *Physica C*, 235-240:3251–3252, 1994.

[63] E. S. Fang and T. Van Duzer. In *Extended Abstracts of the 1989 International Superconductivity Electronics Conference*, page 407. Japan Soc. Appl. Phys., 1989.

[64] J. McDonald and J. R. Clem. *Phys. Rev. B*, 56:14723, 1997.

[65] L. M. Xie, J. Wosik, and C. Wolfe. *Phys. Rev. B*, 54:15494, 1996.

[66] J. McDonald, J. R. Clem, and D. E. Oates. *Phys. Rev. B*, 55:11823, 1997.

[67] D. E. Oates, Y. M. Habib, C. J. Lehner, J. Herd, R. Ono, and L. Vale.

[68] J. S. Herd, D. E. Oates, and J. Halbritter. *IEEE Trans. Appl. Supercond.*, 7:1299–1302, 1997.

[69] J. S. Herd, D. E. Oates, H. Xin, and S. J. Berkowitz. *IEEE Trans. Appl. Supercond.*, In Print, 1999.

[70] Y. M Habib, D. E. Oates, L.R. Vale, R. H. Ono, G. Dresselhaus, and M. S. Dresselhaus. *Appl. Phys. Lett.*, 73:2200–2203, 1998.

[71] N. F. Heinig, R. D. Redwing, I. F. Tsu, A. Gurevich, J. E. Nordman, S. E. Babcock, and D. C. Larbalestier. *Appl. Phys. Lett.*, 69:577–579, 1996.

[72] H. Hilgenkamp and J. Manhart. *Appl. Phys. Lett.*, 73:265–267, 1998.

[73] Z. G. Ivanov, P. A. Nilsson, D. Winkler, J. A. Alarco, T. Claeson, E. A. Stepantsov, and A. Y. Tzalenchuk. *Appl. Phys. Lett.*, 59:3030–3032, 1991.

[74] H. Hilgenkamp and J. Manhart. *Appl. Phys. A*, 64:553–554, 1997.

[75] D. Dimos, P. Chaudhari, and J. Manhart. *Phys. Rev. B*, 41:4038–4049, 1990.

[76] M. A. Hein, S. Bueven, M. Gottschlich, M. Perpeet, and M. Siegel. *Journ. Supercond.*, 9:233–236, 1995.

[77] K. A. Kouznetsov, A. G. Sun, A. S. Katz, S. R. Bachall, J. Clarke, R. C. Dynes, D. Gajewski, S. Han, M. B. Maple, J. T. Kim, and D. M. Ginsberg. *Phys. Rev. Lett.*, 79:3050–3053, 1997.

[78] J. R. Kirtley, C. C. Tsuei, J. Z. Sun, C. C. Chi, L. S. Yu-Jahnes, A. Gupta, M. Rupp, and M. B. Hetchen. *Nature*, 373:225–228, 1995.

[79] J. Manhart and H. Hilgenkamp. *Supercond. Sci. Technol.*, 10:880–883, 1997.

[80] H. Hilgenkamp, J. Manhart, and B. Mayer. *Phys. Rev. B*, 53:14586–14593, 1996.

[81] A. Gurevich and E. A. Pashitskii. *Phys. Rev. B*, 57:13878–13893, 1998.

[82] I. F. Tsu, S. E. Babcock, and D. L. Kaiser. *J. Mate. Res.*, 11:1383–1397, 1996.

[83] N. D. Browning, J. P. Buban, P. D. Nellist, D. P. Norton, M. F. Chisolm, and S. J. Pennycock. *Physica C*, 294:183–193, 1998.

[84] E. B. McDaniel, S. C. Gausepohl, C. T. Li, M. Lee, J. W. Hsu, R. A. Rao, and C. B. Eom. *Appl. Phys. Lett.*, 70:1882–1884, 1997.

[85] H. Hilgenkamp, J. Manhart, B. Mayer, Ch. Gerber, J. R. Kirtley, and K. A. Moler. *IEEE Trans. Appl. Supercond.*, 7:3670–3673, 1997.

[86] J. A. Alarco, E. Olsson, Z. G. Ivanov, D. Winkler, E. A. Stepantsov, O. I. Lebedev, A. L. Vasiliev, and A. Tzalenchuk anf N. A. Kiselev. *Physica C*, 247:163–179, 1995.

[87] M. R. Trunin and G. I. Leviev. *J. Phys. III*, 2:355–341, 1992.

[88] N. Khare, A. K. Gupta, S. K Shrivastava, H. K. Singh, and O. N. Srivasta. *Physica C*, 306:218–222, 1998.

[89] S. C. Lin, W. F. Hart, C. M. Chorey, and K. B. Bhasin. *Cryogenic Engineering*, 42:1017–1022, 1996.

[90] R. B. Laughlin. *Physica C*, 234:280–284, 1994.

[91] V. Z. Kresin, A. Bill, S. A. Wolf, and Y. N. Ovchinnikov. *Jour. Supercond.*, 10:267–272, 1997.